論文 / 著書情報
Article / Book Information

題目(和文)	
Title(English)	Material Property Estimation and Liquid Detection for Multi-layered Media based on Ultrasonic Nondestructive Testing
著者(和文)	沈洋
Author(English)	Yang Shen
出典(和文)	学位:博士(学術), 学位授与機関:東京工業大学, 報告番号:甲第10257号, 授与年月日:2016年3月26日, 学位の種別:課程博士, 審査員:廣瀬 壮一,三上 貴正,鍵 直樹,アニール ワイジェ,佐々木 栄一
Citation(English)	Degree:Doctor (Academic), Conferring organization: Tokyo Institute of Technology, Report number:甲第10257号, Conferred date:2016/3/26, Degree Type:Course doctor, Examiner:,,,,
学位種別(和文)	博士論文
Type(English)	Doctoral Thesis

東京工業大学
Tokyo Institute of Technology

Material Property Estimation and Liquid Detection for Multi-layered Media based on Ultrasonic Nondestructive Testing

By

Yang SHEN

A dissertation submitted in partial fulfillment of the requirement for the degree of

Doctor of Engineering

In

Department of Mechanical and Environmental Informatics

Graduate School of Information Science and Engineering

Tokyo Institute of Technology

February 2016

Adviser Professor

Prof. Sohichi Hirose

Committee Members

Assoc. Prof. Takamasa Mikami
Assoc. Prof. Naoki Kagi
Assoc. Prof. Eiichi Sasaki
Assoc. Prof. Anil C. Wijeyewickrema

ABSTRACT

During the service life of reinforced concrete (RC) slabs, damages and deteriorations can be caused due to overloading, aging, and corrosion. One of the reinforcement approaches is to add a steel plate on the bottom of a RC slab to enhance its flexural capacity. To make steel and concrete function more collaborative, epoxy is sometimes injected as adhesive into the interface between steel plate and concrete, together with anchor bolts. However, using epoxy as the adhesive will bring deterioration due to its aging and delamination on the interfaces. To prevent the failure of adhesives, we need to estimate the material property of epoxy, so that the extent of the aging of the adhesive material in service can be assessed through the historical data comparison. Ultrasonic Nondestructive Evaluation (NDE) is an advantaged approach to detect the delamination or the bonding quality of the layered medium. The elastic property of the adhesive material can also be estimated properly by obtaining the phase velocity of surface wave propagating in the layered medium through NDE test.

This research proposes an effective approach to estimate the elastic property of epoxy layer in a steel-epoxy-concrete bonding layered medium based on the wave dispersion theory. The dispersion properties of different multi-layered media, including free steel plate, steel-epoxy-concrete, steel-water-concrete, steel-spring-concrete, and steel-water-epoxy-concrete are analyzed in this study. Firstly, the boundary conditions are presented, and the dispersion equations are deduced and solved to plot the analytical dispersion curves, also the wave structure of different wave modes are obtained. Through a discussion about the influence factors to the modes and shapes of those dispersion curves, a clear understanding of wave dispersion in the steel-epoxy-concrete bonding layered medium is reached. Then, an ultrasonic

NDE test on a casted steel-epoxy-concrete specimen is conducted following the idea of Spectral Analysis of Surface Waves (SASW), by which the experimental dispersion curves can also be plotted. Through the inversion process of the analytical and experimental dispersion curves, the elastic property of epoxy layer can be successfully estimated. Then based on the estimated elastic constants, wave propagation in the steel-epoxy-concrete layered medium is simulated using Explicit Finite Element Method (EFEM), from which the numerical dispersion curves are obtained.

It has been decades since the steel plate strengthening method for RC slabs was applied on infrastructures, hence quite a lot of the strengthened slabs have already met the problems of material's aging, layers' delamination, or even worse: water's invasion. If water penetrates into the top surface of a steel plate through an additionally damaged concrete slab, serious corrosion will be caused. Therefore, it is of great importance to detect the existence of water layer in the steel-concrete or steel-epoxy-concrete layered media and acquire information on thickness and distribution area of the invaded water layer.

In this study, an ultrasonic multi-reflection approach through oblique incidence is developed for thin liquid layer detection. Firstly, the reflection factor equations are deduced, and the reflection and transmission coefficients of multi-layered media including a liquid layer are calculated theoretically. Four interfaces that would appear in the experimental study are emphasized: steel-water, water-steel, water-concrete and water-epoxy. Then, experiments on multi-layered configurations are conducted with different water layer thicknesses and bottom layer materials. By analyzing the experimental results, the existence of water layer can be clearly distinguished. The effects of incident angles, water layer thicknesses, and the material properties of bottom layer have been tested and presented with numbers of waveforms from the experiments on different multi-layered configurations. The explanation of those

experimental phenomenon is given according to the reflection and transmission coefficients. Through comparison with the theoretical wave travelling time in the water layer, the thickness of the water layer can be estimated from the time interval of reflected wave groups. This method of water layer thickness estimation is tested with acceptable errors, whose possible causes are given.

Moreover, an approach of identification of the region of the liquid layer beneath the solid layer is developed. The procedures of the identification approach are presented, and the relative NDE tests are conducted on the casted multi-layered specimen to confirm every step of the identification to be feasible. Two transducer approaching orientations for detecting the boundary of the liquid layer are tested: parallel approaching, in which the line of transmitter and receiver is parallel to the boundary; vertical approaching, in which the same line is vertical to the boundary. This identification approach of water layer's region can be effectively applied in the practical detection as well.

In summary, this research investigates the nondestructive evaluation of multi-layered media, in which two main objectives are included: to estimate the material property of epoxy layer in steel-epoxy-concrete layered media, and to detect water layer beneath the solid plate. Both the objectives have been achieved successfully through the theoretical research and the experimental work.

ACKNOWLEDGEMENT

This dissertation would not have been possible without the help, support, and guidance of several organizations and individuals who in one way or another contributed and extended their valuable assistance in the preparation and completion of this study. I would like to express my deepest gratitude and appreciation to all of them.

First and foremost, I would like to express my sincere gratefulness to my adviser, Prof. Sohichi Hirose, for so much time he spent on my research. In the past four years, he instructed me in basic knowledge of waves, discussed with me about research details, and guided me on thesis writing time and time again. His patience allowed me to think hard; his smile made me keep confident; his word drove me do firm. I am so honored to be one of his students.

I also would like to express truthful gratitude to the dissertation committee members: Assoc. Prof. Takamasa Mikami, Assoc. Prof. Naoki Kagi, Assoc. Prof. Eiichi Sasaki, and Assoc. Prof. Anil C. Wijeyewickrema for their time on reviewing my dissertation and giving valuable comments and advices.

I wish to thank the academic assistants of Hirose Lab.: Dr. Furukawa supported me a lot in preparing the final defense, and Dr. Bui inspired me much with academic spirits. Thanks will also be given to Dr. Wang, Mr. Yamaguchi, and Mr. Kang for their constructive advices on my research and helpful assistance in the experiments. I wish to express regards to Ms. Sugawara, the secretary of the laboratory, Mr. Padungsriborworn, Mr. Maruyama, and Mr. Obara for their help and encouragement in research and daily life.

I would like to extend my special thanks to Japan Society for the Promotion of Science (JSPS) for giving me the opportunity to study at Tokyo Institute of Technology and providing me scholarship through the Japanese Ministry of Education, Culture, Sports, Science and Technology (Monbukagakusho).

I would like to express my deepest gratitude to my parents for their unconditional love and encouraging support from homeland. My family always can give me strength at each hard moment, and hereby I dedicate this work to them.

List of Symbols

Symbol	Description
λ	Lame's first parameter.
μ	Shear modulus.
ρ	Density.
c, c_p	Phase velocity.
c_g	Group velocity.
c_T	Transverse wave phase velocity.
c_L	Longitudinal wave phase velocity.
c_R	Rayleigh wave phase velocity.
c_w	Longitudinal wave velocity in water.
δ_{ij}	Krocker delta.
u_i	Displacement components ($i = 1, 2, 3$).
ε_{ij}	Strain tensor.
σ_{ij}	Stress tensor.
f_i	Body force.
$\ddot{u}_i$	Velocity components ($i = 1, 2, 3$).
$\varphi,\ \psi$	Vector potential components.
t	Wave travel time; transit time.
x, y, z	Cartesian coordinate axes, same with (x_1, x_2, x_3).
u_x, u_y, u_z	Displacement components, same with (u_1, u_2, u_3).
σ_{zx}, σ_{zz}	Traction components (shear, normal).

ω	Angular frequency.
k	Wave number.
k_T	Wave number for transverse wave.
k_L	Wave number for longitudinal wave.
Δ	Determinant.
H, h, d	Thickness.
kH	Nondimensional wavenumber ($kH = k \cdot H$).
E	Young's modulus.
E_c	Compressive elastic modulus of concrete.
E_d	Dynamic modulus of concrete.
υ	Poisson's ratio.
∇^2	Laplace operator.
s	Spring constant (N/m^3).
θ	Wave incident angle.
f	Frequency.
D	Spatial distance.
$R(f)$	Fourier transform of time records.
$\bar{S}_{x1,x2}(f)$	Cross-power spectrum.
$\gamma^2(f)$	Coherence function.
$\bar{A}_{x1}(f), \bar{A}_{x2}(f)$	Averaged auto power spectra of time records.
ϕ	Phase shift.
F_{var}	Variance function.
$c_{exp}(i)$	Experimental phase velocity.

$c_{ant}^{modex}(i)$	Analytical phase velocity.
k_x	Wave vector component along the interface.
V_x, V_y, V_z	Particle velocity components.
α	Wave incident angle or reflected angle.
β	Wave refracted angle.
Δt	Time interval of wave groups.

TABLE OF CONTENTS

CHAPTER 1

INTRODUCTION

1.1 Background

During the service life of reinforced concrete (RC) slabs, damages and deteriorations can be caused due to overloading, aging, and corrosion. One of the reinforcement approaches is to add a steel plate on the bottom of a RC slab to enhance its flexural capacity, which is proven to be effective and low cost [Adhikary and Mutsuyoshi, 2002; Barnes et al., 2001; Vilnay, 1988; Taeljsten, 1997]. To make steel and concrete function more collaborative, epoxy is sometimes injected as adhesive into the interface between steel plate and concrete, together with anchor bolts [Shen et al., 2014; Ziraba and Baluch, 1995; Buyukozturk, 2004; Jones et al., 1982]. However, using epoxy as the adhesive will bring deterioration due to aging [Gélébart et al., 2007; Plonka et al., 2004]. Many factors like moisture absorption [Ferguson and Qu, 2006; Xiao and Shanahan, 1997], temperature elevation [Kajorncheappunngam, 2002], oxidation [Lafarie-Frenot et al., 2006], and photochemical degradation [Monney, 1998], all can cause aging problem to epoxy, leading to the decline of elastic modulus [Hu and Sun, 2000; Ferguson

and Qu, 2006], and the decrease of stiffness and yield stress [Mailhot, 2005; Vallo, 1993]. Long time of aging will cause even worse consequence: delamination or debonding on the interfaces [Murray et al., 2003; Buyukozturk et al., 2004].

To prevent the failure of adhesives, we need to estimate the material property of epoxy, so that the extent of the aging of the adhesive material in service can be assessed through the historical data comparison [Gélébart, 2007]. However, to maintain the functionality of the strengthened structure, directly cutting the plate and collecting the material is not allowed. Recently the Nondestructive Evaluation (NDE) technique is applied frequently in multi-layered bonding materials and composite materials [Yuan et al., 2008; Hosten et al., 2001; Lobkis et al., 2000], in particular, for detecting the delamination or the bonding quality of the layered media. Furthermore, through obtaining the phase velocity of surface wave propagating in the media using NDE, the elastic property of the adhesive material can be estimated properly [Wu and Chen, 1996]. For a material with aging problem like epoxy, knowing its material property before the occurrence of severe deterioration is significant in engineering. Therefore, a feasible detection method for elastic property of epoxy layer in the steel-epoxy-concrete bonding layered media is in demand to be developed.

If we call the estimation of epoxy's material property for the steel-epoxy-concrete multi-layered media is an early-time strategy for moderate-damaged structures, then for those structures of severe damaged state, we need to offer another proper evaluation method accordingly. It has been decades since the steel plate strengthening method for RC slabs was applied on infrastructures, hence quite a lot of the strengthened slabs have already met the problems of material's aging, layers' delamination, or even worse: water's invasion. If water penetrates into the top surface of a steel plate through an additionally damaged concrete slab, serious corrosion will be caused [Kotyaev et al., 2014; Tachibana et al., 2014]. Therefore, it is

of great importance to detect the existence of water layer in the steel-concrete or steel-epoxy-concrete layered media. Once the debonding starts, it will spread horizontally and enlarge vertical discontinuity between steel and concrete/epoxy. Then after the vertical deflection of a steel plate increases gradually, a catastrophic failure of RC slabs may happen at the final stage. Therefore, knowing the thickness and distribution area of the invaded water layer can help us to assess the severity of the debonding [Shen and Hirose, 2016].

Ultrasonic Testing (UT) is recently used to evaluate flaws in layered media [Su et al., 2006; Kim et al., 2007]. It has also been applied for the detection of water layer in multi-layered media in relative low frequency range [Kotyaev et al., 2014; Tachibana et al., 2014]. However, the Fourier analysis of the waveforms in low frequency has not succeeded in detecting the water layer [Yanagihara et al., 2015]. In high frequency range, on the other hand, received waveforms become relatively simple due to the isolation of each waveform. It is expected that the existence of water layer may be detected from the analysis of reflected waves in layered media.

1.2 Objectives

In this study, we will focus on the Ultrasonic Nondestructive Evaluation on the multi-layered media, specifically, on the steel-concrete and the steel-epoxy-concrete layered media. There are two main objectives to accomplish as we introduced in the background: firstly, we will propose an effective nondestructive approach to estimate the elastic property of epoxy layer in a steel-epoxy-concrete bonding composite media based on the wave dispersion theory in layered media; secondly, we will utilize the multi-reflection effect of oblique incident ultrasonic wave in the liquid layer to detect the penetrated water beneath the steel plate, including the water layer's existence, thickness and the distribution region. As we have already described, these two objectives are for two different damage levels of the steel plate strengthened RC slab. The former one is for the early or moderate damage level when the adhesive material's aging just initiates or starts to become severe, and the latter one is for the serious damage level when the delamination or debonding already occurred and probably so did the invasion of water.

Also, there are other objectives need to be achieved in this study:

1) Develop an effective algorithm for large scale equation solving and roots searching for dispersion curves' plotting.
2) Find a proper experimental approach to obtain good ultrasonic surface wave signals with high coherence and stability.
3) Develop an inversion process for material constants' optimization according to the analytical and experimental dispersion curves.
4) Simulate the wave propagation in the multi-layered specimen using Explicit Finite Element Method (EFEM) and obtain the numerical dispersion curve.
5) Calculate the reflection and refraction coefficients of liquid layer contained multi-

layered media.

6) Conduct oblique incident ultrasonic testing on different multi-layered configurations and find the optimal incident angle range.
7) Propose the identification approach of the region of water layer, and design effective testing procedures.

1.3 Organization of this Dissertation

There are eight chapters in this dissertation.

Chapter 2 is devoted for reviewing literatures related to this dissertation. It covers some important theoretical knowledge points and technical approaches which will be employed in this study. The related wave theories' development and their recent applications are introduced, and several NDE approaches for detection of multi-layered media and their effects are briefly described.

Chapter 3 focuses on the dispersion property of different multi-layered media, including free steel plate, steel-epoxy-concrete, steel-water-concrete, steel-spring-concrete, and steel-water-epoxy-concrete. All these types of multi-layered media are discussed in this dissertation. For example, steel-epoxy-concrete for the material property estimation in Chapter 4, and other water layer contained types for liquid detection in Chapter 6 and Chapter 7. Here, we firstly present the boundary conditions, and deduce the dispersion equations, then solve the equation to get the analytical dispersion curves, and also obtain the wave structure of different wave modes. In the end, the knowledge of Scholte is given for explaining the dispersion curves more properly.

Chapter 4 focuses on the material property estimation of multi-layered media. Firstly we discuss the influence factors to the modes and shapes of the dispersion curves. Then we conduct an ultrasonic NDE test on the casted steel-epoxy-concrete specimen following the idea of Spectral Analysis of Surface Waves (SASW), by which the experimental dispersion curves can also be plotted. Through the inversion process of the analytical and experimental dispersion curves, we can successfully estimate the elastic property of epoxy layer. Then based on the estimated elastic constants, we simulate wave's propagation in the steel-epoxy-concrete layered media using Explicit Finite Element Method (EFEM), from which the numerical

dispersion curves are obtained.

Chapter 5 turns the study back to the theoretical work again, focusing on wave's reflection and refraction (transmission) in multi-layered media, which is the theory basis of the application in Chapter 6 and Chapter 7. We firstly deduce the reflection factor equation and then calculate the reflection and transmission coefficients of multi-layered (liquid layer included) media. Four interfaces that would appear in the following experiment are emphasized here: steel-water, water-steel, water-concrete and water-epoxy.

Chapter 6 focuses on the water layer detection in the multi-layered media, specifically, the steel-water-concrete and steel-water-epoxy-concrete media. In this chapter, we develop an ultrasonic nondestructive approach based on obliquely incident ultrasonic wave's multi-reflection to detect liquid layer beneath a solid layer. Firstly, experiments on multi-layered configurations are conducted with different water layer thicknesses and bottom layer materials. By analyzing the experimental results, the existence of water layer can be clearly distinguished. Through comparison with the theoretical wave travelling time in the water layer, the thickness of the water layer can be estimated from the time interval of reflected wave groups.

Chapter 7 is an extension of the topic in Chapter 6, to identify the region of the liquid layer beneath the solid layer. Firstly an approach of identification and its procedures are presented. Then the relative NDE tests are conducted on the casted multi-layered specimen to confirm every step of the identification to be feasible.

Chapter 8 concludes the research with several points and gives some recommendations for the Ultrasonic Nondestructive Evaluation on the multi-layered media like the steel plate strengthened RC slab, and also provides some possible future developments of this research.

CHAPTER 2

REVIEW OF RELATED LITERATURE

2.1 Introduction

Numbers of literatures have been reviewed about the theoretical research and technical nondestructive approach for multi-layered media. In the theoretical part, two research topics are included. The first one is about dispersion curves, which is the basis of almost all the researches about multi-layered media. It has been studied and calculated since decades ago [Ewing et al., 1957], but its application is still being widely employed in many ways. The second one is about reflection and refraction on the interfaces of multi-layered media. It is also a traditional field firstly been considered in optic science. However, using the phenomenon of multiple reflection and refraction in nondestructive detection is still rarely to be seen currently. In the technical part, three topics are mentioned: about material property estimation; about surface wave method; about leaky waves method. The material property estimation is one of the objectives of this dissertation, and the other two are the common used NDE approaches for multi-layered media. The reviewed literatures are the knowledge basis of this dissertation, also some kind of guidance to the objectives we have made.

2.2 Theoretical Research of Multi-layered Media

Before conducting the nondestructive evaluation on multi-layered media, the theories of wave's dispersion and reflection in the layered media are firstly needed to be studied. There are quite a lot of relative researches about these two topics.

2.2.1 Dispersion Curve

When wave propagates in multi-layered media with variant material property, its phase velocity varies with the frequency, namely, dispersive. The phenomenon of wave dispersion in bonding layered media needs to be studied well because the composite media with different materials will have significantly different dispersion properties. [Tsai et al., 2001] engaged in a research of surface wave dispersion in a copper-epoxy-aluminum composite specimen, and obtained dispersion curves with different elastic property and thickness of epoxy layer. [Puthillath and Rose, 2010] utilized ultrasonic guided wave for inspection of interfacial weakness conditions in an epoxy bonded aluminum-titanium repair patches. They also carried out a theoretical study where the guided wave phase velocity dispersion curves are used in conjunction with wave structures to determine optimal conditions for inspection of adhesive and cohesive weakness. [Lee and Cheng, 2001] presented a method for measuring Lamb wave dispersion curves of a bi-layered plate and to investigate the feasibility of using Lamb wave dispersion data to determine a coating's elastic properties. Some researchers [Ryden and Lowe, 2004] also conducted research and field test in multi-layered pavement structures, in which the dispersion property is under another description. [Zhang and Lu, 2003; Zhang et al., 1998] calculated several cases of dispersion curves of 3-layer composite material with different layer properties, revealed that even a slight alteration on the elastic constants of one of those layers would significantly affect wave's dispersion property. Some researchers also considered the dispersion when the media contained a liquid layer, but most of them only considered the case

that a liquid layer overlying a semi-infinite elastic solid [Tolstoy, 1954; Dorman, 1962] or multi-layered solid [Shao et al., 2007; Jardetzky and Press, 1953], for the simulation of suboceanic ground layers. [Parra and Xu, 1994] analyzed the sensitivity of phase and group velocity as well as attenuation to input parameters (e.g. permeability, porosity, layer thickness, etc.), when acoustic waves propagating in fully saturated layer media, and proposed an algorithm for complex roots finding of dispersion equation. The analysis of dispersion property and plotting of dispersion curves are so important for wave analysis of multi-layered media. The media's parameters, e.g. elastic constants, layer thickness, stratification type, existence of solid-liquid interface, can all exert influence on the curves sensitively. Therefore, knowing the dispersion property of the multi-layered media is the basis of all other research on them.

2.2.2 Reflection and Refraction

The detection of water layer in multi-layered media requires comprehensive knowledge about the wave propagation, reflection, and refraction in layered media. The reflection and refraction of an obliquely incident wave on the interface between two different media has been investigated by [Pilarski and Rose, 1988; Pilarski et al., 1990; Auld, 1973], where solid-solid, solid-liquid, and liquid-solid boundary conditions were considered and reflection factor equations were derived. The reflection and transmission of ultrasonic waves in multi-layered solid media also have been studied [Folds and Loggins, 1977]. [Schoenberg, 1980] computed the reflection and transmission coefficients for harmonic plane waves incident at arbitrary angles upon a plane linear slip interface in terms of the interface compliance, and found these coefficients be frequency dependent. [Henneke, 1972] extended the classical elastic theory of reflection and refraction at an interface to the anisotropic media. The critical angle of the oblique incidence around which the reflection and refraction can vary strongly has also been studied by some researchers. [Ngoc and Mayer, 1979] calculated the profiles for different

combinations of frequencies and beam widths with the angle of incidence being varied about the longitudinal critical angle for a water-Plexiglas interface, and found the existence of nonspecular reflectivity near this particular critical.

Although the theoretical work of reflection and refraction on interfaces has been conducted decades ago, the applications of multi-reflection of acoustic or ultrasonic waves in practical work are still rarely to be seen recently. [Schmitt et al., 2013] introduced an acoustic waveguide sensor based on multiple reflection and mode conversion on solid-liquid interfaces. The author excited the anti-symmetrical zero order Lamb wave mode by a single phase transducer of 1 MHz on thin glass plates of 1 mm thickness. By contact to the investigated liquid, Lamb waves propagating on the first plate emit pressure waves into the adjacent liquid, which excite Lamb waves on the second plate, what again cause pressure waves traveling inside the liquid back to the first plate and so on. Because of the distance of the two plates, the slow sound velocity of water and the fast Lamb wave velocity, the wave groups of the receiver signal are separated in the time domain. Fig. 2.1 shows the guided wave's propagation in the liquid layer between two plates. This phenomenon was employed in the sensor for the concentration measurement of binary and ternary mixtures, liquid level sensing, and investigation of spatial inhomogeneity or bubble detection.

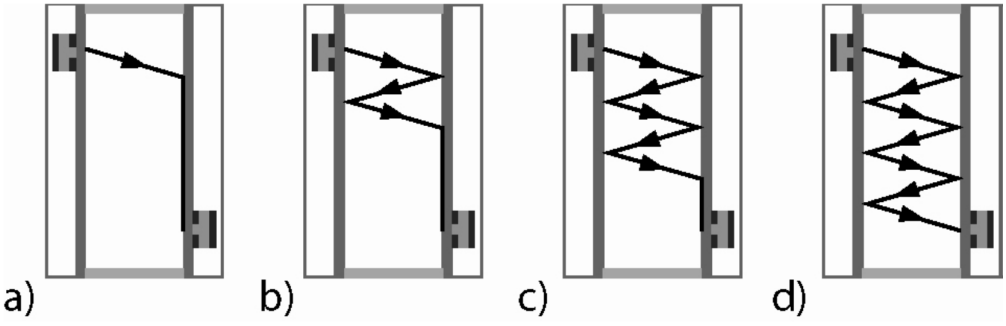

Fig. 2.1 The propagation path of the emitted pressure wave into the liquid by Lamb wave excitation on the emitter plate

From the review of those former researches, we can remark that the reflection and transmission coefficients can be theoretically calculated, with which the properties of interfaces between different layers can be evaluated. The reflection and refraction angles and wave travelling route in multi-layered media can be determined by Snell's law [Rose, 1999]. Therefore, we can plot the travelling routes of obliquely incident ultrasonic waves as well as energy distribution and penetration in the multi-layered media containing a liquid layer. The method based on multi-reflection of shear waves has been applied to the detection of the thickness loss of a solid layer by [Volker and Zon, 2013; Burch and Collett, 2007]. However, the multi-reflection method has not yet been applied to the evaluation of multi-layered media. In this study, we will use wave's multiple reflection and transmission in detecting the existence of liquid layer beneath a solid layer.

2.3 Nondestructive Testing of Multi-layered Media

Besides the theoretical research, the technical approaches and recent achievements about the NDE for multi-layered media are also necessary to be reviewed and studied. Three aspects of the most relative literatures have been introduced here.

2.3.1 Material Property Estimation

To estimate material's elastic properties is often an inescapable task in the nondestructive testing. Compared to the geometrical flaws, the deteriorations on the material properties are sometimes more difficult to be noticed and detected. For a free plate or a solid block that the opposite surfaces can be both reached, the measurement of the wave velocity in that media can be easily achieved [Gélébart et al., 2007; Naffa et al., 2002; Rogers, 1995]. However, for multi-layered media that only the top surface of the first layer can be reached, the estimation of the material property of the buried layers is difficult. Most researches about this topic are all based

on the utilization of the dispersion curves. [Tsai et al., 2001; Wu and Chen, 1996; Wu and Liu, 1999] used laser generated dispersive surface waves for detecting the epoxy layer's material constants and thickness of an epoxy bonded copper-aluminum layered specimen. [Lobkis et al., 2000] presented a method to deduce the in-plane elastic properties of multi-layered composite plates. Drawing on a synthetic-aperture technique developed for the elucidation of materials properties in air-coupled ultrasonic, this method exploited the high elastic anisotropy of composite materials to permit an accurate measurement of directional in-plane stiffness. [Xu et al., 1990] presented a systematic inversion scheme to determine the cohesive properties of adhesive bonds from guided wave phase velocity data. They mentioned that the inaccurate or false data had a strong negative influence on the success of the inversion scheme. From these former researches we can find, all of the experimental studies almost set their target multi-layered media as homogeneous and isotropic for all the layers. Therefore, to conduct the material property estimation on multi-layered media like steel-epoxy-concrete, where the concrete is inhomogeneous and anisotropic, by seriously taken, would be rather challenging.

2.3.2 Surface Wave Method

The experimental data obtained from the surface wave NDE test are wave form data in time domain. Two wave forms from two receivers on two spots with certain distance contain the phase information if they are transformed into frequency domain. With the known distance and phase shift between the two wave forms at each frequency, the experimental dispersion curve can be plotted. This Spectral Analysis of Surface Wave (SASW) method has been used successfully to determine shear wave velocity profiles of soil sites and elastic properties of pavement systems [Nazarian and Desai, 1993]. The frequency-domain functions used in SASW method are the phase information of the cross-power spectrum and the coherence function.

This SASW method will be applied in this study for experimental dispersion curve obtaining.

The calculated dispersion curve of multi-layered solid model can describe the wave dispersion in the bonding layered media analytically. Through generated surface wave test, an experimental dispersion curve is able to be obtained, from which a relation between phase velocity and frequency can be discovered. Through the comparison between the analytical dispersion curve and the experimental one, layer's elastic property can be estimated. The surface wave method was originally applied in geotechnical research [Nazarian and Desai, 1993; Yuan and Nazarian, 1993; Ganji et al., 1998; Park, 1996]. Usually a vibrator or a hammer and several geophones were used as source and receiver respectively, with the wave frequency under 100Hz. Also, pavement structures were usually tested through this method [Ryden and Lowe, 2004], with the frequency normally under 500Hz. Acoustic waves of low frequency are the main wave form in the both types of test. This surface wave method has also been applied in high frequency range (500kHz~4000kHz), for layered metal specimens [Wu and Liu, 1999], with laser generated wave as source. In both low and high frequency range, this method can be applied successfully, however, in the frequency range about 10kHz~300kHz, which is an approximately range for steel-concrete composite material, rare work has been done. The ultrasonic transducer with its operating frequency around 200kHz will be suitable for the surface wave test on the steel-epoxy-concrete bonding layered media, but the material concrete's anisotropy and inhomogeneity will challenge the effect of ultrasonic NDE test. For material like concrete, which is significantly important in infrastructure construction, nevertheless, the NDE attempts are few and always not easy [Antonio and Hirose, 2012; Goueygou et al., 2004; Piwakowski et al., 2004]. The ultrasonic NDE study on layered media which consists of concrete has even fewer been concerned yet, although, in many fields, it is urgently to be conducted.

2.3.3 Leaky Lamb Wave and Leaky Rayleigh Wave

When the multi-layered media contains liquid layer inside, due to the particle displacement normal to the plate, waves are also set up in the surrounding liquid. This is the mechanism by which energy "leaks" from the plate into the liquid; hence, the term "leaky Lamb wave" [Dayal and Kinra, 1989; Dayal and Kinra, 1991]. When the solid layer is thick, the Rayleigh wave propagating on the interface can also leak into the liquid, which is called "leaky Rayleigh wave" [Ahyi et al., 1998]. These leaky waves are the results of the existence of the solid-liquid interface. They can also be used as a nondestructive approach to detect the defects or to estimate the material property of a solid plate surrounded by liquid. [Chimenti and Nayfeh, 1985; Chimenti and Martin; 1991] presented the results of experimental measurements and theoretical calculations on ultrasonic leaky Lamb wave propagation in fiber-reinforced, unidirectional composite laminates. With the Lamb wave vector oriented parallel to the fiber direction, dispersion curves of phase velocity versus frequency and plate thickness were constructed from measurements of ultrasonic reflection from fluid-loaded composite plates. [Karim et al., 1990] presented a numerical procedure for the inversion of leaky Lamb wave data to determine certain material properties of a waveguide using a modified version of the simplex algorithm. Similar inversion scheme was presented by [Xu et al., 1990] to determine the cohesive properties of adhesive bonds from leaky Lamb wave phase velocity data.

2.4 Summary

According to the research objectives of this dissertation, the most relevant literatures have been reviewed in this chapter. Some of those papers will be cited again in the following chapters, which are locally helpful to this dissertation.

CHAPTER 3

WAVE DISPERSION IN LAYERED MEDIA

3.1 Introduction

When wave propagates in multi-layered media with variant material property, its phase velocity varies with the frequency, namely, dispersive. The phenomenon of wave dispersion in bonding layered media needs to be studied well because the layered media with different materials will have significantly different dispersion properties. In this chapter, the dispersion property of a free plate will be firstly discussed, in order to present the detailed process of dispersion equation deduction and roots searching algorithm for dispersion equation solving. Then the cases of solid multi-layered media, and liquid contained multi-layered media will be discussed in sequence. For each case, the boundary conditions will be listed; the dispersion equation will be deduced; the dispersion curves will be plotted; the wave structure of each wave mode will be analyzed. In the end of this chapter, we will use spring to replace non-viscous liquid layer to see whether the effect of a liquid layer between solid layers can be simplified as a normal connection between them. Also, we will briefly introduce Scholte wave as it is born with the solid-liquid interface. The theoretical results of this chapter will be utilized in Chapter

4 and Chapter 6.

To deduce the dispersion equation, we need to recall the following equations from the theory of elasticity.

3 equations of motion (i = 1,2,3):

$$\sigma_{ij,j} + \rho f_i = \rho \ddot{u}_i \tag{3.1}$$

6 independent strain displacement equations:

$$\varepsilon_{ij} = \frac{1}{2}\left(u_{i,j} + u_{j,i}\right) \tag{3.2}$$

6 independent constitutive equations (isotropic materials):

$$\sigma_{ij} = \lambda \varepsilon_{kk} \delta_{ij} + 2\mu \varepsilon_{ij} \tag{3.3}$$

If we eliminate the stress and strain factors from these equations, then we have:

$$\mu u_{i,jj} + (\lambda + \mu) u_{j,ji} + \rho f_i = \rho \ddot{u}_i \tag{3.4}$$

The equations of motion (3.4), which contain only the particle displacements, are the governing partial differential equations for displacement. If the domain in which a solution is sought is infinite, then these equations are sufficient. If the domain is finite, then boundary conditions are needed for a well-posed problem [Rose, 1999].

3.2 Wave Dispersion in Free Plate

Before we look into the dispersion property of multi-layered media, we shall start from the wave's dispersion in a free plate, which is the simplest and most classic case. From this case, we can have the general idea about how the dispersion equation can be deduced, how the dispersion curves can be plotted, and what the wave structure of each mode is.

3.2.1 Dispersion Equation Deduction

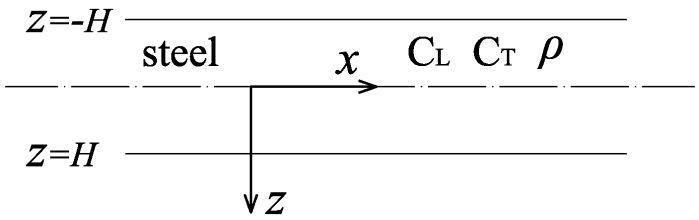

Fig. 3.1 A steel plate in vacuum.

If the displacement vector (field) is decomposed according to Helmholtz decomposition [Achenbach, 1980] and the result substituted into Eq. (3.4), as demonstrated previously, we obtain two uncoupled wave equations [Ewing et al., 1957; Rose, 1999]. For plane strain, these are

governing longitudinal waves:

$$\frac{\partial^2\varphi}{\partial x^2}+\frac{\partial^2\varphi}{\partial z^2}=\frac{1}{{c_L}^2}\cdot\frac{\partial^2\varphi}{\partial t^2} \tag{3.5}$$

governing transverse waves:

$$\frac{\partial^2\psi}{\partial x^2}+\frac{\partial^2\psi}{\partial z^2}=\frac{1}{{c_T}^2}\cdot\frac{\partial^2\psi}{\partial t^2} \tag{3.6}$$

where the potentials φ and ψ are solutions of the wave equations, and c_L and c_T are the longitudinal wave velocity and transverse wave velocity respectively. For simplicity of notation the subscript *y* has been omitted from ψ in Eq. (3.6).

As a result of our assumption of plane strain, the displacements and stresses can be written in terms of the potentials as:

$$u_x=\frac{\partial\varphi}{\partial x}-\frac{\partial\psi}{\partial z} \tag{3.7}$$

$$u_z=\frac{\partial\varphi}{\partial z}+\frac{\partial\psi}{\partial x} \tag{3.8}$$

$$\sigma_{zx}=\mu\left(\frac{\partial u_z}{\partial x}+\frac{\partial u_x}{\partial z}\right)=\mu\left(2\frac{\partial^2\varphi}{\partial x\partial z}-\frac{\partial^2\psi}{\partial z^2}+\frac{\partial^2\psi}{\partial x^2}\right) \tag{3.9}$$

$$\sigma_{zz} = \lambda\left(\frac{\partial u_x}{\partial x} + \frac{\partial u_z}{\partial z}\right) + 2\mu\frac{\partial u_z}{\partial z} = (\lambda + 2\mu)\nabla^2\varphi - 2\mu\left(\frac{\partial^2\varphi}{\partial x^2} - \frac{\partial^2\psi}{\partial x \partial z}\right) \qquad (3.10)$$

Now let us consider the simplest case of a homogeneous plate bounded by two parallel planes. The plate can have either finite or infinite dimensions, and we now restrict ourselves to the latter case, which satisfy four boundary conditions at the upper and lower surfaces of the plate. These conditions express the fact that the stresses vanish at the faces $z = -H$ and $z = H$ (the thickness of the plate is denoted by $2H$ and the median plane by $z = 0$). Then we have

$$\sigma_{zz} = 0 \quad ; \quad \sigma_{zx} = 0 \qquad at\ z = \mp H \qquad (3.11)$$

We begin the analysis by assuming solutions to Eq. (3.5) and Eq. (3.6) in the form

$$\varphi = (A\,sinh\,\nu z + B\,cosh\,\nu z)e^{i(\omega t - kx)} \qquad (3.12)$$

$$\psi = (C\,sinh\,\nu' z + D\,cosh\,\nu' z)e^{i(\omega t - kx)} \qquad (3.13)$$

where,

$$\nu = \sqrt{k^2 - k_L^2} \qquad \nu' = \sqrt{k^2 - k_T^2} \qquad k_L = \frac{\omega}{c_L} \qquad k_T = \frac{\omega}{c_T} \qquad (3.14)$$

Noting that ${c_L}^2 = (\lambda + 2\mu)/\rho$, ${c_T}^2 = \mu/\rho$ and inserting expressions (3.12) and (3.13) into Eqs. (3.7)~(3.11), we obtain the four boundary conditions in the form:

$$(\rho\omega^2 - 2\mu k^2)(A\sinh\nu H - B\cosh\nu H) - 2i\mu k\nu'(C\cosh\nu' H - D\sinh\nu' H) = 0$$

$$2ik\nu(A\cosh\nu H - B\sinh\nu H) - \left({\nu'}^2 + k^2\right)(C\sinh\nu' H - D\cosh\nu' H) = 0$$

$$-(\rho\omega^2 - 2\mu k^2)(A\sinh\nu H + B\cosh\nu H) - 2i\mu k\nu'(C\cosh\nu' H + D\sinh\nu' H) = 0$$

$$2ik\nu(A\cosh\nu H + B\sinh\nu H) + \left({\nu'}^2 + k^2\right)(C\sinh\nu' H + D\cosh\nu' H) = 0 \qquad (3.15)$$

The dispersion equation is obtained in a simpler form if we write the columns corresponding to the coefficients A, D, B, C, add the first line of the determinant to the third, and subtract the second from the fourth. Then, on putting

$$a = 2\mu k^2 - \rho\omega^2 = \mu(2k^2 - k_T^2) = \mu\left(\nu'^2 + k^2\right)$$

$$b = 2\mu k\nu' \cosh \nu' H \qquad d = 2\mu k\nu' \sinh \nu' H \tag{3.16}$$

we have

$$\Delta \times (A, D, B, C)^T = 0 \tag{3.17}$$

where

$$\Delta = \begin{vmatrix} -a\sinh \nu H & id & a\cosh \nu H & -ib \\ -2ik\nu \cosh \nu H & -\left(\nu'^2 + k^2\right)\cosh \nu' H & 2ik\nu \sinh \nu H & \left(\nu'^2 + k^2\right)\sinh \nu' H \\ 0 & 0 & 2a\cosh \nu H & -2ib \\ 0 & 0 & -4ik\nu \sinh \nu H & -2\left(\nu'^2 + k^2\right)\sinh \nu' H \end{vmatrix} \tag{3.18}$$

The four variables A, D, B, C must have values different from zero, and therefore we obtain the dispersion equation:

$$\Delta = 0 \tag{3.19}$$

Obviously this equation can be split into two. They are

$$(\rho\omega^2 - 2\mu k^2)\left(\nu'^2 + k^2\right)\sinh \nu H \cosh \nu' H + 4\mu k^2 \nu\nu' \cosh \nu H \sinh \nu' H = 0 \tag{3.20}$$

and

$$(\rho\omega^2 - 2\mu k^2)\left(\nu'^2 + k^2\right)\cosh \nu H \sinh \nu' H + 4\mu k^2 \nu\nu' \sinh \nu H \cosh \nu' H = 0 \tag{3.21}$$

By Eqs. (3.14), these equations take the form [Ewing et al., 1957; Rose, 1999]:

$$\frac{tanh\, \nu H}{tanh\, \nu' H} = \frac{4k^2 \nu\nu'}{\left(\nu'^2 + k^2\right)^2} = \frac{4\sqrt{1 - c^2/{c_L}^2}\sqrt{1 - c^2/{c_T}^2}}{(2 - c^2/{c_T}^2)^2} \tag{3.22}$$

and

$$\frac{tanh\, \nu H}{tanh\, \nu' H} = \frac{\left(\nu'^2 + k^2\right)^2}{4k^2 \nu\nu'} = \frac{(2 - c^2/{c_T}^2)^2}{4\sqrt{1 - c^2/{c_L}^2}\sqrt{1 - c^2/{c_T}^2}} \tag{3.23}$$

Now the transformation of the determinant Δ which preceded its representation in the form of a product is equivalent to the splitting of Eqs. (3.15) into two separate systems. It is easy to see that the coefficients A and D can be separated from B and C. Thus we can consider a motion symmetric with respect to the plane $z = 0$ which is given by

$$\varphi = B\, cosh\, \nu z\, e^{i(\omega t - kx)} \qquad \psi = C\, sinh\, \nu' z\, e^{i(\omega t - kx)} \tag{3.24}$$

and the antisymmetric motion represented by functions

$$\varphi = A\, sinh\, \nu z\, e^{i(\omega t - kx)} \qquad \psi = D\, cosh\, \nu' z\, e^{i(\omega t - kx)} \tag{3.25}$$

In both cases the nature of the vibrations is determined by the corresponding dispersion equation, i.e., by (3.23) for the symmetric and by (3.22) for the antisymmetric case. Both equations contain two variables, wavenumber k and phase velocity c. Hence, by solving the dispersion equations (3.22) and (3.23), we can plot dispersion curves of symmetric modes and antisymmetric modes respectively, which present the relationship between wavenumber (frequency) and phase velocity.

The dispersion curves are very important in the analysis of wave propagation in layered media, especially from the aspects of wave mode. For different configurations of multi-layered media, the deduction of the dispersion equations can be started with some general assumptions of plane waves propagating in the media.

For a solid layer, both longitudinal wave and transverse wave can propagate in the layer and both waves can be reflected by the bottom interface, so the plane wave needs to be expressed with two components of potential φ and ψ for longitudinal wave and transverse wave accordingly, and each component is composed of two terms for two directions of wave propagation due to reflections on the surfaces or the interfaces. Hence, the potential of a solid layer can be assumed as the form with 4 unknown parameters:

$$\varphi = Ae^{i(\omega t - kx) - \nu z} + Be^{i(\omega t - kx) + \nu z} \tag{3.26}$$

$$\psi = Ce^{i(\omega t - kx) - \nu' z} + De^{i(\omega t - kx) + \nu' z} \tag{3.27}$$

For a solid half space, the wave cannot be reflected by the bottom surface. Therefore, it contains only one term in each potential component, with 2 unknown parameters totally. The potential can be written as:

$$\varphi = Ae^{i(\omega t - kx) - \nu z} \tag{3.28}$$

$$\psi = Ce^{i(\omega t - kx) - \nu' z} \tag{3.29}$$

For a liquid layer, the potential has only longitudinal component with 2 unknown parameters:

$$\varphi = Ae^{i(\omega t - kx) - \nu z} + Be^{i(\omega t - kx) + \nu z} \tag{3.30}$$

For a liquid half space, since no wave can be reflected, the potential can be written as:

$$\varphi = Ae^{i(\omega t - kx) - \nu z} \tag{3.31}$$

After making these assumptions, we can substitute these expressions into Eqs. (3.7)～(3.10), and consider the boundary conditions on the surfaces and each interfaces. Then the

dispersion equation can be obtained from the boundary equations by order the determinant equal to zero, with a more generalized form as:

$$\Delta = \begin{vmatrix} (2k^2 - k_T^2) & (2k^2 - k_T^2) & 2k\nu' & -2k\nu' \\ 2k\nu & -2k\nu & (2k^2 - k_T^2) & (2k^2 - k_T^2) \\ (2k^2 - k_T^2)e^{-\nu H} & (2k^2 - k_T^2)e^{\nu H} & 2k\nu' e^{-\nu' H} & -2k\nu' e^{\nu' H} \\ 2k\nu e^{-\nu H} & -2k\nu e^{\nu H} & (2k^2 - k_T^2)e^{-\nu' H} & (2k^2 - k_T^2)e^{\nu' H} \end{vmatrix} = 0 \quad (3.32)$$

The specific form of the dispersion equations of different configurations of layered media will be shown in the following sections.

3.2.2 Roots Searching Algorithm

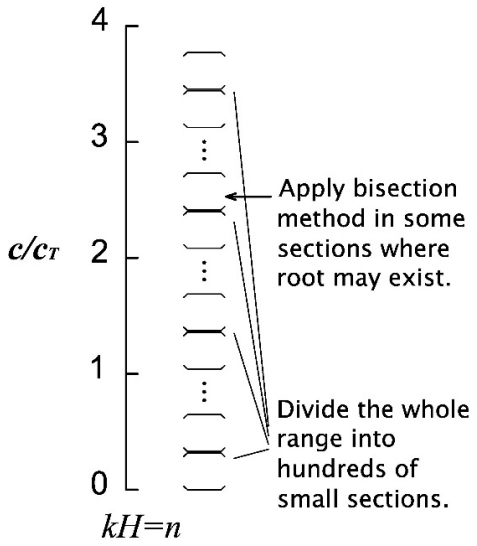

Fig. 3.2 Diagram of the bisection method based algorithm for roots searching.

In this case of solid plate in vacuum, the dispersion equations Eq. (3.22) and Eq. (3.23) have only two terms each, however, when the number of layers of the media increases, the dispersion equation will become very complicated. To obtain the dispersion curves from the dispersion equation, we need a reliable and effective algorithm to search for the roots of the equation. In this study, an upgraded bisection method based algorithm is proposed for multi-roots searching. Here we need to firstly declare that, in order to eliminate the influence of material property and layer thickness to the axes value, we employ the nondimensional

variables c/c_T and kH instead of c and k in dispersion equations Eq. (3.22) and Eq. (3.23). We will sweep the concerned range of kH by certain interval, e.g. 0.01, to find the according roots on each kH value, and those roots stand for the points on different modes of the dispersion curves. Connecting those roots along the kH axis under the correct order is actually the plotting of dispersion curves. The following procedures explain the detail of the algorithm for roots searching, and Fig. 3.2 shows the diagram of this algorithm.

Step 1: Substitute one known value of kH into the dispersion equation $\Delta = 0$.

Step 2: Divide the whole target range of c/c_T (normally 0～4) into hundreds of small sections.

Step 3: Check each section, if the absolute value of Δ on the center point of this section is smaller than both section ending points, then this section contains a root.

Step 4: Apply absolute value based bisection method in those sections that meet the root existing requirement of Step 3.

Step 5: During the loops of the bisection method, when the absolute value of Δ on one center point is smaller than the critical value ε, then the root in that section is found.

Step 6: Collect all the roots found on this kH value, and move on to the next value of kH.

This method can successfully find all the roots of the dispersion equation in the concerned frequency range. However, for multi-layered media problem whose dispersion equation have forms of high order complex value determinant, to calculate the value of the determinant is not so easy. Especially on relative high frequency range, the absolute value of the determinant Δ is not close to zero, to which it should be equal. In that case, using minimum value instead of "zero" value is necessary, in another word, the choosing of the critical value ε becomes significant.

3.2.3 Dispersion Curves Plotting

Fig. 3.3 shows the dispersion curves of a steel plate in vacuum, the material constants are listed in Table 3.1. Both symmetric modes (S modes plotted with red curves) and antisymmetric modes (A modes plotted with blue curves) are plotted together. In Fig. 3.3 we can see that only the A0 mode originates from the zero point. The S0 mode originates from the plate velocity c, which is equal to $E^{1/2}[\rho(1-\upsilon^2)]^{-1/2}$ [Rose, 1999], where E is the Young's modulus, and υ is Poisson's ratio. All the other modes have cutoff frequency, before which the mode do not exist. As the convergence velocity when the kH value (frequency) becomes large, the A0 and S0 modes converge to c_R, the Rayleigh wave velocity, and all the other modes converge to c_T, the transverse wave velocity. The dispersion curves of a plate in vacuum has a quite "standard" form, which can be used for comparison with those of layered media, which will be discussed in the following sections.

Table 3.1 Material constants of the steel plate.

Material	C_L (m/s)	C_T (m/s)	ρ (kg/m^3)
Steel	5870	3140	7800

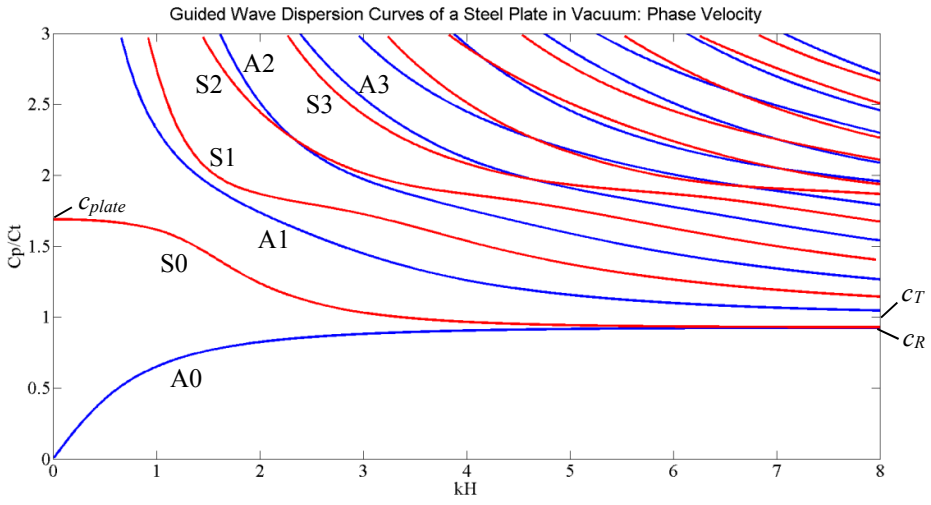

Fig. 3.3 Dispersion curves of a steel plate in vacuum (phase velocity): blue curves, antisymmetric modes; red curves, symmetric modes.

The quantity $c_g = d\omega/dk$, defining the velocity of a group of waves having angular frequency ω_0, is known as the group velocity. It can be expressed by a form of phase velocity c and wave number k as [Ewing et al., 1957]:

$$c_g = c + k\frac{dc}{dk} \tag{3.33}$$

Hence, as long as we have the dispersion curves of phase velocity, we can also plot the dispersion curves of group velocity by knowing the numerical derivative of c with respect to k. Fig. 3.4 shows the dispersion curves (c_g/c_T vs. kH) of a steel plate in vacuum.

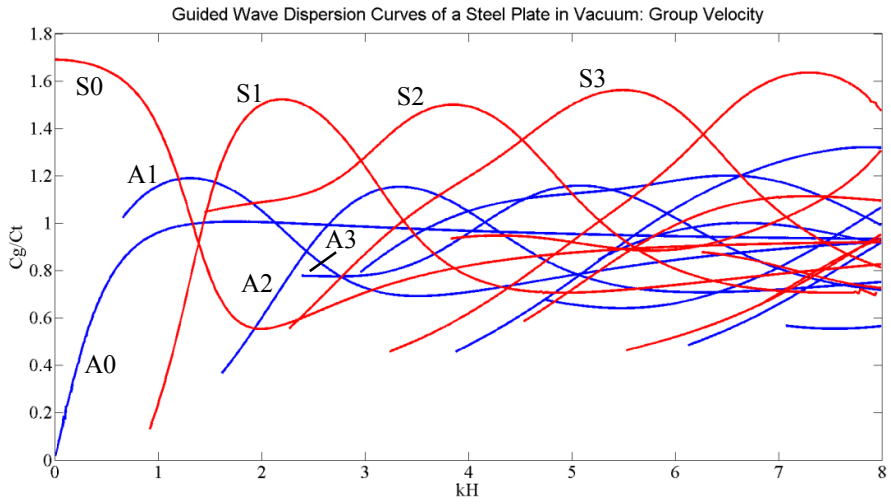

Fig. 3.4 Dispersion curves of a steel plate in vacuum (group velocity): blue curves, antisymmetric modes; red curves, symmetric modes.

If we put the curves of phase velocity and group velocity of the same wave mode together, we can have Fig. 3.5 and Fig. 3.6, for antisymmetric modes and symmetric modes respectively. By this way, we can compare the phase velocity and group velocity of the same wave mode easily.

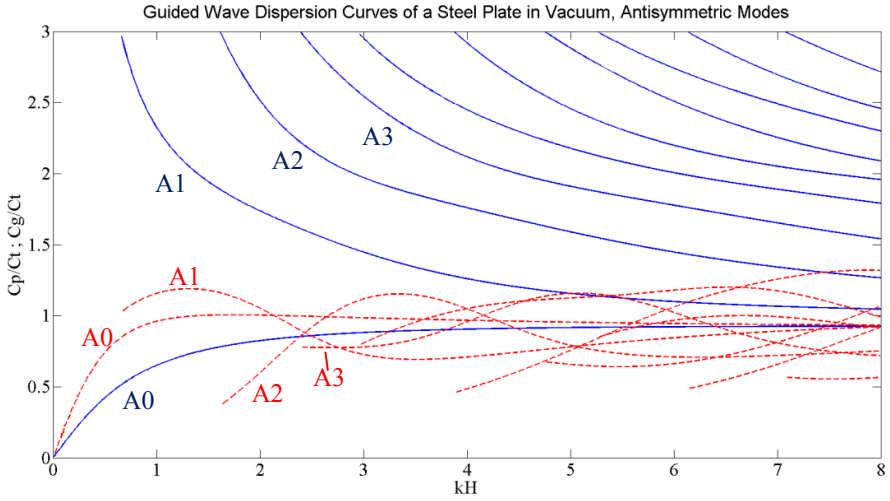

Fig. 3.5 Dispersion curves of a steel plate in vacuum (antisymmetric modes): blue curves, phase velocity; red curves, group velocity.

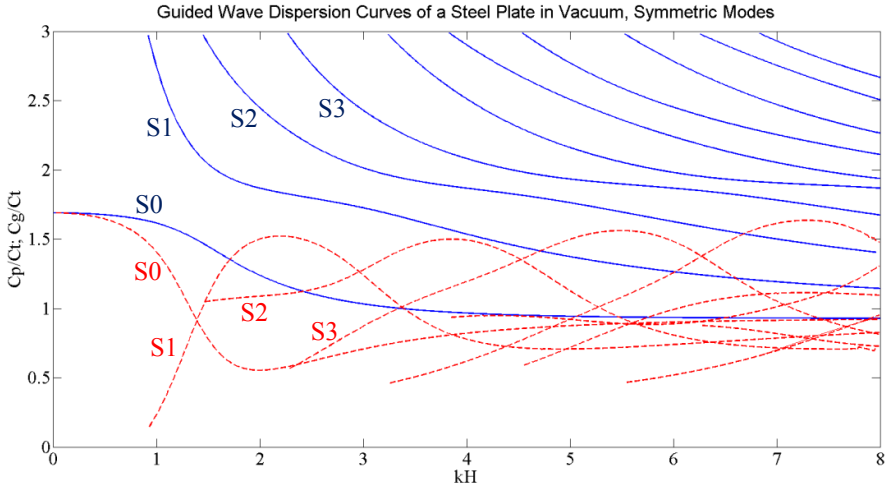

Fig. 3.6 Dispersion curves of a steel plate in vacuum (symmetric modes): blue curves, phase velocity; red curves, group velocity.

3.2.4 Wave Structure Analysis

By deducing the dispersion curves, we obtain the phase velocities of variant modes on the same kH value. When we feedback those value pairs into the boundary condition equations Eq. (3.15) or Eq. (3.17), we can solve those equations and obtain the values of the unknown parameters A, D, B, and C. By substituting these parameters into Eq. (3.12), Eq. (3.13) and Eq. (3.7), Eq. (3.8), we can obtain the corresponding displacements of each wave mode on different frequencies (kH) on each point in the plate (layer, in the case of multi-layered media), in other words, the wave structure of each mode.

It is interesting to study wave structure variation by increasing the kH product along a particular mode [Hayashi et al., 2006; Rose, 1999]. Fig. 3.7 to Fig. 3.12 depict solutions at a variety of kH values to modes S0, S1, S2, A0, A1, and A2 for a steel plate. The material constants of the plate are shown in Table 3.1. Sample kH points are chosen for each mode to show the variation in wave structure when kH value, namely, frequency increases. Displacements u and w are the displacements on x and z directions accordingly.

For example, in S0 mode (see Fig. 3.7), the displacement u differs not so much across the thickness of the plate at very low kH values ($kH = 0.25$), but it becomes heavily concentrated at the center of the plate when the kH values increase. In contrast, the displacement w, which is initially close to linear distribution, has a small displacement value on the outer surface (see Fig. 3.7 (a)). However, w becomes larger than u on the outer surface when $kH = 1$ (Fig. 3.7 (b)), and at $kH = 1.5$ (Fig. 3.7 (c)) and $kH = 2$ (Fig. 3.7 (d)) becomes dominant. In S1 mode (see Fig. 3.8), u concentrates its amplitude at the center of the plate when the kH value are small (Fig. 3.8 (a) and (b)). When the kH value goes high, the wave structure of both displacement components become more curving. We also notice that u component is always symmetric with the center axis of the plate ($H = 0$), oppositely, the w

component is always antisymmetric, denoting a stretch or compression force along the vertical axis of the plate. In S2 mode (see Fig. 3.9), the w component goes from dominant to zero on displacement value of outer surface when kH changes from 1.5 to 4. From S0 mode to S2 mode, we can find that the wave structures become more curving and complicated. From the curves' shape, we can easily distinguish each mode on the same kH value, which will be very useful in mode selection.

Similar studies are graphed for the antisymmetric modes in Fig. 3.10, Fig. 3.11, and Fig. 3.12. In this section, all the analysis are based on a steel plate in the vacuum, hence the symmetric or antisymmetric property of the wave structure along the center axis of the plate is very good. In the following sections, multi-layered media will be studied with different layers even liquid layer, the perfect symmetric or antisymmetric performance can no longer be found.

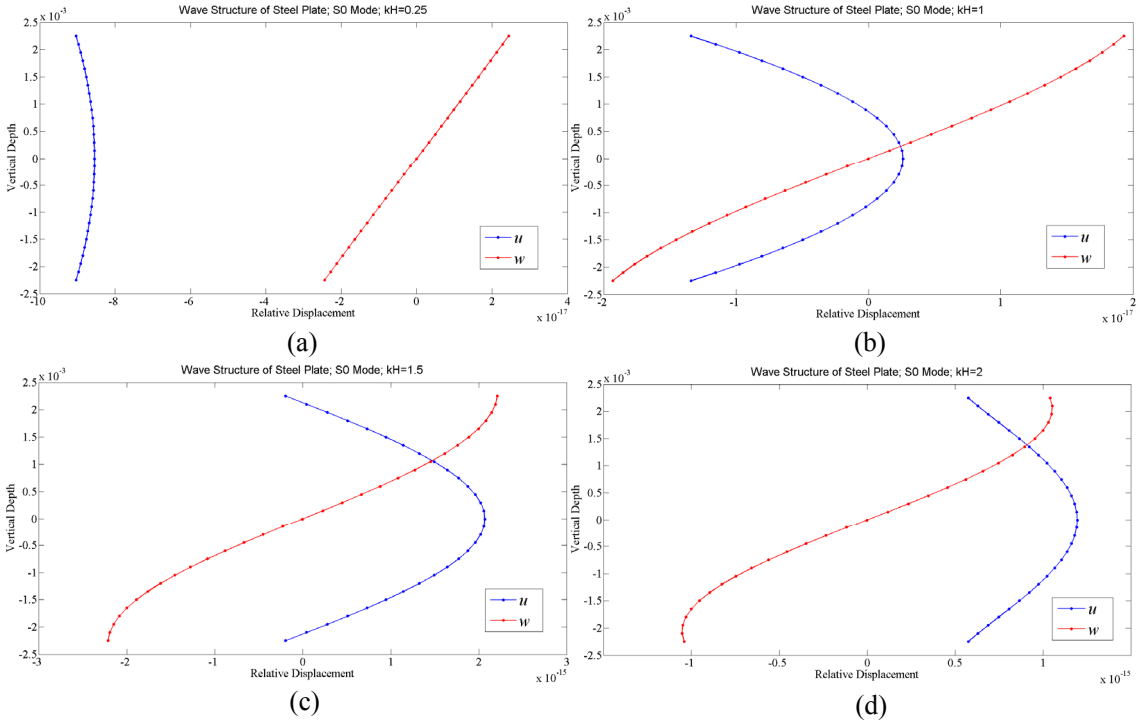

Fig. 3.7 Wave structure of S0 mode of a steel plate, showing u (blue line) and w (red line) displacement profiles across the thickness of the plate.
(a), kH=0.25; (b), kH=1; (c), kH=1.5; (d), kH=2.

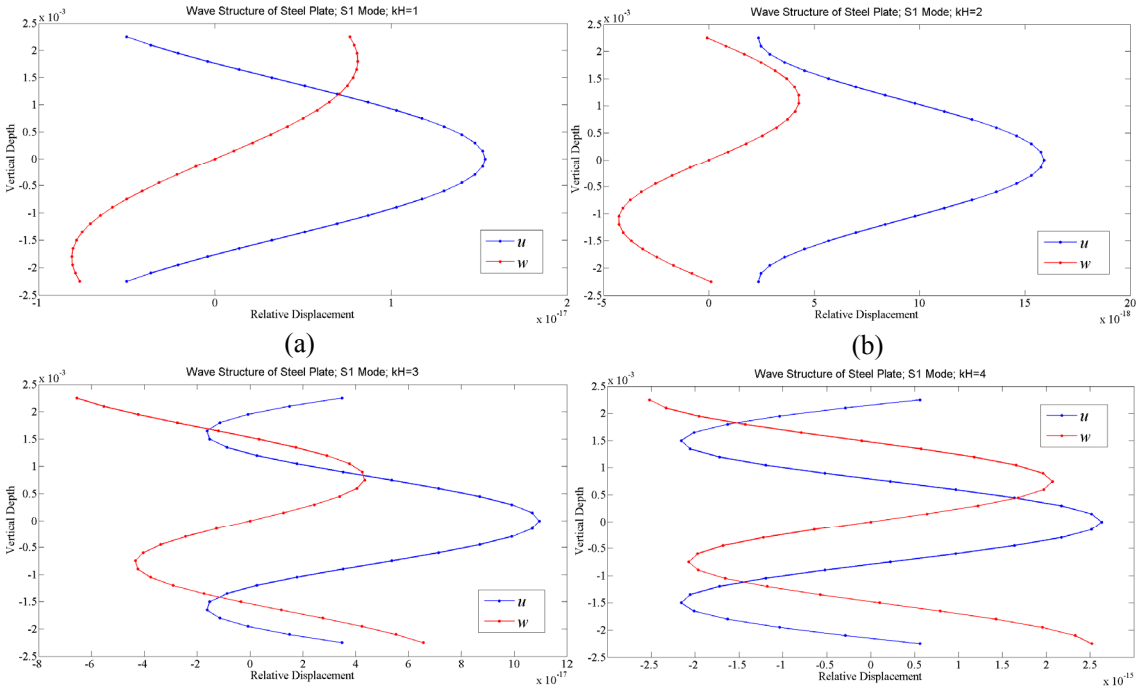

Fig. 3.8 Wave structure of S1 mode of a steel plate, showing u (blue line) and w (red line) displacement profiles across the thickness of the plate.
(a), kH=1; (b), kH=2; (c), kH=3; (d), kH=4.

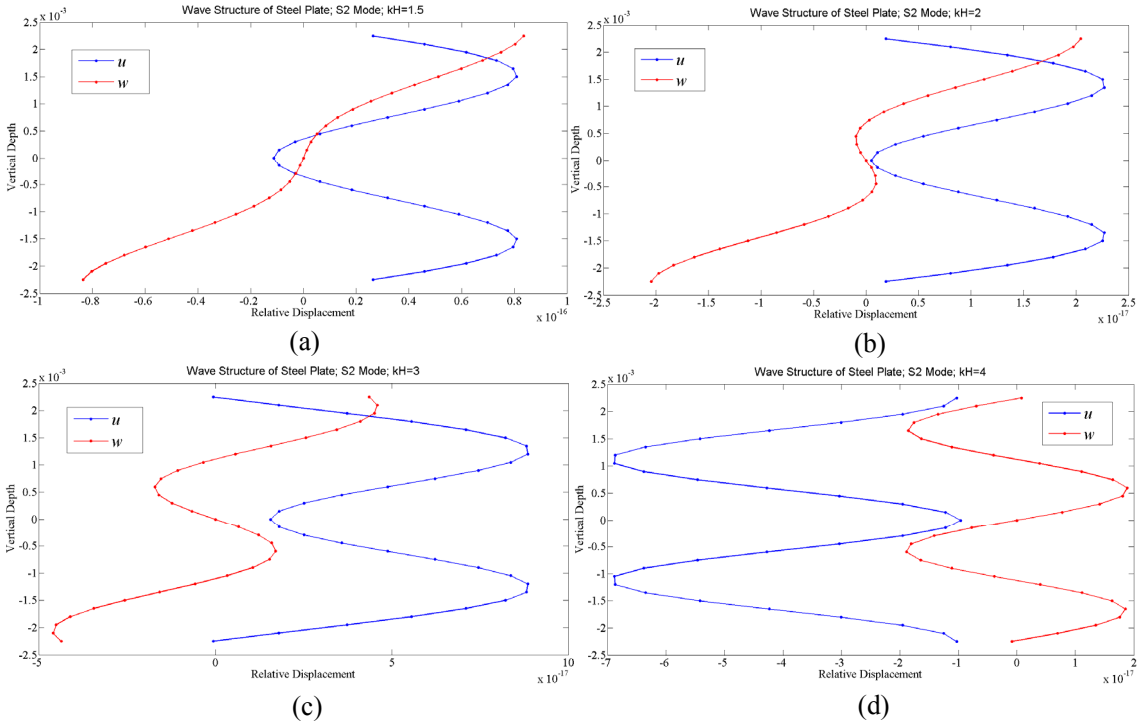

Fig. 3.9 Wave structure of S2 mode of a steel plate, showing showing u (blue line) and w (red line) displacement profiles across the thickness of the plate.
(a), kH=1.5; (b), kH=2; (c), kH=3; (d), kH=4.

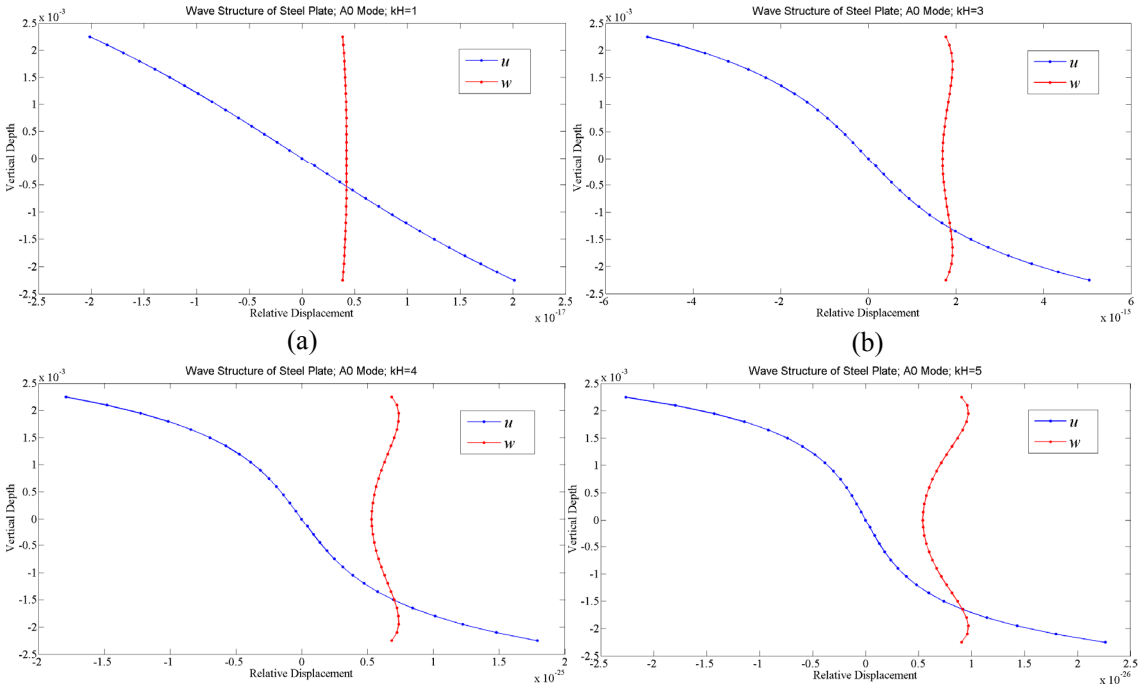

(a) (b)

(c) (d)

Fig. 3.10 Wave structure of A0 mode of a steel plate, showing u (blue line) and w (red line) displacement profiles across the thickness of the plate.

(a), kH=1; (b), kH=3; (c), kH=4; (d), kH=5.

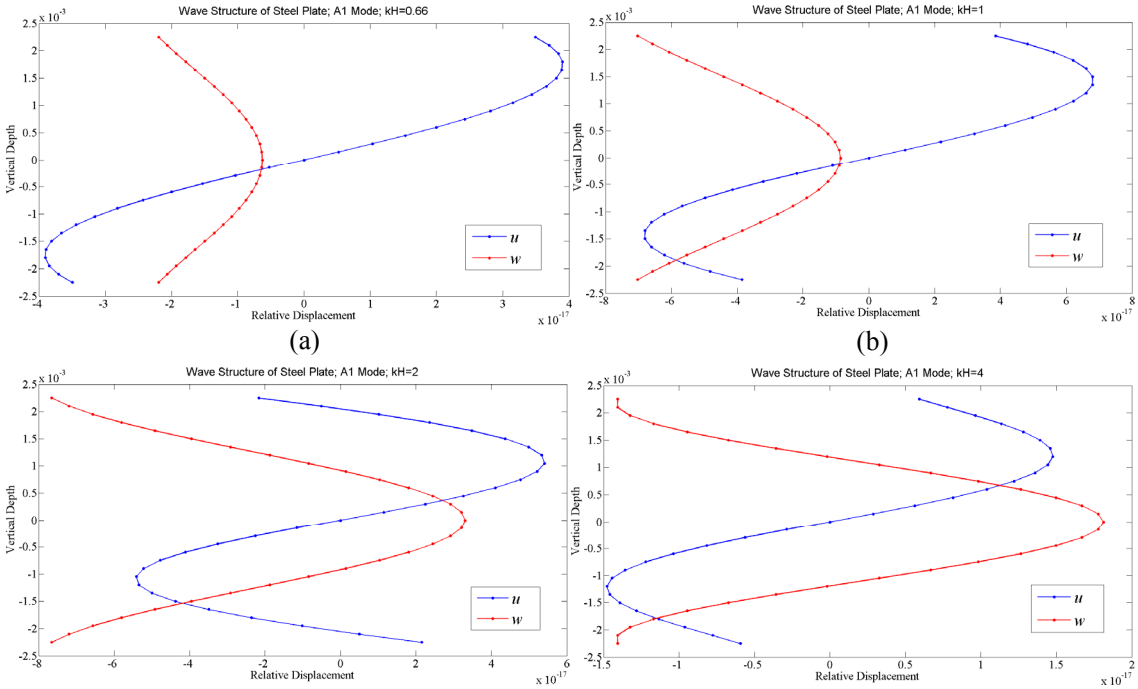

(a) (b)

(c) (d)

Fig. 3.11 Wave structure of A1 mode of a steel plate, showing u (blue line) and w (red line) displacement profiles across the thickness of the plate.

(a), kH=0.66; (b), kH=1; (c), kH=2; (d), kH=4.

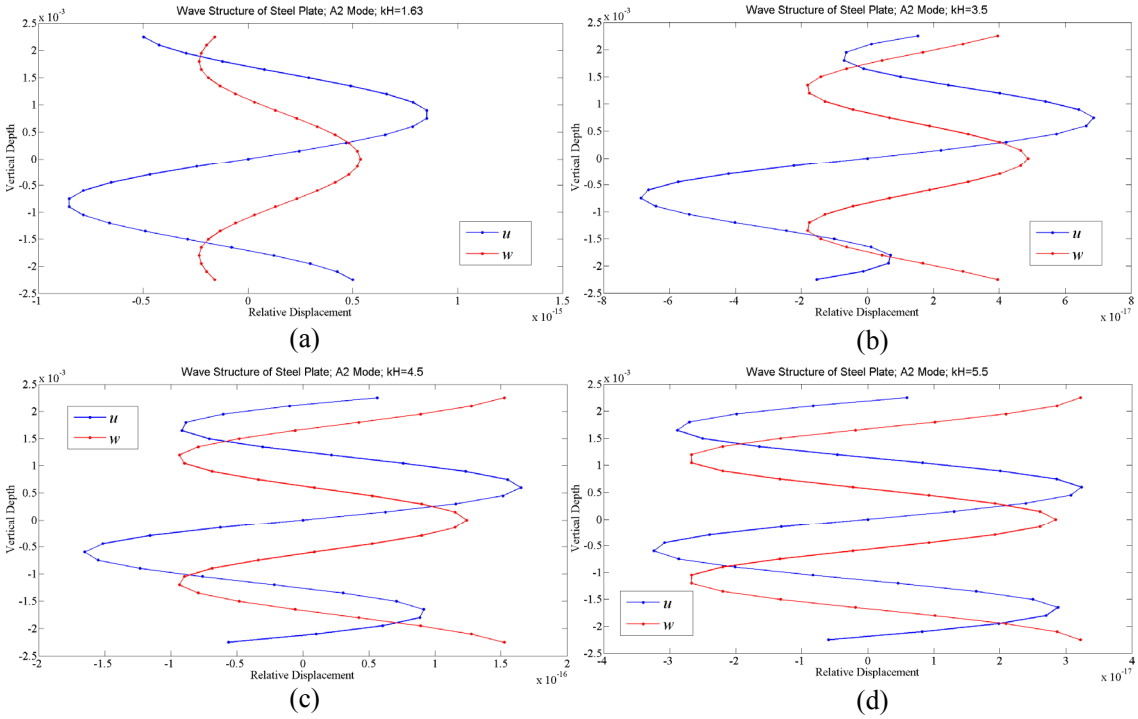

Fig. 3.12 Wave structure of A2 mode of a steel plate, showing u (blue line) and w (red line) displacement profiles across the thickness of the plate.
(a), kH=1.63; (b), kH=3.5; (c), kH=4.5; (d), kH=5.5.

Use of wave structure can lead to increased wave penetration power along a structure. For example, by avoiding energy leakage from water loading or insulation. Improved sensitivity to certain defects can be obtained as a result of controlling impingement at a certain location across the thickness of the structure. The mode selection and wave structure are also used in detection of small defects on the surface of a structure. This is accomplished by getting higher energy concentrations on the outer surface. Also, the wave structure can help us to distinguish crossed modes from each other when we plot dispersion curves of layered media, since usually some parts of different modes of layered media keep close with each other or even with cross point.

3.3 Wave Dispersion in Steel-Epoxy-Concrete Layered Media

From here, we will think about the wave's dispersion in multi-layered media. Since this study attempts to conduct the nondestructive testing on the steel plate strengthened, epoxy adhered RC structures, the steel-epoxy-concrete layered media is certainly the primary object of research. The following deduction is based on the steel-epoxy-concrete 3 layers model that each solid layer bonded with other perfectly. The dispersion curves obtained in this section will be used again in Chapter 4.

3.3.1 Dispersion Equation and Dispersion Curves

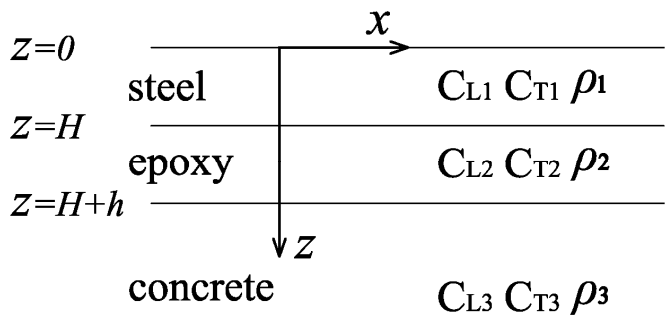

Fig. 3.13 Steel-Epoxy-Concrete 3 layers model: a model of 2 layers overlying on a half space.

For a solid model of two layers of uniform thickness overlying on a half space as shown in Fig. 3.13, as mentioned in Eqs. (3.26)～(3.29), it can be assumed that there are plane waves propagating in the three layers as the forms of:

$$\varphi_1 = Ae^{i(\omega t-kx)-\nu_1 z} + Be^{i(\omega t-kx)+\nu_1 z} \quad \psi_1 = Ce^{i(\omega t-kx)-\nu_1' z} + De^{i(\omega t-kx)+\nu_1' z}$$

$$\varphi_2 = Ee^{i(\omega t-kx)-\nu_2 z} + Fe^{i(\omega t-kx)+\nu_2 z} \quad \psi_2 = Ge^{i(\omega t-kx)-\nu_2' z} + He^{i(\omega t-kx)+\nu_2' z}$$

$$\varphi_3 = Ie^{i(\omega t-kx)-\nu_3 z} \quad \psi_3 = Je^{i(\omega t-kx)-\nu_3' z} \tag{3.34}$$

where φ and ψ are the displacement potentials, the subscript 1, 2 and 3 are referring to layer's number. In layer 1 and 2, there are both incident and reflected waves existing, hence,

each potential contains two components with two unknown amplitude coefficient (A&B; C&D; E&F; G&H); in layer 3, which stands for the half space, only the incident wave is existing, hence, each potential contains one component with one unknown amplitude coefficient (I; J).

Then, for the free surface, the tractions should be free; for the interfaces between two layers, the continuity of tractions and displacements is required. Considering all these boundary conditions, and the expressions in Eqs. (3.7)～(3.10), the following equations can be listed:

$$\sigma_{zx} = \mu_1\left(2\frac{\partial^2\varphi_1}{\partial x\partial z} - \frac{\partial^2\psi_1}{\partial z^2} + \frac{\partial^2\psi_1}{\partial x^2}\right) = 0$$

$$\sigma_{zz} = (\lambda_1 + 2\mu_1)\nabla^2\varphi_1 - 2\mu_1\left(\frac{\partial^2\varphi_1}{\partial x^2} - \frac{\partial^2\psi_1}{\partial x\partial z}\right) = 0 \qquad \text{at } z = 0 \qquad (3.35)$$

and

$$(u_x)_1 = \frac{\partial\varphi_1}{\partial x} - \frac{\partial\psi_1}{\partial z} = (u_x)_2 = \frac{\partial\varphi_2}{\partial x} - \frac{\partial\psi_2}{\partial z}$$

$$(u_z)_1 = \frac{\partial\varphi_1}{\partial z} + \frac{\partial\psi_1}{\partial x} = (u_z)_2 = \frac{\partial\varphi_2}{\partial z} + \frac{\partial\psi_2}{\partial x}$$

$$(\sigma_{zx})_1 = (\sigma_{zx})_2$$

$$(\sigma_{zz})_1 = (\sigma_{zz})_2 \qquad \text{at } z = H \qquad (3.36)$$

and

$$(u_x)_2 = \frac{\partial\varphi_2}{\partial x} - \frac{\partial\psi_2}{\partial z} = (u_x)_3 = \frac{\partial\varphi_3}{\partial x} - \frac{\partial\psi_3}{\partial z}$$

$$(u_z)_2 = \frac{\partial\varphi_2}{\partial z} + \frac{\partial\psi_2}{\partial x} = (u_z)_3 = \frac{\partial\varphi_3}{\partial z} + \frac{\partial\psi_3}{\partial x}$$

$$(\sigma_{zx})_2 = (\sigma_{zx})_3$$

$$(\sigma_{zz})_2 = (\sigma_{zz})_3 \qquad \text{at } z = H + h \qquad (3.37)$$

where H and h are the thickness of 1st and 2nd layer accordingly.

If we substitute the expression of Eq. (3.34) into the boundary conditions Eqs. (3.35)～(3.37), we can obtain 10 equations with 10 variables. To keep those variables having values different from zero, we obtain the dispersion equation as shown in Eq. (3.39) [Shen et al., 2014].

For simplicity, following expressions have been used:

$$k^2 - k_{Li}^2 = \nu_i^2$$

$$k^2 - k_{Ti}^2 = \nu_i'^2 \qquad i = 1,2,3 \qquad (3.38)$$

where k_L and k_T are the wave number of longitudinal wave and transverse wave accordingly.

Table 3.2 Material constants of the Steel-Epoxy-Concrete layered media.

Material	**C_L (m/s)**	**C_T (m/s)**	**ρ (kg/m^3)**	**Thickness (mm)**
Steel	5870	3140	7800	4.5
Epoxy	2500	1112	1120	5
Concrete	4000	2450	2400	∞

By solving the dispersion equation Eq. (3.39) with the bisection method based algorithm mentioned in Section 3.2.2, the dispersion curves, which indicate the relation between wave number or frequency versus phase velocity, can be plotted as shown in Fig. 3.14. The material constants used in Fig. 3.14 are shown in Table 3.2.

From Fig. 3.14, we can see that infinite modes exist in the Steel-Epoxy-Concrete layered media. The 1st mode starts from the Rayleigh wave speed of half-space (3rd layer) c_{R3}, and other modes start from transverse wave speed of half-space (3rd layer) c_{T3} with cutoff frequencies. All the modes asymptotically trend to the transverse wave speed of 2nd layer c_{T2} as frequency tends towards infinity. The 1st mode performs a hook-like curve in low frequency

range, where the minimum point of the "hook" is determined by the 2nd layer's transverse wave speed c_{T2} also. This dispersion curves of the Steel-Epoxy-Concrete layered media will be used in Chapter 4 for epoxy's material properties estimation, more discussion about the properties of this dispersion curves will be continued in Section 4.2.

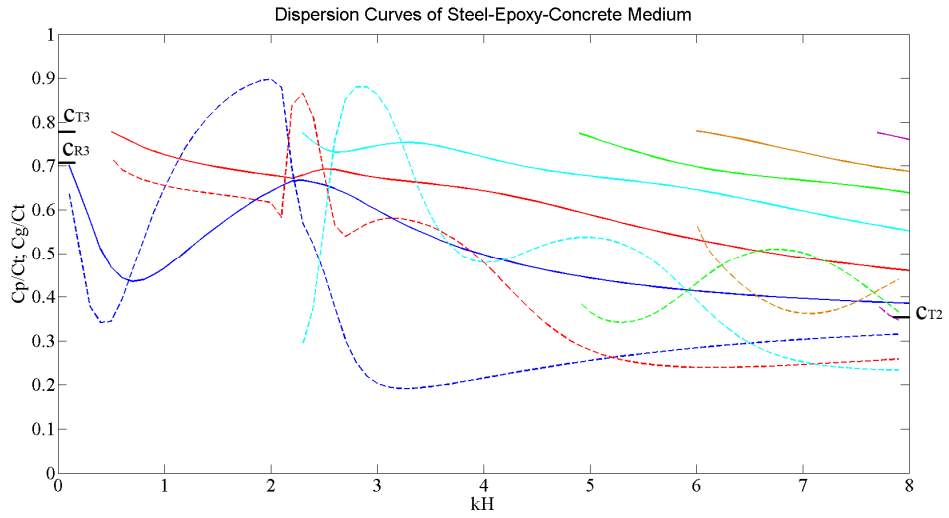

Fig. 3.14 Dispersion curves of a Steel-Epoxy-Concrete media:
solid line, phase velocity; dashed line, group velocity.

$$\Delta = \begin{vmatrix}
\left(2k^2-k_{T1}^2\right)e^{\nu_1 H} & 2k\nu_1' e^{\nu_1' H} & \left(2k^2-k_{T1}^2\right)e^{-\nu_1 H} & -2k\nu_1' e^{-\nu_1' H} & 0 & 0 & 0 & 0 & 0 & 0 \\
2k\nu_1 e^{\nu_1 H} & \left(2k^2-k_{T1}^2\right)e^{\nu_1' H} & -2k\nu_1 e^{-\nu_1 H} & \left(2k^2-k_{T1}^2\right)e^{-\nu_1' H} & 0 & 0 & 0 & 0 & 0 & 0 \\
-k & -\nu_1' & -k & \nu_1' & k & \nu_2' & k & -\nu_2' & 0 & 0 \\
-\nu_1 & -k & \nu_1 & -k & \nu_2 & k & -\nu_2 & k & 0 & 0 \\
2k\nu_1 & 2k^2-k_{T1}^2 & -2k\nu_1 & 2k^2-k_{T1}^2 & -2k\nu_2\dfrac{\mu_2}{\mu_1} & -\dfrac{\mu_2}{\mu_1}\left(2k^2-k_{T2}^2\right) & 2k\nu_2\dfrac{\mu_2}{\mu_1} & -\dfrac{\mu_2}{\mu_1}\left(2k^2-k_{T2}^2\right) & 0 & 0 \\
2k^2-k_{T1}^2 & 2k\nu_1' & 2k^2-k_{T1}^2 & -2k\nu_1' & -\dfrac{\mu_2}{\mu_1}\left(2k^2-k_{T2}^2\right) & -2k\nu_2'\dfrac{\mu_2}{\mu_1} & -\dfrac{\mu_2}{\mu_1}\left(2k^2-k_{T2}^2\right) & 2k\nu_2'\dfrac{\mu_2}{\mu_1} & 0 & 0 \\
0 & 0 & 0 & 0 & -ke^{-\nu_2 h} & -\nu_2' e^{-\nu_2' h} & -ke^{\nu_2 h} & \nu_2' e^{\nu_2' h} & ke^{-\nu_3 h} & \nu_3' e^{-\nu_3' h} \\
0 & 0 & 0 & 0 & -\nu_2 e^{-\nu_2 h} & -ke^{-\nu_2' h} & \nu_2 e^{\nu_2 h} & -ke^{\nu_2' h} & \nu_3 e^{-\nu_3 h} & ke^{-\nu_3' h} \\
0 & 0 & 0 & 0 & 2k\nu_2 e^{-\nu_2 h} & \left(2k^2-k_{T2}^2\right)e^{-\nu_2' h} & -2k\nu_2 e^{\nu_2 h} & \left(2k^2-k_{T2}^2\right)e^{\nu_2' h} & -2k\nu_3\dfrac{\mu_3}{\mu_2}e^{-\nu_3 h} & -\dfrac{\mu_3}{\mu_2}\left(2k^2-k_{T3}^2\right)e^{-\nu_3' h} \\
0 & 0 & 0 & 0 & \left(2k^2-k_{T2}^2\right)e^{-\nu_2 h} & 2k\nu_2' e^{-\nu_2' h} & \left(2k^2-k_{T2}^2\right)e^{\nu_2 h} & -2k\nu_2' e^{\nu_2' h} & -\dfrac{\mu_3}{\mu_2}\left(2k^2-k_{T3}^2\right)e^{-\nu_3 h} & -2k\nu_3'\dfrac{\mu_3}{\mu_2}e^{-\nu_3' h}
\end{vmatrix} = 0 \quad (3.39)$$

3.3.2 Wave Structure Analysis

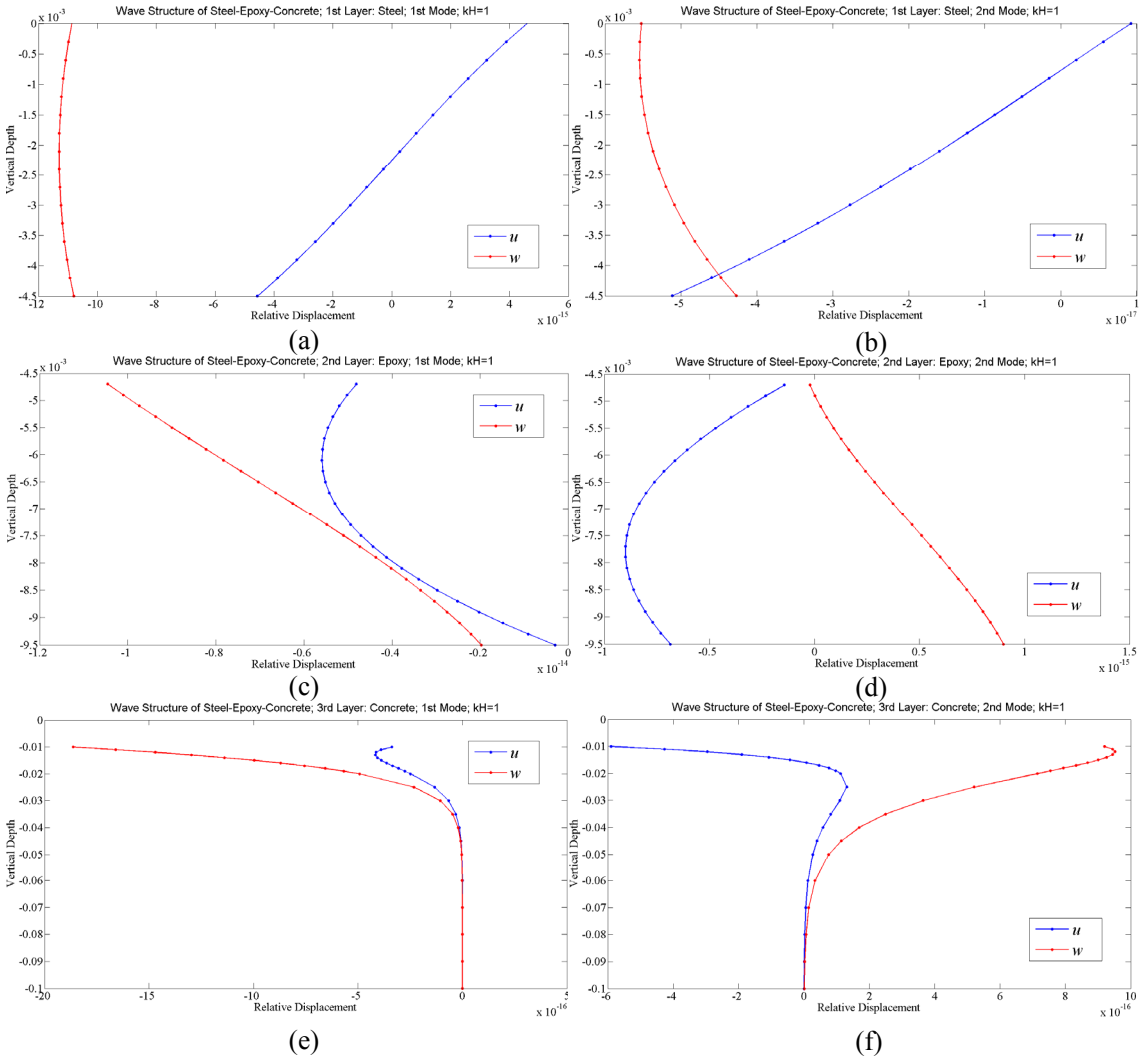

Fig. 3.15 Wave structures of 1st and 2nd modes of a Steel-Epoxy-Concrete layered media, when kH=1, showing u (blue line) and w (red line) displacement profiles in layers of steel (a,b), epoxy (c,d), and concrete (e,f) respectively.

In Fig. 3.15～Fig. 3.17, the wave structures of first three modes of a Steel-Epoxy-Concrete three layered media have been plotted. Since the amplitudes of displacements in different layers are quite different due to different material constants, the wave structures are shown separately with layers. Fig. 3.15 shows the wave structures when $kH = 1$, where only 1st and 2nd wave modes exist as can be seen in Fig. 3.14. Fig. 3.16 and 3.17 show the wave structures when kH are 3 and 5, relatively high values, where the 3rd mode also exists. From those figures, we can

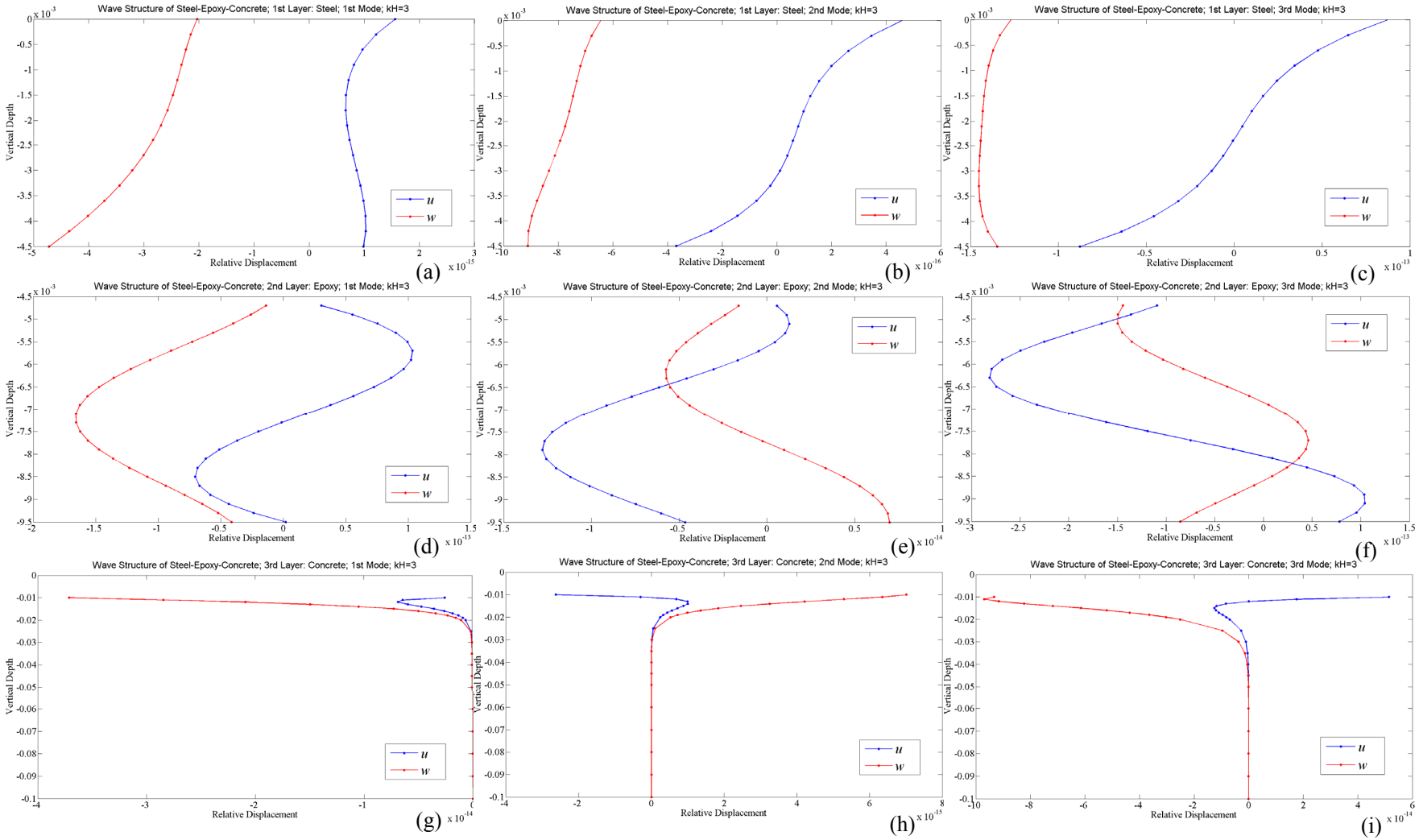

Fig. 3.16 Wave structures of 1st, 2nd, and 3rd modes of a Steel-Epoxy-Concrete layered media, when kH=3, showing u (blue line) and w (red line) displacement profiles in layers of steel (a,b,c), epoxy (d,e,f), and concrete (g,h,i) respectively.

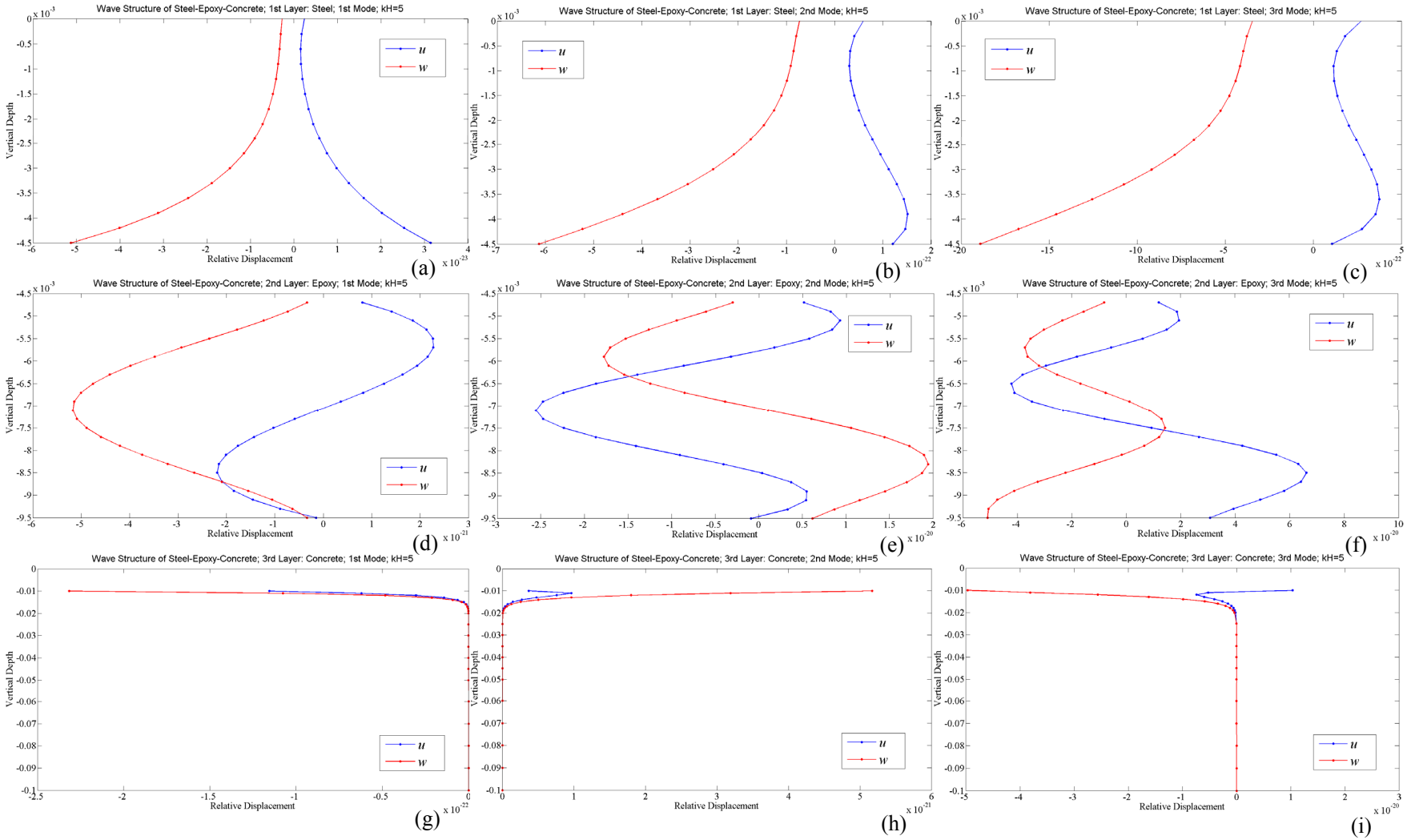

Fig. 3.17 Wave structures of 1st, 2nd, and 3rd modes of a Steel-Epoxy-Concrete layered media, when kH=5, showing u (blue line) and w (red line) displacement profiles in layers of steel (a,b,c), epoxy (d,e,f), and concrete (g,h,i) respectively.

see that the differences between the 1st mode and the 2nd mode are quite notable both in 1st layer (steel) and 2nd layer (epoxy), and when $kH = 5$, in epoxy layer, the 2nd mode is much curving than the 1st mode, as shown in Fig. 3.17 (d)&(e). The differences between the 2nd mode and the 3rd mode are generally concentrated in the 2nd (epoxy) layer. In the 1st (steel) layer, the wave structures of these two modes are quite alike with each other. From the dispersion curves in Fig. 3.14, we can find a very sensitive area when $kH = 2.2$, where the 1st mode and the 2nd mode are so close with each other, easily to make confusion. After this area, these two modes develop with different trends. Through the wave structure analysis, we can clearly see that when $kH = 5$, the 2nd mode's structure is more curving than the 1st mode's, which logically should be. In other words, the plotting of dispersion curves of the 1st mode and the 2nd mode in Fig. 3.14 is correct. With the results of wave structures, we can easily distinguish different modes in the areas with modes adjacency or modes crossing, eliminating the confusions.

3.4 Wave Dispersion in Steel-Water-Concrete Layered Media

Here we will include a liquid layer between solid layers to see how the dispersion curves will behave due to the additional liquid layer. Again, a model of steel-water-concrete layered media becomes our object of research.

3.4.1 Dispersion Equation

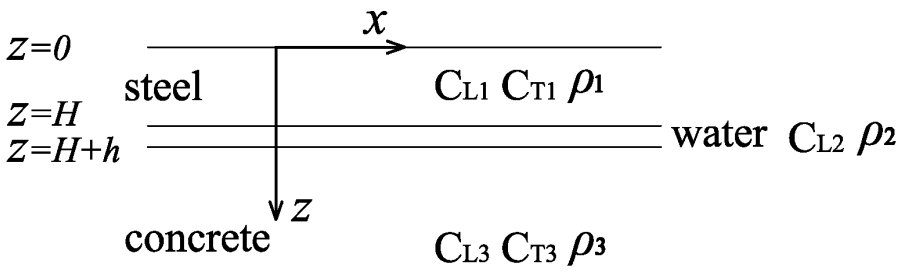

Fig. 3.18 Steel-Water-Concrete layered model: a model of 2 layers overlying on a half space.

As shown in Fig. 3.18, for a Steel-Water-Concrete layered model which contains a liquid layer between two solid layers, as mentioned in Eqs. (3.26)～(3.30), it can be assumed that there are plane waves propagating in the three layers as the forms of:

$$\varphi_1 = Ae^{i(\omega t-kx)-\nu_1 z} + Be^{i(\omega t-kx)+\nu_1 z} \quad \psi_1 = Ce^{i(\omega t-kx)-\nu_1' z} + De^{i(\omega t-kx)+\nu_1' z}$$

$$\varphi_2 = Ee^{i(\omega t-kx)-\nu_2 z} + Fe^{i(\omega t-kx)+\nu_2 z}$$

$$\varphi_3 = Ge^{i(\omega t-kx)-\nu_3 z} \qquad \psi_3 = He^{i(\omega t-kx)-\nu_3' z} \tag{3.40}$$

Then, for the free surface, the tractions should be free; for the interfaces between solid layer and liquid layer, the continuity of tractions and displacements on the normal direction is required, and the tractions of solid sides on the shear direction should be vanished. Considering all these boundary conditions, and the expressions in Eqs. (3.7)～(3.10), the following equations can be listed:

$$\sigma_{zx} = \mu_1\left(2\frac{\partial^2\varphi_1}{\partial x\partial z} - \frac{\partial^2\psi_1}{\partial z^2} + \frac{\partial^2\psi_1}{\partial x^2}\right) = 0$$

$$\sigma_{zz} = (\lambda_1 + 2\mu_1)\nabla^2\varphi_1 - 2\mu_1\left(\frac{\partial^2\varphi_1}{\partial x^2} - \frac{\partial^2\psi_1}{\partial x\partial z}\right) = 0 \qquad at\ z = 0 \tag{3.41}$$

and

$$(u_z)_1 = \frac{\partial\varphi_1}{\partial z} + \frac{\partial\psi_1}{\partial x} = (u_z)_2 = \frac{\partial\varphi_2}{\partial z} + \frac{\partial\psi_2}{\partial x}$$

$$(\sigma_{zx})_1 = \mu_1\left(2\frac{\partial^2\varphi_1}{\partial x\partial z} - \frac{\partial^2\psi_1}{\partial z^2} + \frac{\partial^2\psi_1}{\partial x^2}\right) = 0$$

$$(\sigma_{zz})_1 = (\lambda_1 + 2\mu_1)\nabla^2\varphi_1 - 2\mu_1\left(\frac{\partial^2\varphi_1}{\partial x^2} - \frac{\partial^2\psi_1}{\partial x\partial z}\right) = (\sigma_{zz})_2 = \lambda_2\nabla^2\varphi_2$$

$$at\ z = H \tag{3.42}$$

and

$$(u_z)_2 = \frac{\partial \varphi_2}{\partial z} + \frac{\partial \psi_2}{\partial x} = (u_z)_3 = \frac{\partial \varphi_3}{\partial z} + \frac{\partial \psi_3}{\partial x}$$

$$(\sigma_{zx})_3 = \mu_3 \left(2\frac{\partial^2 \varphi_3}{\partial x \partial z} - \frac{\partial^2 \psi_3}{\partial z^2} + \frac{\partial^2 \psi_3}{\partial x^2} \right) = 0$$

$$(\sigma_{zz})_2 = \lambda_2 \nabla^2 \varphi_2 = (\sigma_{zz})_3 = (\lambda_3 + 2\mu_3)\nabla^2 \varphi_3 - 2\mu_3 \left(\frac{\partial^2 \varphi_3}{\partial x^2} - \frac{\partial^2 \psi_3}{\partial x \partial z} \right)$$

$$at \;\; z = H + h \quad (3.43)$$

where H and h are the thickness of 1st and 2nd layer accordingly.

If we substitute the expression of Eq. (3.40) into the boundary conditions Eqs. (3.41)～(3.43), we can obtain 8 equations with 8 variables. To keep those variables having values different from zero, we obtain the dispersion equation as shown in Eq. (3.44).

3.4.2 Dispersion Curves

Fig. 3.19 shows the dispersion curves of the Steel-Water-Concrete layered media, with 3 different thicknesses of the water layer, in order to find out the effect of water layer thickness to the shape of curves. The material constants used in Fig. 3.19 are shown in Table 3.3.

Table 3.3 Material constants of the Steel-Water-Concrete layered media.

Material	**C_L (m/s)**	**C_T (m/s)**	**ρ (kg/m^3)**	**Thickness (mm)**	
Steel	5870	3140	7800	H	
Water	1500	/	1000	Model 1	*h=0.02H*
				Model 2	*h=0.05H*
				Model 3	*h=0.10H*
Concrete	4000	2450	2400	∞	

When two solid layers (steel and concrete) are inserted by a thin liquid layer (water), only two wave modes are found in the area where phase velocity is smaller than transverse velocity in the steel plate (c_{T1}). The 1st mode, which starts from zero value when $kH = 0$, is born with the liquid layer beneath a solid layer. This wave is actually only propagating on the interface of solid and liquid, called Scholte wave. It is a significant difference on dispersion curves between the media with liquid layer and that without liquid layer. We will further introduce this wave mode in Section 3.7. In Fig 3.19, we can clearly see that this Scholte wave mode (the 1st mode) is strongly affected by the water layer thickness. When the thickness is relatively thin, the growth of the wave velocity is slow. However, its limit value when kH increases is always approximately the transverse velocity in the liquid layer, very close, but not reach that value. On the other hand, the 2nd wave mode is less sensitive to the thickness of water layer, and the shape is very similar with the 1st wave mode of Steel-Epoxy-Concrete layered media case, which are both the "hook-like" shape.

$$\Delta = \begin{vmatrix} \left(2k^2-k_{\beta 1}^2\right)e^{\nu_1 H} & \left(2k^2-k_{\beta 1}^2\right)e^{-\nu_1 H} & 2k\nu_1' e^{\nu_1' H} & -2k\nu_1' e^{-\nu_1' H} & 0 & 0 & 0 & 0 \\ 2k\nu_1 e^{\nu_1 H} & -2k\nu_1 e^{-\nu_1 H} & \left(2k^2-k_{\beta 1}^2\right)e^{\nu_1' H} & \left(2k^2-k_{\beta 1}^2\right)e^{-\nu_1' H} & 0 & 0 & 0 & 0 \\ -\nu_1 & \nu_1 & -k & -k & \nu_2 & -\nu_2 & 0 & 0 \\ -2k\nu_1 & 2k\nu_1 & -\left(2k^2-k_{\beta 1}^2\right) & -\left(2k^2-k_{\beta 1}^2\right) & 0 & 0 & 0 & 0 \\ \left(2k^2-k_{\beta 1}^2\right) & \left(2k^2-k_{\beta 1}^2\right) & 2k\nu_1' & -2k\nu_1' & \frac{\lambda_2}{\mu_1}k_{\alpha 2}^2 & \frac{\lambda_2}{\mu_1}k_{\alpha 2}^2 & 0 & 0 \\ 0 & 0 & 0 & 0 & -\nu_2 e^{-\nu_2 d} & \nu_2 e^{\nu_2 d} & \nu_3 e^{-\nu_3 d} & k e^{-\nu_3' d} \\ 0 & 0 & 0 & 0 & 0 & 0 & -2k\nu_3 e^{-\nu_3 d} & -\left(2k^2-k_{\beta 3}^2\right)e^{-\nu_3' d} \\ 0 & 0 & 0 & 0 & -\frac{\lambda_2}{\mu_3}k_{\alpha 2}^2 e^{-\nu_2 d} & -\frac{\lambda_2}{\mu_3}k_{\alpha 2}^2 e^{\nu_2 d} & -\left(2k^2-k_{\beta 3}^2\right)e^{-\nu_3 d} & -2k\nu_3' e^{-\nu_3' d} \end{vmatrix} = 0 \quad (3.44)$$

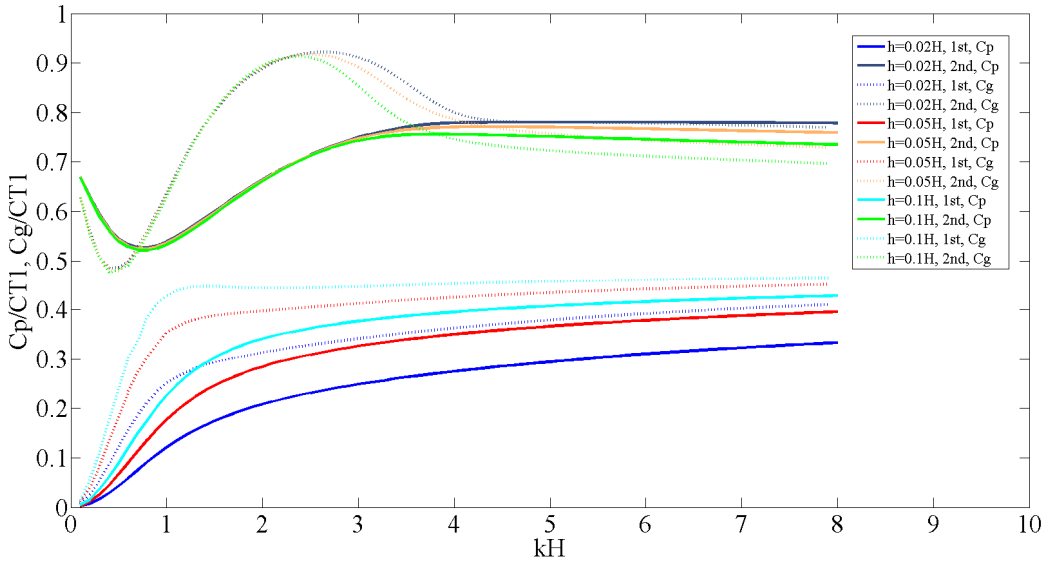

Fig. 3.19 Dispersion curves of a Steel-Water-Concrete media:
solid line, phase velocity; dashed line, group velocity.

3.5 Wave Dispersion in Steel-Spring-Concrete Layered Media

In the previous section, we obtained the dispersion curves of a steel-water-concrete layered media, and discover the existence of Scholte wave on the solid-liquid interface. The liquid layer can deliver normal stress on z direction, but is not able to deliver shear stress on x direction if it is non-viscous. Therefore, the effect of a water layer between two solid layers is very close to the function of spring element which has only vertical stiffness. To verify this, we design a model of steel-spring-concrete layered media with spring's constant of s, and compare its dispersion curves with that of steel-water-concrete layered media. If they are identical with each other, then the simplified spring model can substitute the liquid layer contained model in the numerical simulations (FEM, BEM) of this type of problems, which can significantly simplify the meshing and decrease the size of the problems. If they are somehow different, then the explanation can also be given through the comparison of their dispersion curves.

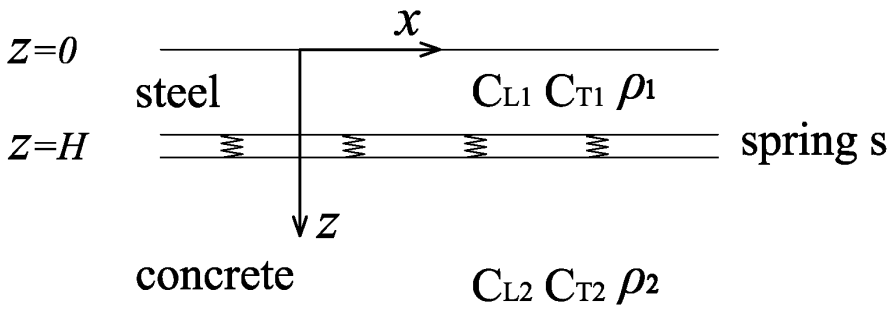

Fig. 3.20 Steel-Spring-Concrete layered model.

As shown in Fig. 3.20, for a Steel-Spring-Concrete layered model which contains two solid layers connected by universally distributed springs, as mentioned in Eqs. (3.26)～(3.29), it can be assumed that there are plane waves propagating in the two solid layers as the forms of:

$$\varphi_1 = Ae^{i(\omega t-kx)-\nu_1 z} + Be^{i(\omega t-kx)+\nu_1 z} \qquad \psi_1 = Ce^{i(\omega t-kx)-\nu_1' z} + De^{i(\omega t-kx)+\nu_1' z}$$

$$\varphi_2 = Ee^{i(\omega t-kx)-\nu_2 z} \qquad \psi_2 = Fe^{i(\omega t-kx)-\nu_2' z} \tag{3.45}$$

Then, for the free surface, the tractions should be free; for the spring connection on the interface between two solid layers, the continuity of normal traction is required, and the normal traction should be equal to the product of the spring constant $s\ (N/m^3)$ and the displacement difference of the two layers. Considering all these boundary conditions, and the expressions in Eqs. (3.7)～(3.10), the following equations can be listed:

$$\sigma_{zx} = \mu_1 \left(2\frac{\partial^2 \varphi_1}{\partial x \partial z} - \frac{\partial^2 \psi_1}{\partial z^2} + \frac{\partial^2 \psi_1}{\partial x^2} \right) = 0$$

$$\sigma_{zz} = (\lambda_1 + 2\mu_1)\nabla^2 \varphi_1 - 2\mu_1 \left(\frac{\partial^2 \varphi_1}{\partial x^2} - \frac{\partial^2 \psi_1}{\partial x \partial z} \right) = 0 \qquad at\ z = 0 \qquad (3.46)$$

and,

$$(\sigma_{zx})_1 = 0 \quad ; \quad (\sigma_{zx})_2 = 0$$

$$s \cdot [(u_z)_2 - (u_z)_1] = (\sigma_{zz})_1 = (\sigma_{zz})_2 \qquad at\ z = H \qquad (3.47)$$

where H is the thickness 1st layer, and s is the spring constant, whose dimension is N/m^3.

If we substitute the expression of Eq. (3.45) into the boundary conditions Eqs. (3.46)～(3.47), we can obtain 6 equations with 6 variables. To keep those variables having values different from zero, we obtain the dispersion equation as shown in Eq. (3.48).

$$\Delta = \begin{vmatrix} \left(2k^2 - k_{\beta 1}^2\right) e^{\nu_1 H} & \left(2k^2 - k_{\beta 1}^2\right) e^{-\nu_1 H} & 2k\nu_1' e^{\nu_1' H} & -2k\nu_1' e^{-\nu_1' H} & 0 & 0 \\ 2k\nu_1 e^{\nu_1 H} & -2k\nu_1 e^{-\nu_1 H} & \left(2k^2 - k_{\beta 1}^2\right) e^{\nu_1' H} & \left(2k^2 - k_{\beta 1}^2\right) e^{-\nu_1' H} & 0 & 0 \\ \frac{s\nu_1}{\mu_1} - \left(2k^2 - k_{\beta 1}^2\right) & \frac{-s\nu_1}{\mu_1} - \left(2k^2 - k_{\beta 1}^2\right) & \frac{sk}{\mu_1} - 2k\nu_1' & \frac{sk}{\mu_1} + 2k\nu_1' & -\frac{s\nu_2}{\mu_1} & -\frac{sk}{\mu_1} \\ \left(2k^2 - k_{\beta 1}^2\right) & \left(2k^2 - k_{\beta 1}^2\right) & 2k\nu_1' & -2k\nu_1' & -\frac{\mu_2}{\mu_1}\left(2k^2 - k_{\beta 2}^2\right) & -\frac{\mu_2}{\mu_1} \cdot 2k\nu_2' \\ -2k\nu_1 & 2k\nu_1 & -\left(2k^2 - k_{\beta 1}^2\right) & -\left(2k^2 - k_{\beta 1}^2\right) & 0 & 0 \\ 0 & 0 & 0 & 0 & 2k\nu_2 & \left(2k^2 - k_{\beta 2}^2\right) \end{vmatrix} = 0$$

(3.48)

The spring components applied in this model are be attempted to substitute the effect of water layer, since they have similar mechanism of normal traction transmit and shear traction isolation. However, how large the spring constant should be in this model is a question for us. Hence, we tried numbers of different values of the spring constant to find the most appropriate one. In Fig. 3.21, various shapes of the dispersion curve of the 1st mode are shown with 8 different values of spring constant. To emphasize the most sensitive part, only the range of $0 < kH < 2$ is shown. As you can see, when the value of spring constant increases from $1.0e5\ N/m^3$ to $1.0e12\ N/m^3$, the curves change the shape from a nearly linear one to a "hook-like" one. When the spring constant is small, the curve behaves like the A0 mode of the "steel plate in vacuum" model (blue curve in Fig. 3.21), which makes sense because when the spring is weak, this model will approximately become a steel plate floating in the vacuum, lacking the interaction with the bottom solid layer. On the other hand, when the spring constant is big enough, the curve behaves like the perfectly bonded case, which means the spring is so strong to become rigid tight between the two solid layers.

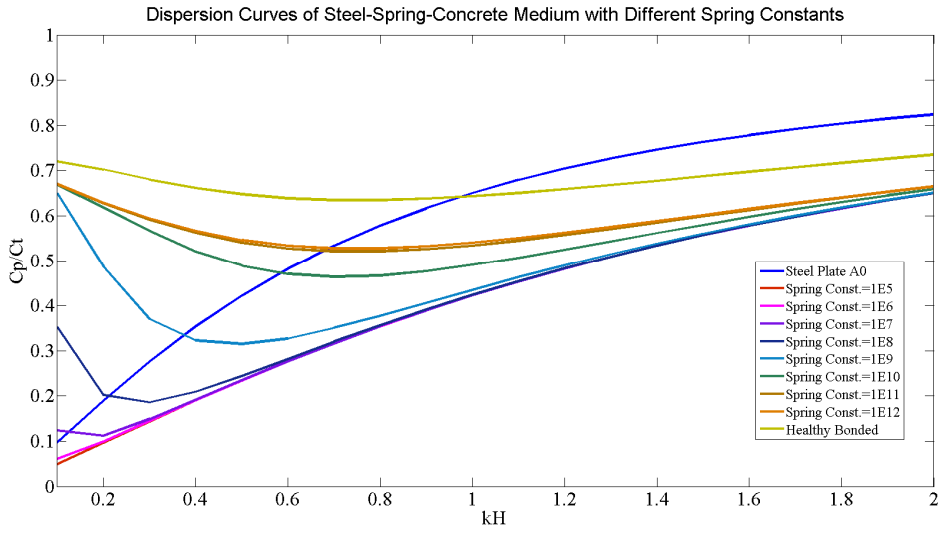

Fig. 3.21 Dispersion curves of Steel-Spring-Concrete media with different spring constant.

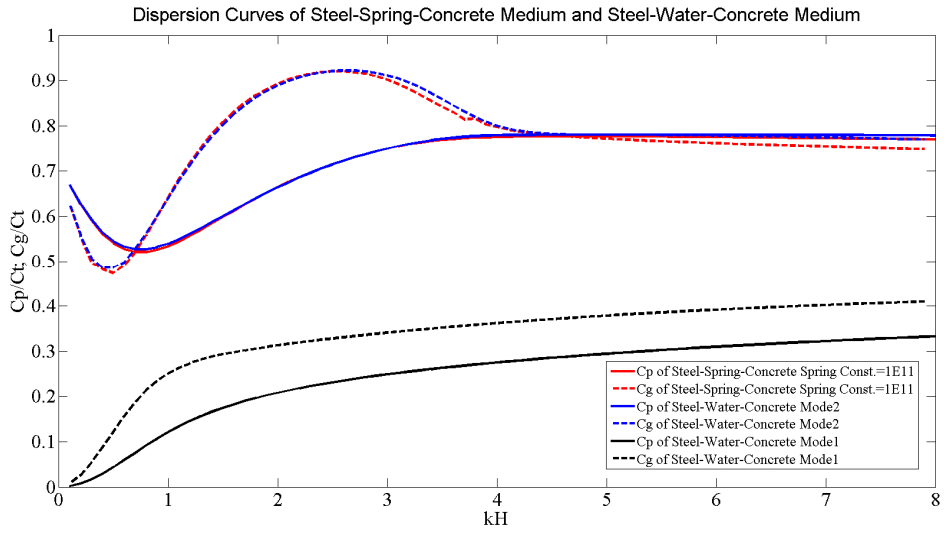

Fig. 3.22 Comparison of dispersion curves of Steel-Spring-Concrete model and Steel-Water-Concrete model: solid line, phase velocity; dashed line, group velocity.

In Fig. 3.22, both the dispersion curves of the Steel-Spring-Concrete media and the Steel-Water-Concrete media have been put in for comparison, in which the thickness of water layer is $0.02H$ (H is the thickness of steel plate here), and the spring constant s is $1.0e11\ N/m^3$. In the spring model, only one wave mode shows, which is plotted by red curves; on the other hand, in the water layer model, two modes exist, and one of them is the Scholte wave, plotted by black curves. However, the phase velocity of the 1st wave mode of the spring model is almost identical with that of the 2nd mode of the water layer model, which indicates that spring can partly substitute the effect of water layer on dispersion property. The 1st wave mode of the water layer model, i.e. the Scholte wave, only exist on the solid-liquid interface. Therefore, through the spring model we cannot obtain it, and that is the major difference between these two models. However, if the wave propagation on the solid-liquid interface is not concerned in some problems, but only the delivery of stress is focused on, then the spring model can successfully substitute the liquid layer contained model in the numerical simulations. From this comparison we can also find that the spring constant of $1.0e11\ N/m^3$ level is almost equal to the water layer of $0.02H$ thickness on elastic property.

3.6 Wave Dispersion in Steel-Water-Epoxy-Concrete Layered Media

To compare the case of steel-epoxy-concrete multi-layered media in Section 3.3, we will add a water layer between the steel plate and the epoxy, to see what difference will be caused on the behavior of the dispersion curves. The results of this section will also be used in Chapter 6 to detect the existence of water layer beneath the steel plate.

3.6.1 Dispersion Equation and Dispersion Curves

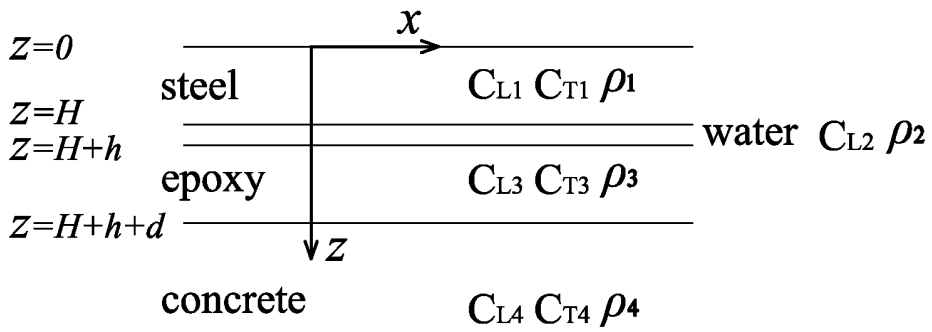

Fig. 3.23 Steel-Water-Epoxy-Concrete layered model.

As shown in Fig. 3.23, for a Steel-Water-Epoxy-Concrete layered model which contains a liquid layer, as mentioned in Eqs. (3.26)～(3.30), it can be assumed that there are plane waves propagating in the three layers as the forms of:

$$\varphi_1 = Ae^{i(\omega t-kx)-\nu_1 z} + Be^{i(\omega t-kx)+\nu_1 z} \quad \psi_1 = Ce^{i(\omega t-kx)-\nu_1' z} + De^{i(\omega t-kx)+\nu_1' z}$$

$$\varphi_2 = Ee^{i(\omega t-kx)-\nu_2 z} + Fe^{i(\omega t-kx)+\nu_2 z}$$

$$\varphi_3 = Ge^{i(\omega t-kx)-\nu_3 z} + He^{i(\omega t-kx)+\nu_3 z} \quad \psi_3 = Ie^{i(\omega t-kx)-\nu_3' z} + Je^{i(\omega t-kx)+\nu_3' z}$$

$$\varphi_4 = Ke^{i(\omega t-kx)-\nu_4 z} \quad \psi_4 = Le^{i(\omega t-kx)-\nu_4' z} \tag{3.45}$$

Then, for the free surface, the tractions should be free; for the interfaces between solid layer and liquid layer, the continuity of tractions and displacements on the normal direction is required, and the tractions of solid sides on the shear direction should be vanished; for the interfaces between two solid layers, the continuity of tractions and displacements is required.

Considering all these boundary conditions, and the expressions in Eqs. (3.7)～(3.10), the following equations can be listed:

$$\sigma_{zx} = \mu_1 \left(2\frac{\partial^2 \varphi_1}{\partial x \partial z} - \frac{\partial^2 \psi_1}{\partial z^2} + \frac{\partial^2 \psi_1}{\partial x^2} \right) = 0$$

$$\sigma_{zz} = (\lambda_1 + 2\mu_1)\nabla^2 \varphi_1 - 2\mu_1 \left(\frac{\partial^2 \varphi_1}{\partial x^2} - \frac{\partial^2 \psi_1}{\partial x \partial z} \right) = 0 \qquad \text{at } z = 0 \qquad (3.46)$$

and

$$(u_z)_1 = \frac{\partial \varphi_1}{\partial z} + \frac{\partial \psi_1}{\partial x} = (u_z)_2 = \frac{\partial \varphi_2}{\partial z} + \frac{\partial \psi_2}{\partial x}$$

$$(\sigma_{zx})_1 = \mu_1 \left(2\frac{\partial^2 \varphi_1}{\partial x \partial z} - \frac{\partial^2 \psi_1}{\partial z^2} + \frac{\partial^2 \psi_1}{\partial x^2} \right) = 0$$

$$(\sigma_{zz})_1 = (\lambda_1 + 2\mu_1)\nabla^2 \varphi_1 - 2\mu_1 \left(\frac{\partial^2 \varphi_1}{\partial x^2} - \frac{\partial^2 \psi_1}{\partial x \partial z} \right) = (\sigma_{zz})_2 = \lambda_2 \nabla^2 \varphi_2$$

$$at \ z = H \qquad (3.47)$$

and

$$(u_z)_2 = \frac{\partial \varphi_2}{\partial z} + \frac{\partial \psi_2}{\partial x} = (u_z)_3 = \frac{\partial \varphi_3}{\partial z} + \frac{\partial \psi_3}{\partial x}$$

$$(\sigma_{zx})_3 = \mu_3 \left(2\frac{\partial^2 \varphi_3}{\partial x \partial z} - \frac{\partial^2 \psi_3}{\partial z^2} + \frac{\partial^2 \psi_3}{\partial x^2} \right) = 0$$

$$(\sigma_{zz})_2 = \lambda_2 \nabla^2 \varphi_2 = (\sigma_{zz})_3 = (\lambda_3 + 2\mu_3)\nabla^2 \varphi_3 - 2\mu_3 \left(\frac{\partial^2 \varphi_3}{\partial x^2} - \frac{\partial^2 \psi_3}{\partial x \partial z} \right)$$

$$at \ z = H + h \qquad (3.48)$$

and

$$(u_x)_3 = \frac{\partial \varphi_3}{\partial x} - \frac{\partial \psi_3}{\partial z} = (u_x)_4 = \frac{\partial \varphi_4}{\partial x} - \frac{\partial \psi_4}{\partial z}$$

$$(u_z)_3 = \frac{\partial \varphi_3}{\partial z} + \frac{\partial \psi_3}{\partial x} = (u_z)_4 = \frac{\partial \varphi_4}{\partial z} + \frac{\partial \psi_4}{\partial x}$$

$$(\sigma_{zx})_3 = (\sigma_{zx})_4$$

$$(\sigma_{zz})_3 = (\sigma_{zz})_4 \qquad at\ z = H + h + d \qquad (3.49)$$

where H, h, and d are the thickness of 1st, 2nd, and 3rd layer accordingly.

If we substitute the expression of Eq. (3.45) into the boundary conditions Eqs. (3.46)～(3.49), we can obtain 12 equations with 12 variables. To keep those variables having values different from zero, we obtain the dispersion equation as shown in Eq. (3.50).

By solving the dispersion equation Eq. (3.50) with the bisection method based algorithm mentioned in Section 3.2.2, the dispersion curves, which indicate the relation between wave number or frequency versus phase velocity, can be plotted as shown in Fig. 3.24. The material constants used in Fig. 3.24 are shown in Table 3.4.

Table 3.4 Material constants of the Steel-Epoxy-Concrete layered media.

Material	**C_L (m/s)**	**C_T (m/s)**	**ρ (kg/m^3)**	**Thickness (mm)**
Steel	5870	3140	7800	4.5
Water	1500	/	1000	0.09
Epoxy	2500	1112	1120	5
Concrete	4000	2450	2400	∞

Fig. 3.24 presents the dispersion curves of a Steel-Water-Epoxy-Concrete layered media. Compared with Fig. 3.14, the dispersion curves of a Steel-Epoxy-Concrete layered media, the most significant difference is the existence of Scholte wave mode in the water-layer-contained model, whose asymptotic velocity in high frequency range is the longitudinal wave velocity in water (c_w). More details about Scholte wave will be given in Section 3.7. The value and pattern of the other modes are very close in these two models. The 2nd mode (if we call the Scholte wave as the 1st mode) starts from the Rayleigh wave speed of half-space (4th layer) c_{R4}, and other modes start from transverse wave speed of half-space (4th layer) c_{T4} with cutoff frequencies. All the modes asymptotically trend to the transverse wave speed of 3rd layer c_{T3} as frequency tends towards infinity.

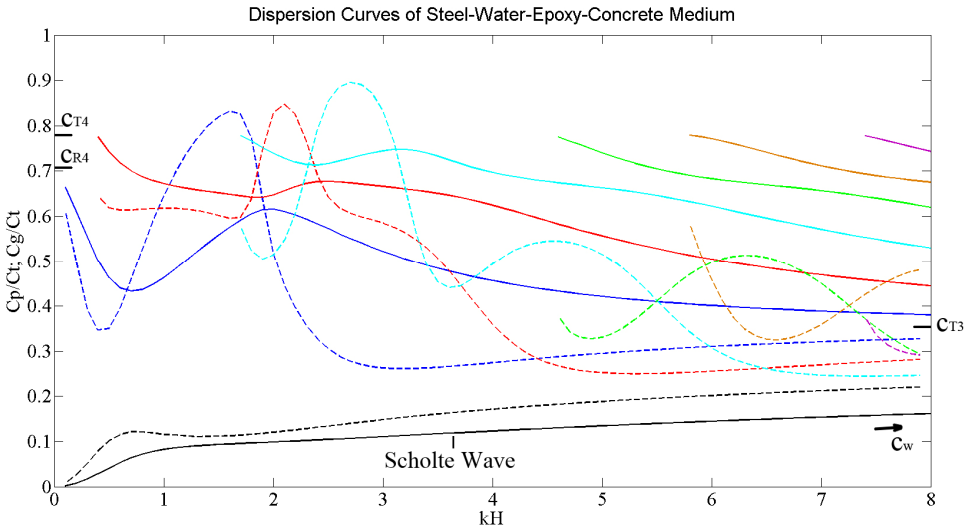

Fig. 3.24 Dispersion curves of a Steel-Water-Epoxy-Concrete media: solid line, phase velocity; dashed line, group velocity.

$$\Delta =$$

$$\begin{vmatrix}
\left(2k^2-k_{\beta 1}^2\right)e^{\nu_1 H} & \left(2k^2-k_{\beta 1}^2\right)e^{-\nu_1 H} & 2k\nu_1^{'}e^{\nu_1^{'}H} & -2k\nu_1^{'}e^{-\nu_1^{'}H} & 0 & 0 & 0 & 0 & 0 & 0 & 0 & 0 \\
2k\nu_1 e^{\nu_1 H} & -2k\nu_1 e^{-\nu_1 H} & \left(2k^2-k_{\beta 1}^2\right)e^{\nu_1^{'}H} & \left(2k^2-k_{\beta 1}^2\right)e^{-\nu_1^{'}H} & 0 & 0 & 0 & 0 & 0 & 0 & 0 & 0 \\
-\nu_1 & \nu_1 & -k & -k & \nu_2 & -\nu_2 & 0 & 0 & 0 & 0 & 0 & 0 \\
-2k\nu_1 & 2k\nu_1 & -\left(2k^2-k_{\beta 1}^2\right) & -\left(2k^2-k_{\beta 1}^2\right) & 0 & 0 & 0 & 0 & 0 & 0 & 0 & 0 \\
\left(2k^2-k_{\beta 1}^2\right) & \left(2k^2-k_{\beta 1}^2\right) & 2k\nu_1^{'} & -2k\nu_1^{'} & \frac{\lambda_2}{\mu_1}k_{\alpha 2}^2 & \frac{\lambda_2}{\mu_1}k_{\alpha 2}^2 & 0 & 0 & 0 & 0 & 0 & 0 \\
0 & 0 & 0 & 0 & -\nu_2 e^{-\nu_2 d} & \nu_2 e^{\nu_2 d} & \nu_3 e^{-\nu_3 d} & -\nu_3 e^{\nu_3 d} & ke^{-\nu_3^{'}d} & ke^{\nu_3^{'}d} & 0 & 0 \\
0 & 0 & 0 & 0 & 0 & 0 & -2k\nu_3 e^{-\nu_3 d} & 2k\nu_3 e^{\nu_3 d} & -\left(2k^2-k_{\beta 3}^2\right)e^{-\nu_3^{'}d} & -\left(2k^2-k_{\beta 3}^2\right)e^{\nu_3^{'}d} & 0 & 0 \\
0 & 0 & 0 & 0 & \frac{\lambda_2}{\mu_3}k_{\alpha 2}^2 e^{-\nu_2 d} & \frac{\lambda_2}{\mu_3}k_{\alpha 2}^2 e^{\nu_2 d} & \left(2k^2-k_{\beta 3}^2\right)e^{-\nu_3 d} & \left(2k^2-k_{\beta 3}^2\right)e^{\nu_3 d} & 2k\nu_3^{'}e^{-\nu_3^{'}d} & -2k\nu_3^{'}e^{\nu_3^{'}d} & 0 & 0 \\
0 & 0 & 0 & 0 & 0 & 0 & -ke^{-\nu_3(d+h)} & -ke^{\nu_3(d+h)} & -\nu_3^{'}e^{-\nu_3^{'}(d+h)} & \nu_3^{'}e^{\nu_3^{'}(d+h)} & ke^{-\nu_4(d+h)} & \nu_4^{'}e^{-\nu_4^{'}(d+h)} \\
0 & 0 & 0 & 0 & 0 & 0 & -\nu_3 e^{-\nu_3(d+h)} & \nu_3 e^{\nu_3(d+h)} & -ke^{-\nu_3^{'}(d+h)} & -ke^{\nu_3^{'}(d+h)} & \nu_4 e^{-\nu_4(d+h)} & ke^{-\nu_4^{'}(d+h)} \\
0 & 0 & 0 & 0 & 0 & 0 & 2k\nu_3 e^{-\nu_3(d+h)} & -2k\nu_3 e^{\nu_3(d+h)} & \left(2k^2-k_{\beta 3}^2\right)e^{-\nu_3^{'}(d+h)} & \left(2k^2-k_{\beta 3}^2\right)e^{\nu_3^{'}(d+h)} & -2\frac{\mu_4}{\mu_3}k\nu_4 e^{-\nu_4(d+h)} & -\frac{\mu_4}{\mu_3}\left(2k^2-k_{\beta 4}^2\right)e^{-\nu_4^{'}(d+h)} \\
0 & 0 & 0 & 0 & 0 & 0 & \left(2k^2-k_{\beta 3}^2\right)e^{-\nu_3(d+h)} & \left(2k^2-k_{\beta 3}^2\right)e^{\nu_3(d+h)} & 2k\nu_3^{'}e^{-\nu_3^{'}(d+h)} & -2k\nu_3^{'}e^{\nu_3^{'}(d+h)} & -\frac{\mu_4}{\mu_3}\left(2k^2-k_{\beta 4}^2\right)e^{-\nu_4(d+h)} & -2\frac{\mu_4}{\mu_3}k\nu_4^{'}e^{-\nu_4^{'}(d+h)}
\end{vmatrix}$$

$$= 0$$

(3.50)

3.6.2 Wave Structure Analysis

Fig. 3.25～Fig 3.27 show the wave structures of first three modes of the Steel-Water-Epoxy-Concrete layered media. Since the amplitudes of displacements in the water layer are much larger and always linear, the wave structures are shown separately without showing the one in water layer. As we can see from those figures, the most notable differences of wave structure between each modes are found in the epoxy layer (the 3rd layer), from which we can easily distinguish those modes from each other. Also, when the frequency goes high ($kH = 5$), higher order mode behaves more curving than lower order mode. The analysis of wave structure can help us to judge the correctness of the plotting of the dispersion curves, and to understand the development of the displacements in each layers when the frequency changes.

3.7 Scholte Wave

Now we look into the wave mode that always exists when there is a liquid layer among the solid layers, the Scholte Wave, or the Stoneley-Scholte Wave [Talmant et al., 1989; Uberall et al., 1994; Bao et al., 1997; Sessarego et al., 1997].

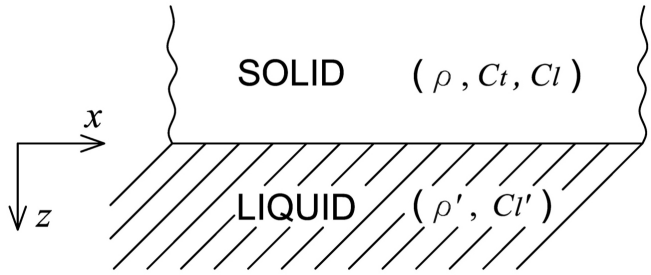

Fig. 3.28 A solid-liquid interface.

For a two layer model with a solid-liquid interface as shown in Fig. 3.28, we can list the boundary conditions as:

$$(u_z)_1 = \frac{\partial \varphi_1}{\partial z} + \frac{\partial \psi_1}{\partial x} = (u_z)_2 = \frac{\partial \varphi_2}{\partial z} + \frac{\partial \psi_2}{\partial x}$$

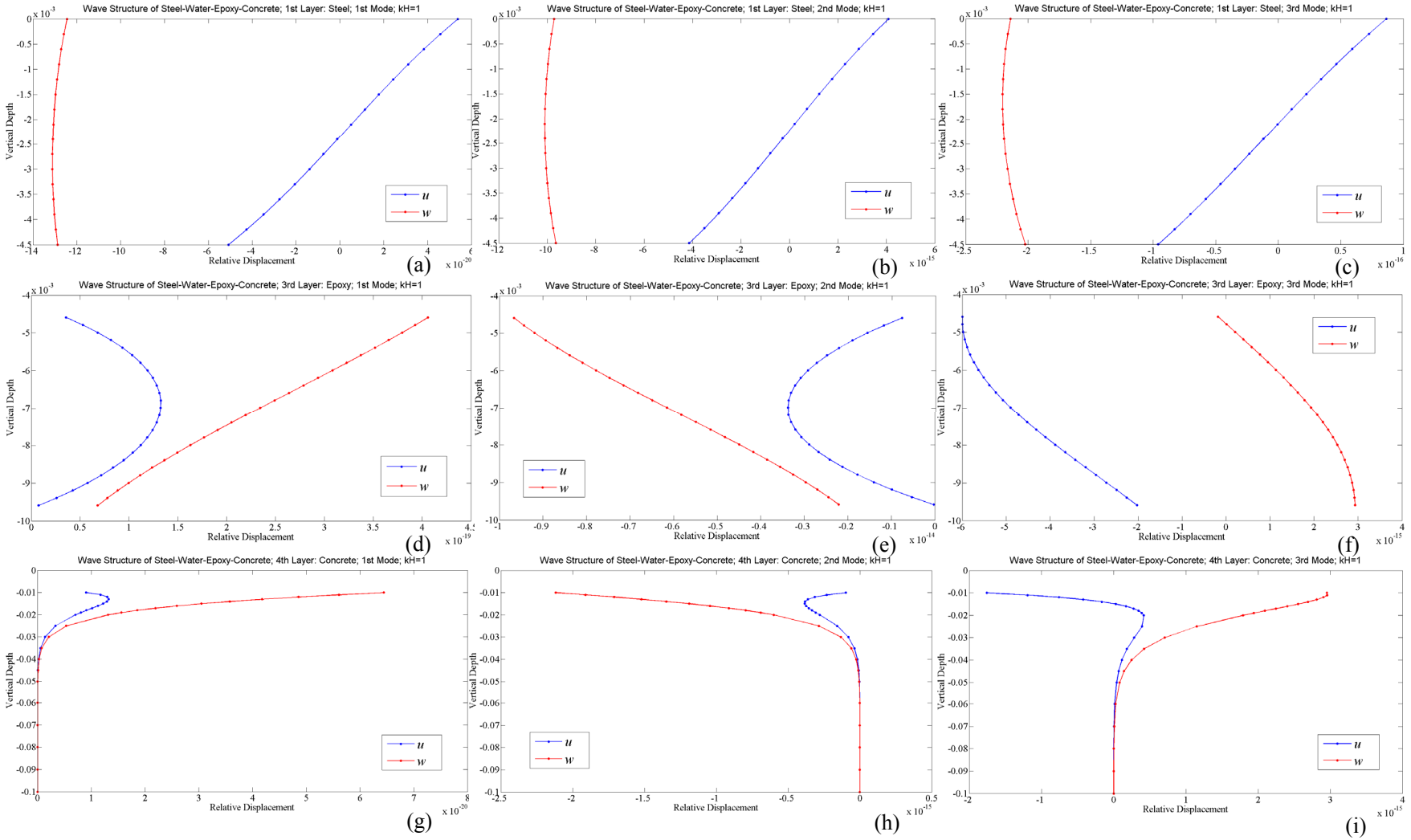

Fig. 3.25 Wave structures of 1st, 2nd, and 3rd modes of a Steel-Water-Epoxy-Concrete layered media, when kH=1, showing u (blue line) and w (red line) displacement profiles in layers of steel (a,b,c), epoxy (d,e,f), and concrete (g,h,i) respectively.

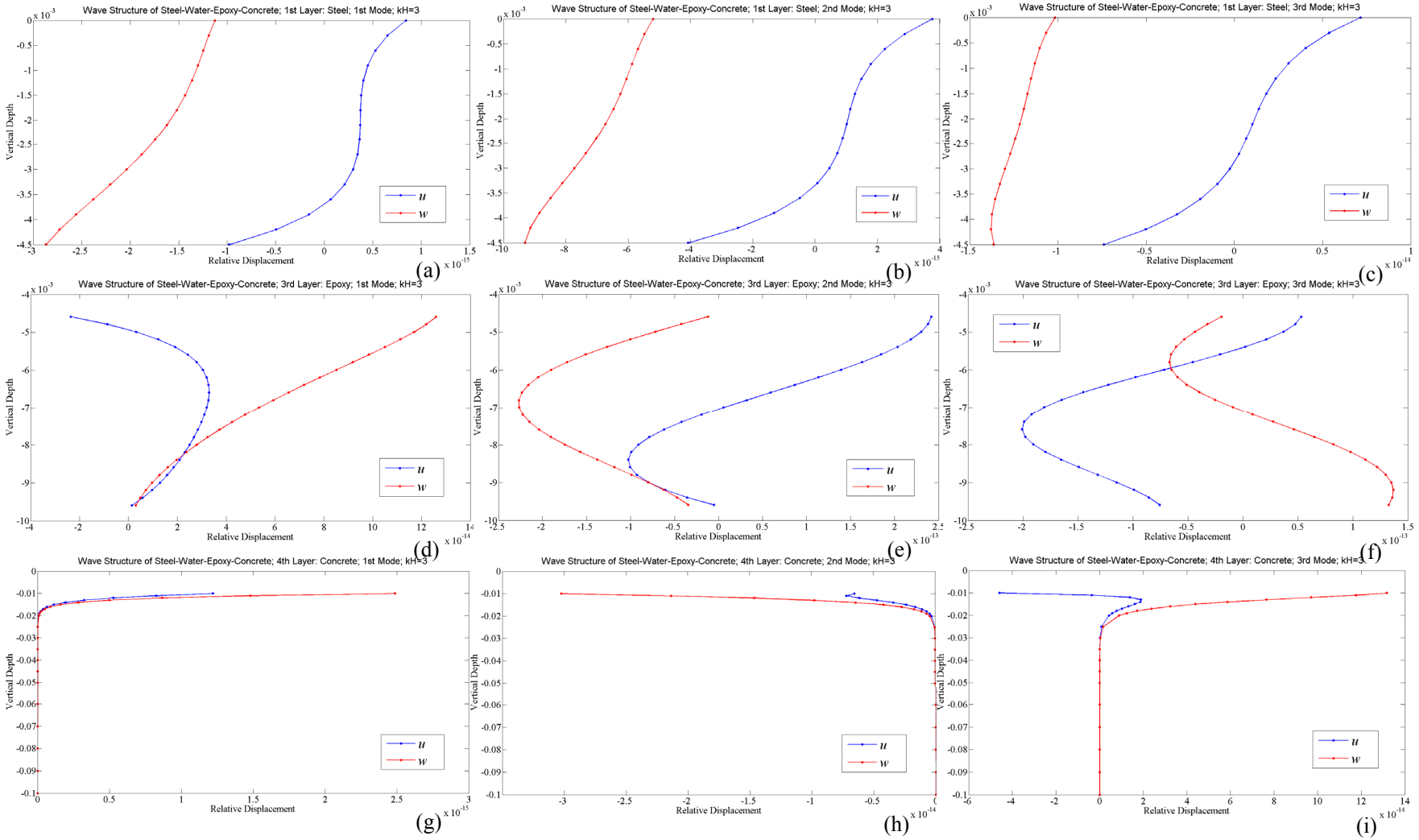

Fig. 3.26 Wave structures of 1st, 2nd, and 3rd modes of a Steel-Water-Epoxy-Concrete layered media, when kH=3, showing u (blue line) and w (red line) displacement profiles in layers of steel (a,b,c), epoxy (d,e,f), and concrete (g,h,i) respectively.

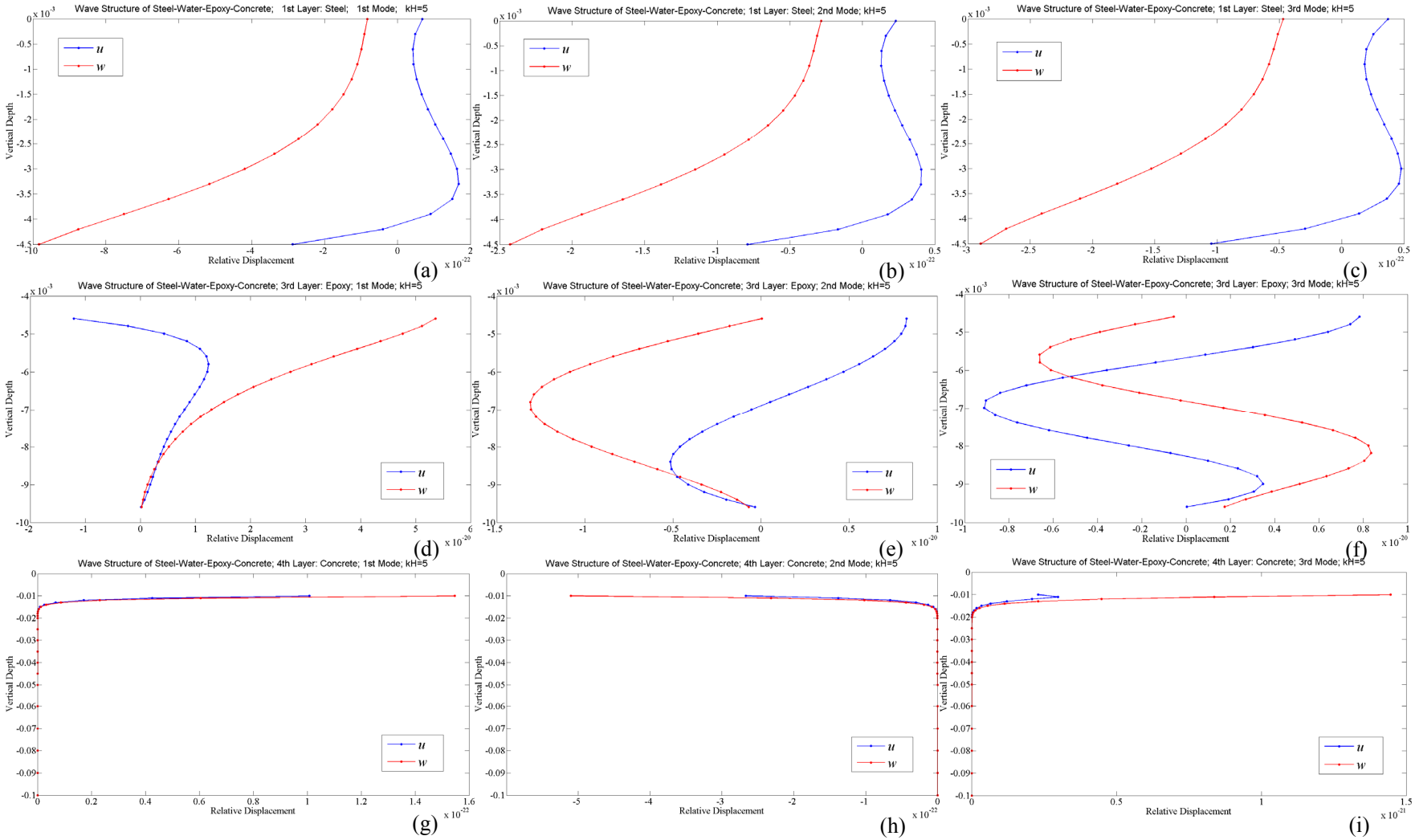

Fig. 3.27 Wave structures of 1st, 2nd, and 3rd modes of a Steel-Water-Epoxy-Concrete layered media, when kH=5, showing u (blue line) and w (red line) displacement profiles in layers of steel (a,b,c), epoxy (d,e,f), and concrete (g,h,i) respectively.

$$(\sigma_{zz})_1 = (\sigma_{zz})_2$$

$$(\sigma_{zx})_1 = 0 \qquad at\ z = 0. \tag{3.51}$$

The boundary equations yield a determinant, the solutions of which correspond to the existence of surface waves propagating at the interface between a solid and a liquid media. The resolution of the determinant reduces to the following secular equation:

$$4\left(\frac{c_T}{c}\right)^2\left[1-\left(\frac{c_T}{c}\right)^2\right]^{1/2}\left[\left(\frac{c_T}{c_L}\right)^2-\left(\frac{c_T}{c}\right)^2\right]^{1/2}-\left[1-2\left(\frac{c_T}{c}\right)^2\right]^2=\frac{\rho'}{\rho}\left[\frac{\left(\frac{c_T}{c_L}\right)^2-\left(\frac{c_T}{c}\right)^2}{\left(\frac{c_T}{c_L'}\right)^2-\left(\frac{c_T}{c}\right)^2}\right]^{1/2} \tag{3.52}$$

where the $'$ denotes the material properties of the fluid [Billy and Quentin, 1983].

From Eq. (3.52), three waves can be deduced:

Rayleigh Wave: When $\rho' \ll \rho$, e.g. air to solid, the right term can be neglected and the equation reduces to the following form, which is the Rayleigh's equation:

$$\left(\frac{c}{c_T}\right)^6-8\left(\frac{c}{c_T}\right)^4+8\left(\frac{c}{c_T}\right)^2\left[3-2\left(\frac{c_T}{c_L}\right)^2\right]-16\left[1-\left(\frac{c_T}{c_L}\right)^2\right]=0 \tag{3.53}$$

Leaky Rayleigh Wave: The influence of the liquid is expressed by the term on the RHS of Eq. (3.52). Usually the inequality $c_L' < c < c_L$ is satisfied and this additional term is imaginary. The equation is then satisfied for only complex values of variable c. The corresponding wave decays when it propagates on the surface because it continuously radiates energy back into the liquid media at the Rayleigh angle $\theta_R' = \sin^{-1}(c_L'/c_{R'})$. In this relationship $c_{R'}$ is the velocity of Leaky Rayleigh Wave in the solid bounded by a liquid and the inequality $c_R \lesssim c_{R'}$ is always satisfied.

Scholte Wave: In addition to the generalized Rayleigh wave it has been shown that a real solution of Eq.(3.52) exists. This solution corresponds to a surface wave whose phase velocity

is somewhat smaller than the acoustic velocity in the liquid ($c_S \lesssim c_L'$). Most of its energy is localized in the liquid and its direction of propagation is parallel to that of Rayleigh wave.

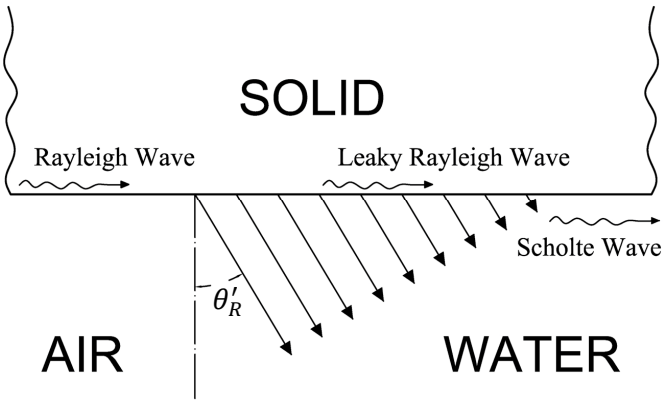

Fig. 3.29 Rayleigh Wave, Leaky Rayleigh Wave and Scholte Wave on the solid-air, and solid-water interfaces.

The relationship of these three waves and their propagation on the solid-air, solid-water interfaces can be described by Fig. 3.29.

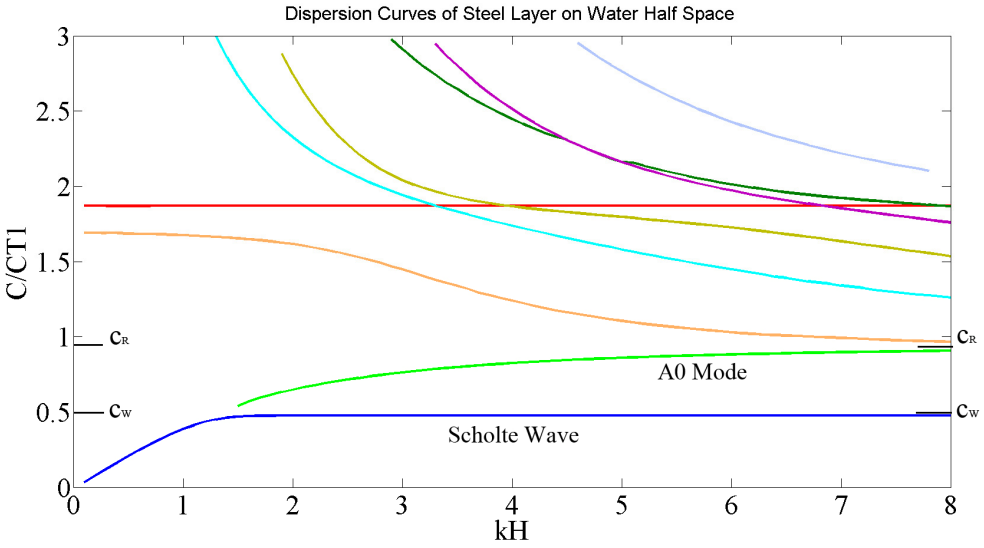

Fig. 3.30 Dispersion curves of a steel-water half space model.

Fig. 3.30 presents the dispersion curves of a model of lying a steel plate on a water half space. We can clearly find the Scholte wave who has a limit velocity very close to the acoustic velocity in water. The A0 mode has almost the same trend with Scholte wave at low frequencies,

but when frequency increases, it reaches to the Rayleigh wave velocity of steel (c_R) instead of c_w.

Since the Scholte wave is principally located propagating in the liquid, and the wave is of maximum intensity at the interface and decreases exponentially away from the interface into both the fluid and the solid media [Luppe and Doucet, 1988], people can hardly detect it from the solid side, if the solid layer is thick. Many researches about obtaining this wave were all based on the measurement in the liquid [Favretto and Rabau, 1997; Cegla et al., 2005]. Though from the aspect of dispersion curves, we can clearly find the difference between "with water layer model" and "without water layer model" through the existence of Scholte wave, we can hardly obtain it experimentally if we set our transducer on the solid side.

3.8 Summary

Dispersion curves and wave structures of different multi-layered media have been obtained through the solving of dispersion equations respectively. The cases of pure solid and water layer contained can be compared on the aspect of dispersion curves. The most significant difference is the existence of Scholte wave mode when there is solid-liquid interface in the multi-layered media. However, the detection of Scholte wave will meet some restriction. Hence, in order to distinguish the water layer beneath a solid layer by using dispersion curves, shape's change of other wave modes, especially the 1st mode, needs to be paid more attention. Among these different cases, the dispersion curves analysis of Steel-Epoxy-Concrete layered media will be continued in the next chapter with epoxy's material constants varying. The wave structure analysis is very helpful for us to judge the modes' development when we have modes' intersection or adjacency on the curves. For the future work, the algorithm of the root searching can be improved by a more advanced large size matrix solving program to reduce the calculation time.

CHAPTER 4

MATERIAL PROPERTY ESTIMATION IN LAYERED MEDIA

4.1 Introduction

This chapter will focus on the first applied instance of this study: the material property estimation for multi-layered media. In the results of Chapter 3, we can obtain the theoretical dispersion curves of Steel-Epoxy-Concrete layered media with different material constants of the epoxy layer. Then in this chapter, an ultrasonic NDE test on the steel-epoxy-concrete bonding specimens will be taken. The SASW method will be applied into data processing to obtain the experimental dispersion curves of the specimen. Through an inversion process based on a variance function for multi-modes between the analytical and experimental dispersion curves, the elastic property of the epoxy layer can be estimated, which will be introduced in the Explicit Finite Element Method (EFEM) model as the material property setting. Through the 3-D EFEM simulation, the surface wave propagation inside the specimen can be visualized, and the numerical dispersion curves can also be plotted through the spectrum analysis of

numerical waveforms. The numerical result can be used to further verify the accuracy of the material property estimation approach.

4.2 Analysis of Dispersion Curves

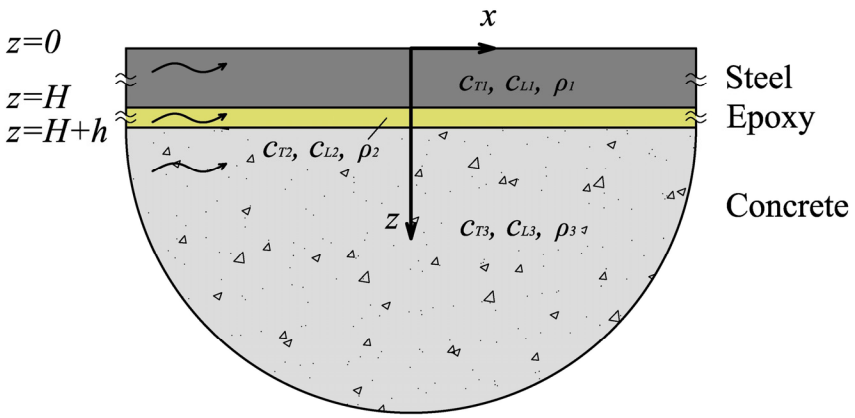

Fig. 4.1 A Steel-Epoxy-Concrete 3 layers model: 2 layers overlying on a half space.

The dispersion curves of multi-layered media are quite sensitive to layer's material properties. The stiffening (longitude and transverse phase velocities of lower layer are larger than those of upper layer) and softening (phase velocities of lower layer are smaller than those of upper layer) media can have significantly different dispersion properties. For instance, in a copper-epoxy-aluminum composite media [Wu and Chen, 1996], in which the third layer aluminum has the highest phase velocity, only one mode can be activated in the concerned frequency range, and in high frequency range, wave propagates with Rayleigh wave speed of the first layer; in a softening layered media however, due to a low phase velocity of the half-space, when the phase velocity nearly equals the transverse velocity of the half-space, the mode will cease to propagate, which is called "cutoff effect" [Nayfeh and Chimenti, 1984]. Here, a model of steel-epoxy-concrete layered media is studied, which belongs to the softening media as concrete in the bottom and softest material epoxy in the middle, as shown in Fig. 4.1.

In Table 4.1, four models of material property are presented. In all of these models, the properties of steel layer are set to be unchangeable. To understand the effect of different

material properties of epoxy layer to dispersion curves, the phase velocities of epoxy are raised in sequence from Model 1 to Model 3, where all of these settings are based on a real possibility of epoxy material. The material of concrete is approximated as homogeneous in those analytical models, and because it is difficult to be precisely qualified on its elastic constants, we propose an enhanced constants setting of concrete in Model 4 to see its influence. Fig. 4.2 shows the analytical dispersion curves of the four models in Table 4.1.

Table 4.1 Material parameters assumptions for analytical dispersion curves

Model	Layer's Material	P-wave velocity C_L (m/s)	S-wave velocity C_T (m/s)	Density (kg/m^3)	Thickness (mm)
Model 1	Steel	5870	3140	7800	4.5
	Epoxy	1600	800	1120	5
	Concrete	3400	2200	2400	∞
Model 2	Steel	5870	3140	7800	4.5
	Epoxy	2000	1000	1120	5
	Concrete	3400	2200	2400	∞
Model 3	Steel	5870	3140	7800	4.5
	Epoxy	2500	1112	1120	5
	Concrete	3400	2200	2400	∞
Model 4	Steel	5870	3140	7800	4.5
	Epoxy	2500	1112	1120	5
	Concrete	4000	2450	2400	∞

In Model 1 (Fig. 4.2 a), phase velocities of all the modes decrease faster than they do in other models as the lowest phase velocity of the 2nd layer is assumed. An interesting phenomenon is that the dispersion curve of the 4th mode seems to be cut when its phase velocity reaches c_{T3}, and be excited again when frequency increases. This phenomenon again confirms that the phase velocity of guided waves must be less than the shear wave velocity of the last layer in a stratified half-space. Otherwise, the energy of this guided wave will be infinite when the depth z tends towards infinity [Zhang and Lu, 2003]. In Model 2 (Fig. 4.2 b), due to the increment of elastic constants of epoxy layer, the "hook" of the 1st mode curve is pulled up to meet the 2nd mode closely. Then in Model 3 (Fig. 4.2 c), with a relative high elastic constants of epoxy, the 1st mode has crossed over the 2nd mode and reaches closely to c_{T3}, which is the

limitation of the wave speed in this media. In Model 4 (Fig. 4.2 d), the high elastic constants of concrete has clearly lifted the curves of all the modes up as the maximum values of those curves are determined by the material property of half-space, however, the minimum values, determined by the second layer, are almost same as the ones in Model 3.

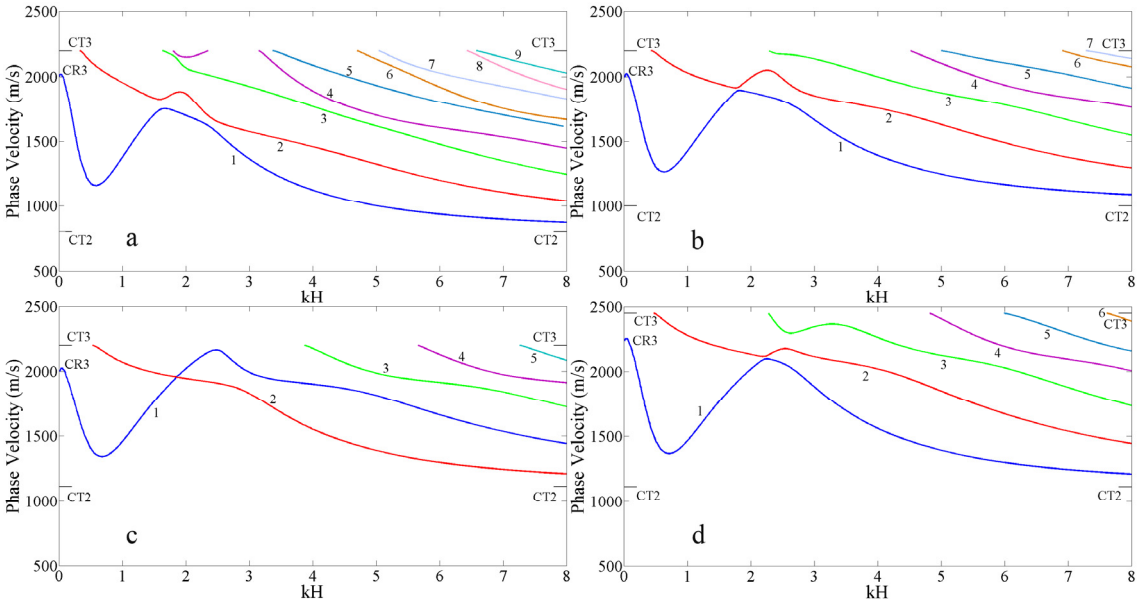

Fig. 4.2 Dispersion curves of a steel plate in vacuum (symmetric modes)

Different frequency ranges of dispersion curves are sensitive or insensitive to different parameters. In relative high frequency range (above 230kHz), theoretically, the dispersion curves are sensitive to the change of elastic properties: c_L and c_T of epoxy layer. However, due to the decrease of 1st mode's velocity, and more energy contribution of other higher modes, those multi-modes are hard to be detected and distinguished. When the frequency goes even higher, for a wave with very short wavelength, the layered half-space is equivalent to a homogeneous half-space composed of the first layer's material only. Hence, although theoretically, there is no mode can be excited whose phase velocity is greater than c_{T3}, it still should be considered that the limit of the phase velocity in high frequency range is c_{R1}, which is the Rayleigh wave speed of the first layer. The practical measurement also shows that, in high frequency range, the detectable wave's speed is quite close to the Rayleigh wave speed of

steel. Therefore, for the parameter of epoxy's elastic constants, we found that the range of 20kHz~160kHz, which is around the "hook" shape part of the 1st mode, is the most distinguishable and sensitive part of dispersion curves with even small change of elastic constants values. After knowing each parameter's effect on dispersion curves and its sensitivity to those parameters, we decide to use ultrasonic transducer of 200kHz central frequency as transmitter and receiver, and we can roughly predict the shape of the analytical dispersion curves and the range of phase velocities before conducting calculation, which can efficiently improve the inversion process in the later work [Shen et al., 2014].

4.3 Ultrasonic Nondestructive Test on Steel-Epoxy-Concrete Layered Specimen

4.3.1 Experiment Setup

A steel-epoxy-concrete 3 layer bonding specimen has been manufactured approximating to the composite structure on RC bridge strengthened by steel plates. Firstly a concrete block (400mm×400mm×150mm) was casted, then it was supported above a steel plate (500mm×500mm×4.5mm) with a gap of 5mm, after that the epoxy was injected into the gap evenly, as shown in Fig. 4.3. When the epoxy finished hardening, the ultrasonic transducers can be set on the steel plate (Fig. 4.4).

To get the compressive elastic modulus (E_c) of the concrete casted in the specimen, a compression test has been conducted on sample concrete cylinder, with diameter of 100mm, length of 200mm, and density of $2400kg/m^3$. Fig. 4.5 shows the deformation (compressive strain) of the cylinder under the compressive loads from 0kN to 156kN. Two strain gauges were installed on the opposite sides of the cylinder, and the respective strain values were averaged as the deformation of cylinder. According to the linear fitting, the compressive elastic modulus $E_c = 28.92\text{Gpa}$.

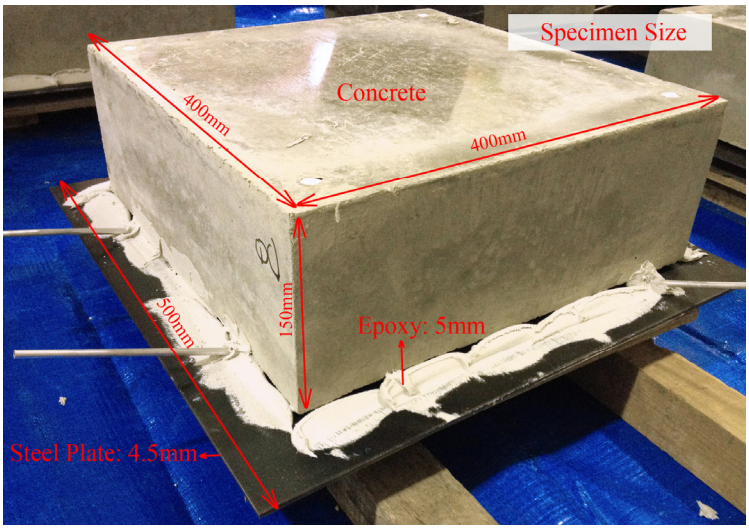

Fig. 4.3 A Steel-Epoxy-Concrete specimen (epoxy injection).

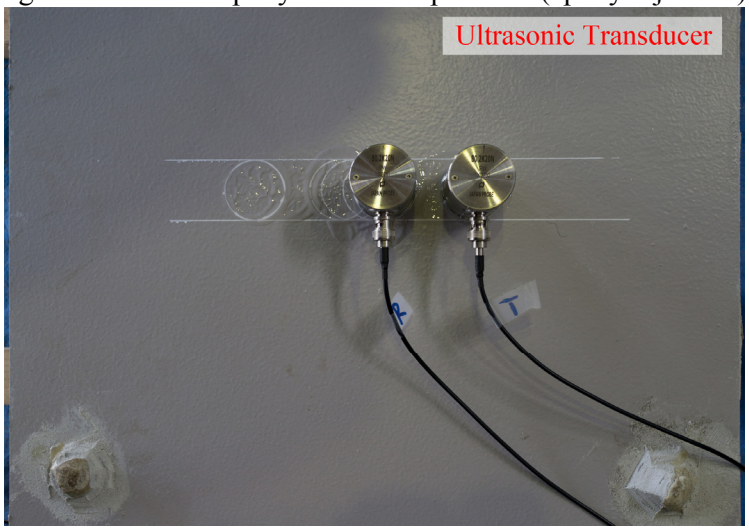

Fig. 4.4 Ultrasonic transducers setting on the specimen.

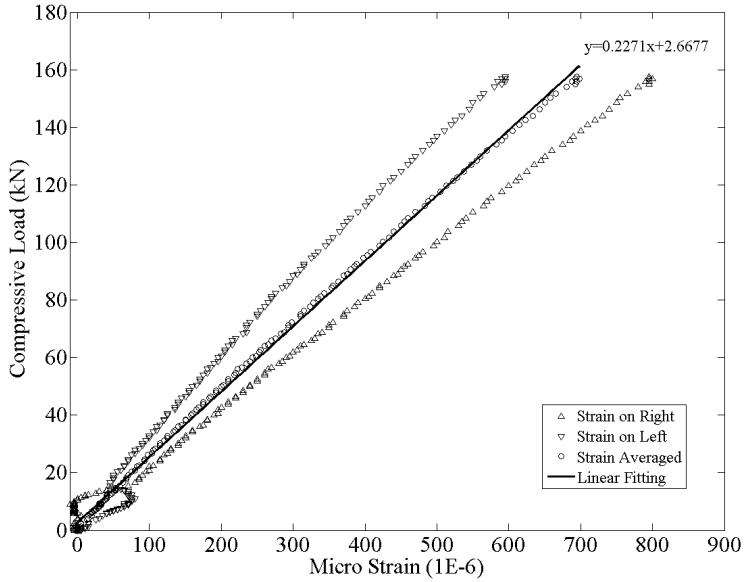

Fig. 4.5 Diagram of the bisection method based algorithm for roots searching.

However, in this study, the dynamic modulus (E_d) of concrete rather than the static compressive modulus (E_c) should be used. Several attempts have been made to correlate static compressive (E_c) and dynamic (E_d) moduli for concrete [Neville, 1997; Lydon and Balendran, 1986]. The simplest of these empirical relations is proposed by [Lydon and Iacovou, 1995]:

$$E_c = 0.83\, E_d \tag{4.1}$$

According to Eq. (4.1), the dynamic modulus of the concrete used in the specimen is $E_d = 34.84\text{Gpa}$. With a given Poisson's ratio of 0.2, the longitudinal and transverse phase velocity of the concrete used in the specimen is about: $c_L = 4000m/s$; $c_T = 2450m/s$. These values will be used in the following inversion process, as the known parameters of the analytical dispersion curves.

Fig. 4.6 shows the setup of the nondestructive test on the steel-epoxy-concrete 3 layer specimen. Two normal-type ultrasonic transducers of frequency of 200kHz are used in this NDE test. A pitch-catch method is applied, with one transducer as transmitter and another one as receiver. To keep good signal coherence, the transmitter and receiver are the same type. The diameter of the transducer's contact surface is 34.2mm. They are vertically set on the plane of the specimen, to produce normal-type ultrasonic wave. As conducting media, Glycerine is pasted between transducers and specimen. The contact pressure of transmitting and receiving transducer is produced by their self-weight of 325g. An integrated high power ultrasonic pulser&receiver is utilized in this test. The generated frequency range of pulser is 30kHz～10MHz, and the detectable frequency range of receiver is 300Hz～30MHz. In this test, one cycle of pulse wave (rectangular wave) with frequency of 200kHz is employed as incident wave and will be generated by the pulser. The pulser&receiver is controlled by a portable computer with parameter setting and pulser's trigger releasing. The received signal is also recorded in the PC with real-time wave form presenting and FFT spectrum analyzing. This ultrasonic testing system is light-weight, portable for field testing; meanwhile, it has a wide

working frequency range for different objective to be detected, as long as corresponding working frequencies' transducers are utilized.

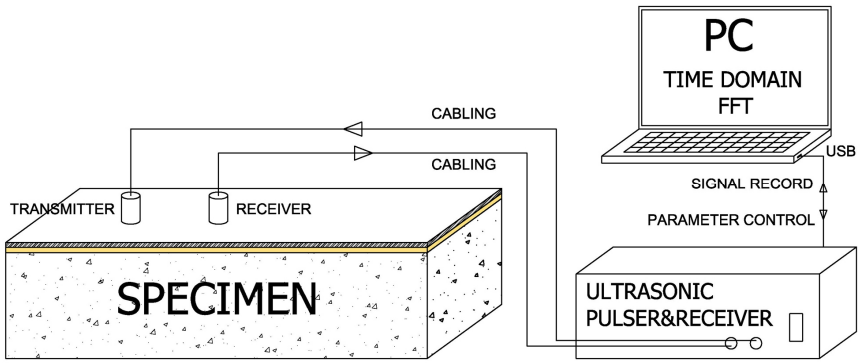

Fig. 4.6 Experiment setup.

4.3.2 Test's Procedure and Transducers' Calibration Setting

To know the transducers' characteristic more specifically, a pulse-echo test has been conducted on a homogeneous Polymethylmethacrylate (PMMA) block, with the dimension of 400mm×152mm×152mm. Identical with the following tests, one cycle of 200kHz pulse wave is generated by the pulser, which is transmitted by the transducer and reflected by the opposite face (152mm) of the block, then received by the same transducer. Fig. 4.7 shows the waveform of the 1st reflected wave; Fig. 4.8 shows its Fourier spectrum, from which we can see that the effective frequency range of this type of transducer is from 50kHz to 350kHz, as the incident wave is 200kHz.

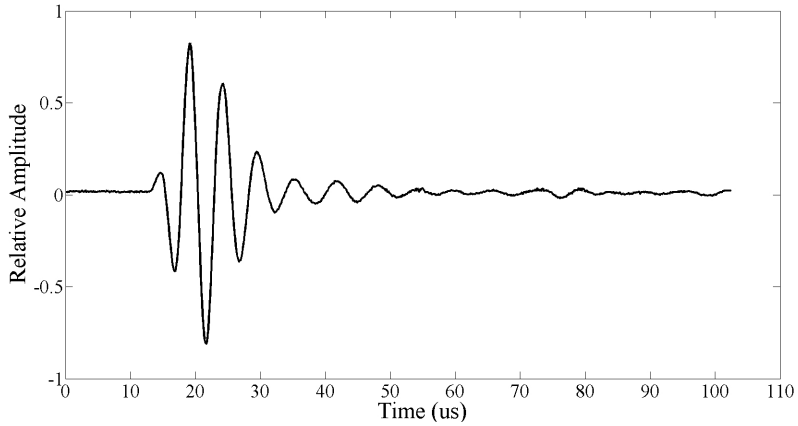

Fig. 4.7 Pulse-Echo test on a homogeneous PMMA block: received waveform.

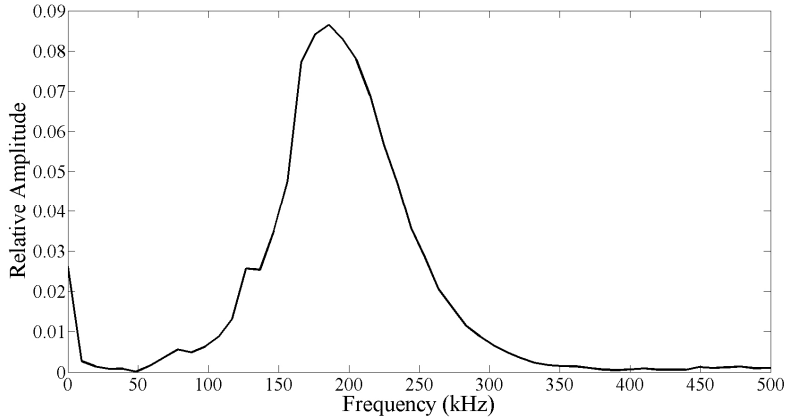

Fig. 4.8 Pulse-Echo test on a homogeneous PMMA block: Fourier spectrum.

As shown in Fig. 4.9, the receiver is positioned on two spots symmetrically off the center line with a distance D apart. These two spots are marked as R_1 and R_2, and the position of transmitter is marked as T. During the test, the receiver is firstly positioned on R_1, detecting the surface wave signal from R_1, then it is shifted to R_2, keeping the same pulse wave from the transmitter on T. Although the signals from R_1 and R_2 are not recorded simultaneously, by keeping the pulser's parameters and distance between transmitter and receiver identical, this method of single receiver shifting can be equivalent to the detection using double receivers simultaneously.

Fig. 4.9 shows the plan of transducer setting in the experiment. Because our interested frequency range is about 20kHz~160kHz, and especially 20kHz~60kHz, in which the most distinguishable (sensitive) part: the bottom of the 1st mode's "hook" exists, so a relatively large spacing between receivers is adopted. In low frequency range (below 50kHz), the corresponding long wavelength requires a relative large receiver spacing, that can probe the wave signal distinctly. For example, at f =20kHz, the wavelength is about 75mm, to which a comparative receiver spacing distance is needed. However, based on practical experience from repeatedly testing, a too large spacing may cause significant signal attenuation from R_1 to R_2, which is a negative effect in spectral analysis afterwards. In the experiment, the spacing D

between R_1 and R_2 is shifted from 15mm, with every 15mm's interval, until 75mm to find a most proper distance from multiple concerns. Meanwhile, to compare the data collected from two opposite directions, the transmitter is also positioned on two symmetrical spots. Theoretically, if the material is isotropic and homogeneous, and the epoxy layer has uniform thickness, the results obtained from the opposite direction should be the same.

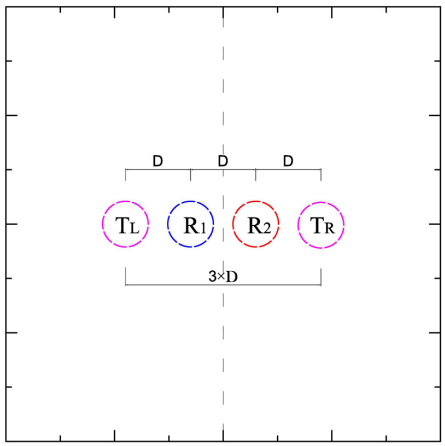

Fig. 4.9 Transducers' position setting on the specimen. (T_L: transmitter on LHS, T_R: transmitter on RHS, R_1: receiver 1, R_2: receiver 2.)

4.4 Spectral Analysis of Surface Waves

From the NDE test, the waveform data in time domain can be obtained. However, it is difficult to extract information regarding to the dispersion properties directly from the time domain signals. The Fast Fourier Transform (FFT) and Spectral Analysis of Surface Waves (SASW) are needed in the signal processing [Nazarian and Desai, 1993]. Then, in frequency domain, the phase difference of the two receivers can be obtained, from which, the relation between phase velocity and frequency or wavenumber, namely, dispersion curves can be plotted experimentally.

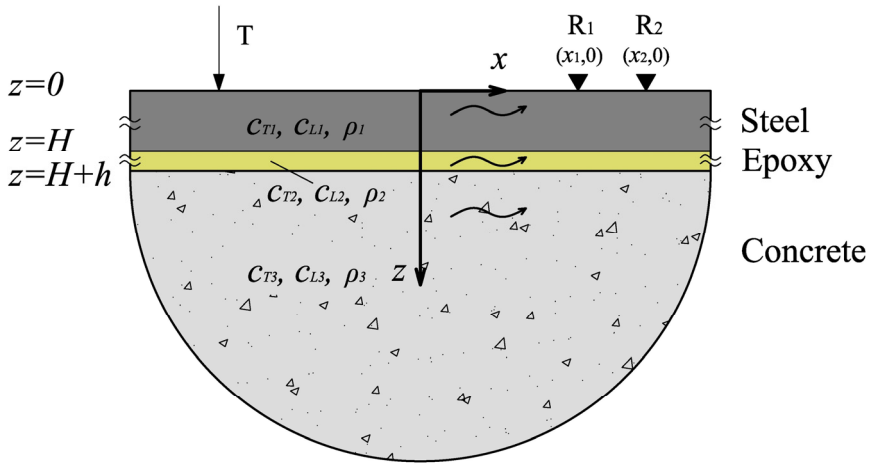

Fig. 4.10 Transmitter and receiver's coordinates on the layered media.

The transducers' coordinates are already shown in Fig. 4.10. If we transform the time domain wave form into frequency domain using FFT, we can have the cross-power spectrum, $\bar{S}_{x1,x2}(f)$, between the two signals from R1 and R2 with distance D, which is defined as

$$\bar{S}_{x1,x2}(f) = \frac{1}{n}\sum_{i=1}^{n}\{[R_1(f)]_i \cdot [R_2^*(f)]_i\} \tag{4.2}$$

where $R_1(f)$ and $R_2(f)$ correspond to the Fourier transforms of time records from two receivers located a distance D apart. The bar above $\bar{S}_{x1,x2}(f)$ corresponds to the frequency-domain average of several records. Parameter n is the number of records averaged, in this study, $n = 3$ is adopted. The asterisk above $R_2(f)$ corresponds to the complex conjugate operator.

Another important function here is the coherence function, $\gamma^2(f)$, which characterizes the signals' reliability. It is calculated from:

$$\gamma^2(f) = \frac{\left|\bar{S}_{x1,x2}(f)\right|^2}{\bar{A}_{x1}(f) \cdot \bar{A}_{x2}(f)} \tag{4.3}$$

where $\bar{A}_{x1}(f)$ and $\bar{A}_{x2}(f)$ correspond to the averaged auto power spectra of records from receiver 1 and receiver 2, respectively. The auto power spectrum for a record $\bar{A}_{xk}(f)$ is defined as:

$$\bar{A}_{xk}(f) = \frac{1}{n}\sum_{i=1}^{n}\{[R_k(f)]_i \cdot [R_k^*(f)]_i\} \qquad (k = 1, 2) \tag{4.4}$$

From RHS of Eq. (4.4), we can see that everything is averaged by *n* times, which means the value of coherence function $\gamma^2(f)$ is a measurement of experimental repeatability. If the recorded signals are reliable, then only tiny difference exists among *n* times' repeat, and the value of $\gamma^2(f)$ will approach to the unity.

For each frequency *f*, the phase shift ϕ can be picked from the cross-power spectrum. The cross-power spectrum $\bar{S}_{x1,x2}(f)$ is a complex-valued parameter. Therefore, the phase is calculated from:

$$\phi = tan^{-1}\frac{Imag\left[\bar{S}_{x1,x2}(f)\right]}{Real\left[\bar{S}_{x1,x2}(f)\right]} \tag{4.5}$$

Knowing the phase, the travel time t can be calculated by:

$$t = \frac{\phi}{2\pi f} \tag{4.6}$$

and the phase velocity *c* can be obtained by:

$$c = \frac{D}{t} = \frac{x_1 - x_2}{\frac{\phi}{2\pi f}} = 2\pi f\frac{x_1 - x_2}{\phi} \tag{4.7}$$

where $D = x_1 - x_2$ is the distance between the receivers.

From Eq. (4.7), the relation between phase velocity c and frequency f is revealed, according to which the experimental dispersion curves can be plotted.

4.5 Estimation of Elastic Properties of Epoxy Layer

4.5.1 Experimental Dispersion Curves

Fig. 4.11 a shows the earlier arrived waveforms observed by the receiver located on R_1 and R_2 when the transmitter is located on the left and right hand side respectively, (see Fig. 4.9

as reference). Fig. 4.11 b shows the later arrived waveforms observed in the two opposite settings. From both figures, we can clearly see that the waveforms obtained from the two opposite position settings of the transducer are quite close, which reveals a good "homogeneity" from different areas of the specimen. In order to focus on the surface wave only but not the reflected wave, a waveform of a short time period (about $130\,\mu s$ here) is cropped. The attenuation of the surface wave after 60mm's propagation is clear through the amplitude comparison between waveforms in Fig. 4.11 a and b.

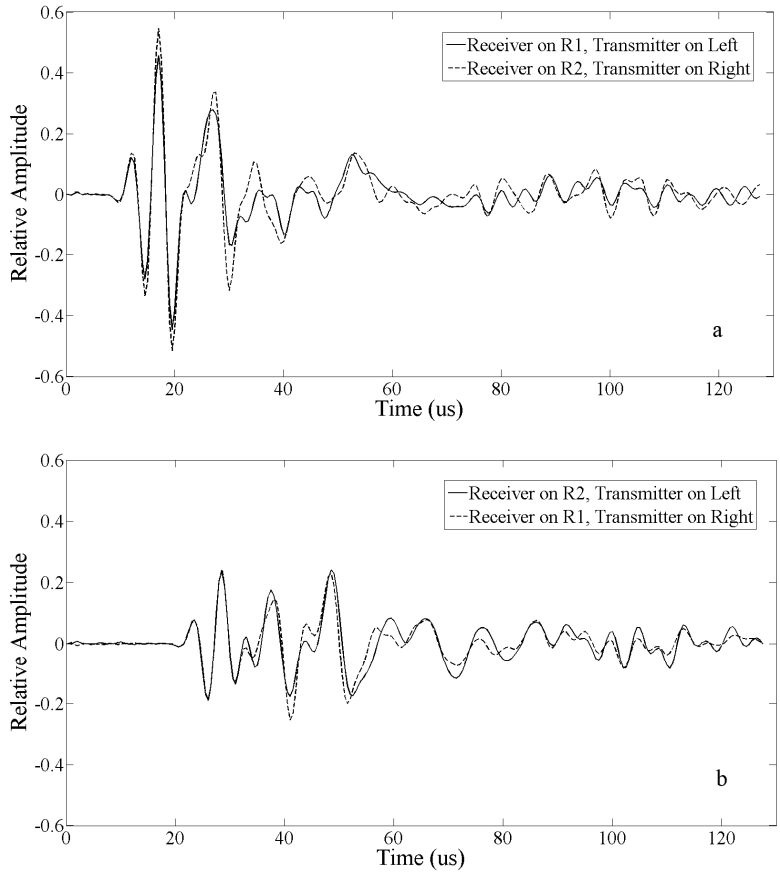

Fig. 4.11 Received waveforms when D=60mm: a, earlier arrived; b, later arrived.

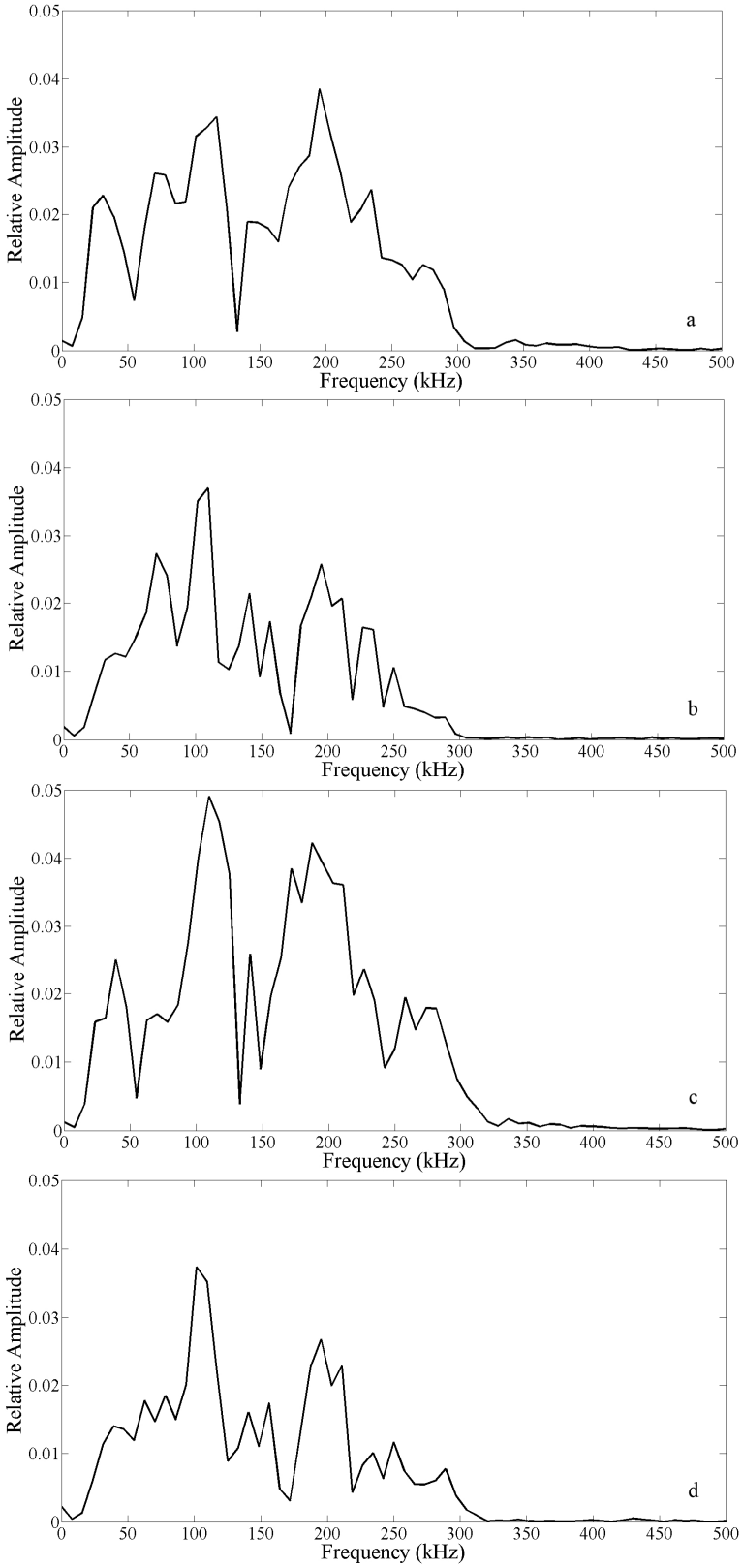

Fig. 4.12 Fourier spectra of waveforms shown in Fig. 4.11: a, received by R_1, emitted by T_L; b, received by R_2, emitted by T_L; c, received by R_2, emitted by T_R; d, received by R_1, emitted by T_R.

Figs. 4.12 a to d show the Fourier spectra of the waveforms in Fig. 4.11. The Fourier spectrum gives a clear sight that main energy of those waves is distributed between 0kHz to 300kHz, among which, around very low frequency near 0kHz and 150kHz, the energy distribution is low with some notable amplitude drops. Usually, for ultrasonic transducer, the performance in very low frequency part is tricky, limited by the working range of the transducer. In the spectral analysis, the waveform with a general even energy distribution on considered frequency range is preferred. The amplitude drop in frequency domain will bring phase information loss, which will be discussed later.

With the Fourier spectrum, according to Eq. (4.2), we can have the cross-power spectrum, $\bar{S}_{x1,x2}(f)$, from which the phase difference of each frequency can be obtained (Fig. 4.14). With Eq. (4.3), the coherence function, $\gamma^2(f)$ (Fig. 4.13) can be calculated. For each position setting, same test will be repeated for n times, in this study, $n = 3$. Since the spectrum analysis is based on the averaged result of these n times' tests, the function value of $\gamma^2(f)$ is a judge of coherence of those tests. If the test is repeatable, namely, the measured data is stable, the coherence value will converge towards one. In Fig. 4.13, the coherence values of both the opposite settings are close to 1 below 300kHz, and become unstable above 300kHz. Thus, only frequency components lower than 300kHz are adopted. However, even in this range, we can also see that at the frequencies near 0kHz, and 150kHz, the coherence value drops by 10% more or less, due to the relatively low energy distribution around there.

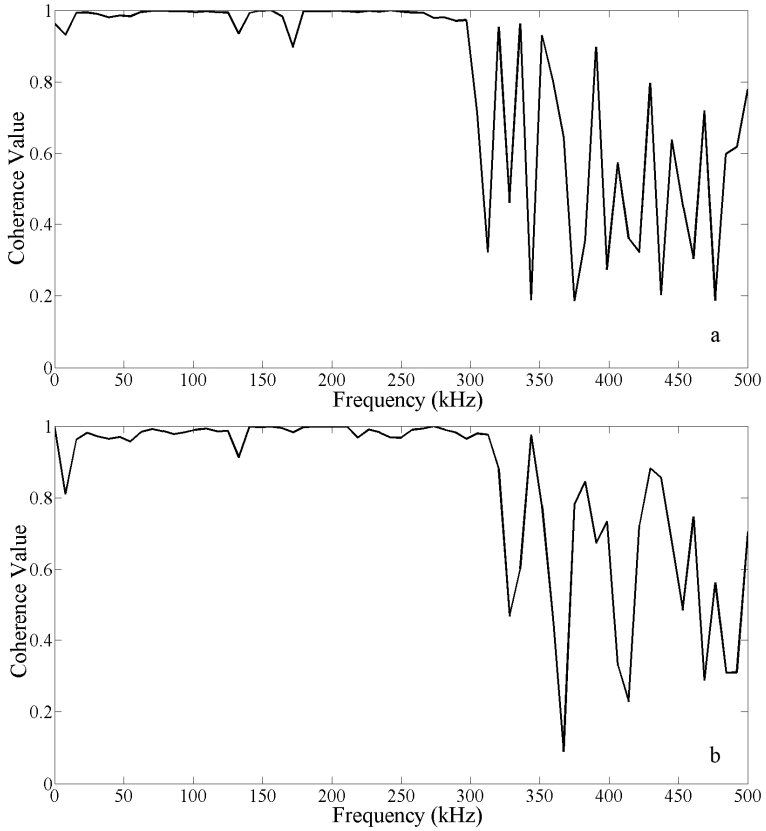

Fig. 4.13 Coherence function value for: a, transmitter on left; b, transmitter on right.

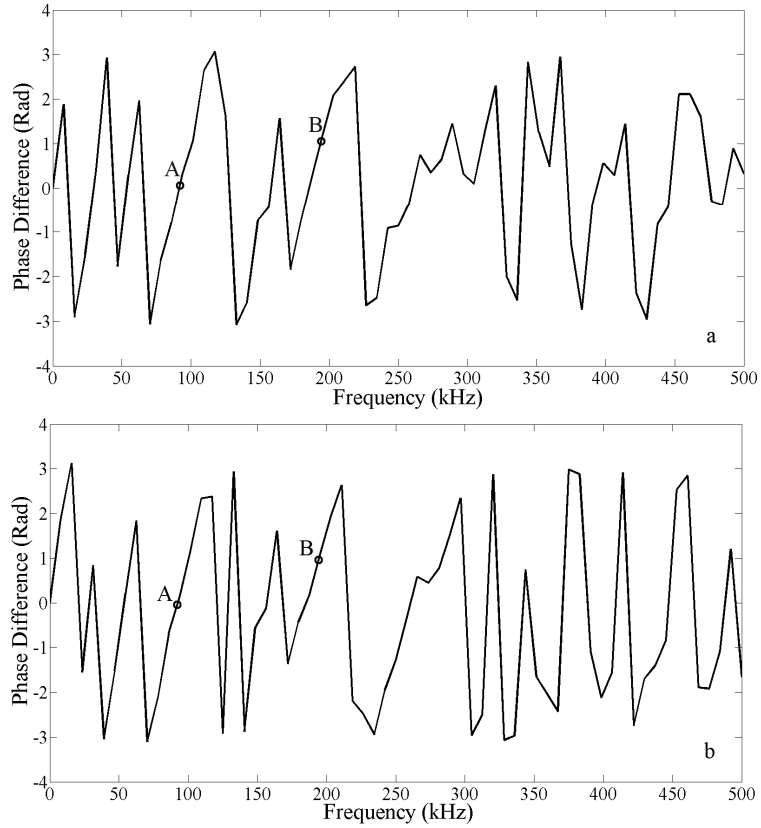

Fig. 4.14 Phase difference of R_1 and R_2 for: a, transmitter on left; b, transmitter on right.

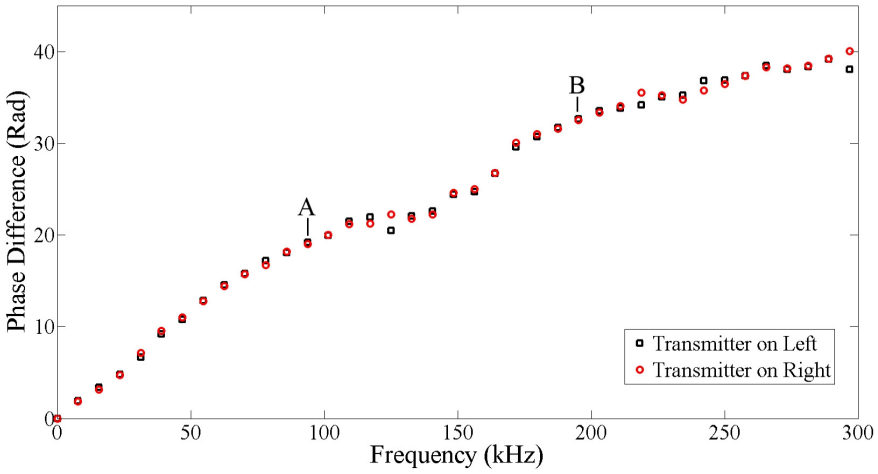

Fig. 4.15 Unfolded phase difference of R1 and R2

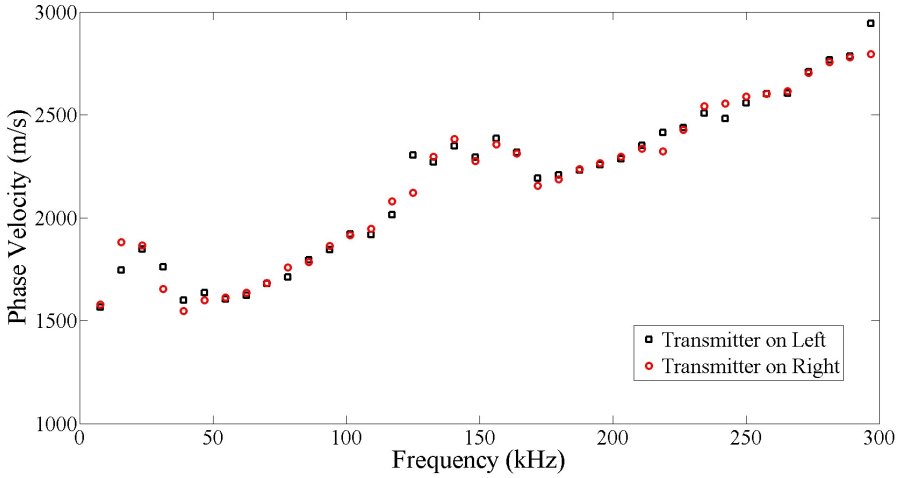

Fig. 4.16 The experimental dispersion curves.

If we unfold the phase difference in Fig. 4.14 from periodic phase to continuous one, we can redraw the continuous phase difference as shown in Fig. 4.15. After unfolding, the data points on A (98kHz) and B (195kHz) in Fig. 4.14 a and b are then located on a continuous phase difference curve as in Fig. 4.15. With the continuous phase difference curve, the experimental dispersion curves then can be plotted (Fig. 4.16) according to Eq. (4.7). In Fig. 4.15 and Fig. 4.16, the results agree well when the transmitter is set oppositely, which shows a good homogeneity of the specimen. From Fig. 4.16, we can see that in the frequency range near 0kHz and around 150kHz, the results do not behave as expected, caused by the amplitude drop in frequency domain (Fig. 4.12) and coherence value drop in Fig. 4.13.

4.5.2 Inversion Process and Material Property Estimation

When both the analytical (Fig. 4.2) and experimental (Fig. 4.16) dispersion curves have been obtained, an inversion process based on a variance function for multi-modes can be applied to find the most appropriate analytical curve, which has minimum difference with the experimental one. The variance function can be expressed as:

$$F_{var} = \frac{\sum_{i=1}^{N}\left[c_{exp}(i) - c_{ant}^{modex}(i)\right]^2}{\sum_{i=1}^{N}\left[c_{exp}(i)\right]^2} \tag{4.8}$$

where i represents each data point in the calculated frequency range and N is the total number of data points utilized in the inversion process. The $c_{exp}(i)$ is the experimental phase velocity obtained from spectrum analysis, and the $c_{ant}^{modex}(i)$ is the analytical phase velocity of the most adjacent mode with the experimental value. When there are multi-modes existing in the frequency range, the algorithm will calculate and compare the distances of those modes' value to the experimental value, and pick up the most adjacent one into the calculation of F_{var}. The value of $c_{ant}^{modex}(i)$ is also affected by several variables such as phase velocity of materials, and layer's depth, as we discussed in Chapter 3. Here, as the epoxy layer's depth is already known, we only consider two parameter variables: the epoxy layer's longitudinal velocity c_{L2} and transverse velocity c_{T2}. Namely, the variance function can be described as:

$$F_{var} = f(c_{L2}, c_{T2}) \tag{4.9}$$

A simplex method (Nelder and Mead, 1965; Karim et al., 1990; Kundu et al., 1991) based minimization process is then applied to find the minimum value of F_{var} from an initial guess of c_{L2} and c_{T2}. A very small critical value will be set to cease the minimum value searching. Fig. 4.17 gives two examples of inversion results of two specimens with different epoxy materials. The same initial guess has been set for these two examples as $c_{L2} = 1600\text{m/s}$ and $c_{T2} = 800\text{m/s}$. After 32 and 18 loops of iteration respectively, the most appropriate analytical curves of the two examples shown in Fig. 4.17 a and b have both been found. The variance

function values of the last loop, namely, the errors of these two inversion processes are 9.0e-4 and 6.3e-4 correspondingly, which meet a good accuracy. The frequency range of the inversion process is from 15kHz to 230kHz, excluding the very low frequency points with low coherence value. Fig. 4.17 a uses the same experimental data as previous figures. From this figure, we can see that the interference of the 2nd wave mode has influenced the measured data around 150kHz, in other words, in this frequency range, the 2nd mode is more easily to be excited than the 1st mode. Hence, the phase velocity measured around 150kHz is mainly from the 2nd mode, which is faster than the 1st mode. The material properties of the analytical curves are listed in Table 4.1, which can be used to estimate the epoxy layer material property of the specimens. From Fig. 4.17 and Table 4.1, we can see that the epoxy used in specimen 1 behaves more rigid than that in specimen 2, with higher longitude and transverse wave velocity.

Before we conduct the inversion process, we need to check the experimental dispersion curve manually and get rid of those obviously deviated phase velocity points refer to the coherence value spectrum and phase difference spectrum. This procedure can efficiently increase the accuracy of the inversion and reduce the convergence time. Hence, obtaining a well-recognized experimental dispersion curve is the basic premise of the following inversion process.

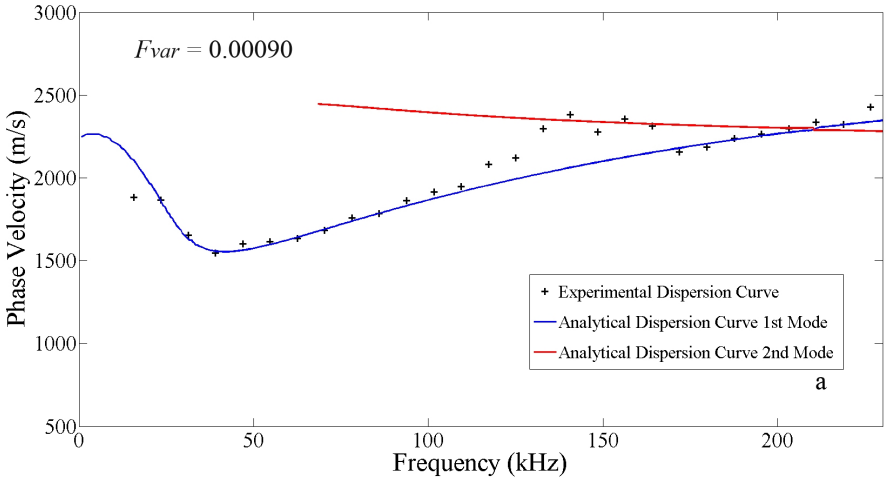

Fig. 4.17 Comparison of the experimental and analytical dispersion curves: a, specimen No.1;

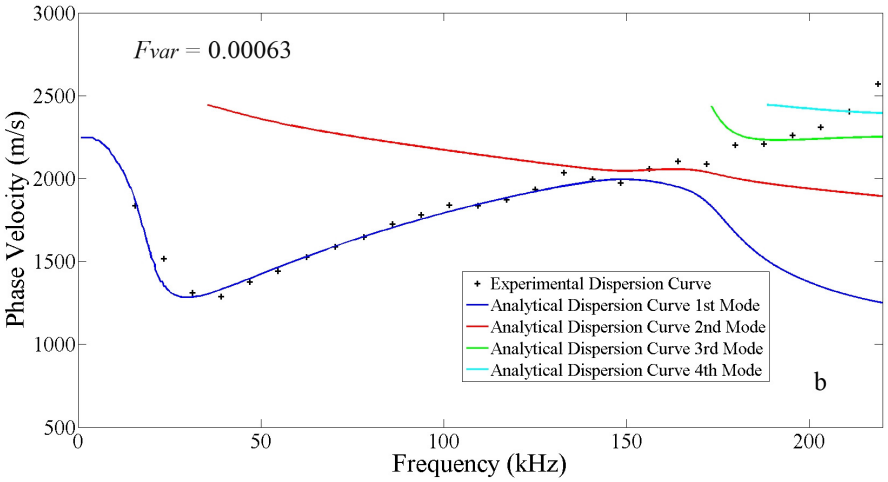

Fig. 4.17 Comparison of the experimental and analytical dispersion curves: b, specimen No.2. The two specimens use different epoxy material.

Table. 4.1 Estimated material property of two specimens.

Layer's Material		Estimated C_L (m/s)	Estimated C_T (m/s)	Density (kg/m^3)	Measured C_L (m/s)
Steel		5870	3140	7800	–
Epoxy	S1	**3000**	**1700**	**1126**	**2903** (+3.34%)
	S2	**2000**	**1000**	**1121**	**1977** (+1.16%)
Concrete		4000	2450	2400	–

Table 4.1 lists the estimated material property of epoxy layer in two different specimens with different types of epoxy through ultrasonic NDE test, spectral analysis and an inversion process between analytical curves and experimental data. The measured longitudinal wave velocities are also obtained through pitch-catch ultrasonic test on cylinder samples of epoxy. A good agreement has been made between estimated and measured data, and the estimated values are slightly larger than the measured values by 3.34% and 1.16% in the two samples respectively. Here, the thickness of the epoxy layer is assumed to be known. In field test, however, the layer thickness is generally unknown, at least partially, and so are the material properties of concrete. These factors need to be considered together in the further research.

4.6 Explicit FEM Simulation and Numerical Dispersion Curves

4.6.1 3-Dimensional Explicit Finite Element Model

With the estimated material property, an FEM model of the steel-epoxy-concrete 3-layered specimen can be built. The wave propagation in the 3-layered media can be simulated and compared with the experimental waveform. The numerical results can help us to verify the feasibility of the NDE test and the accuracy of the experimental data. Through the dispersion curves' comparison from the three different approaches, we can more clearly identify the most distinguishable and sensitive frequency range of the dispersion curves, which can be helpful in the choosing of the proper range of inversion process. The Explicit Finite Element Method (EFEM) is applied to reduce the computational cost per increment when the model is large on space and time approximation. In this EFEM model, we neglect the inhomogeneity of concrete from aggregates. The wavelength of the ultrasonic wave we used in the test is generally larger than the aggregates' dimension; hence the insignificant scattering between aggregates can be neglected without accuracy less.

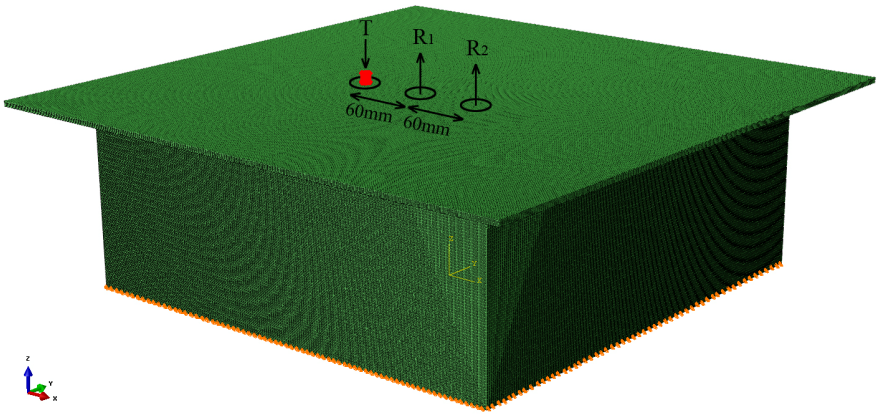

Fig. 4.18 FEM model of steel-epoxy-concrete specimen

A 3-dimensional FEM model of steel-epoxy-concrete specimen has been built (Fig. 4.18). The dimension of steel plate (500mm×500mm×4.5mm) is larger than epoxy layer (400mm ×400mm×5mm) and concrete block (400mm×400mm×150mm), which is the same as real specimen. The 8-node solid cube element is used in this simulation, with the horizontal size of

1mm, the vertical size of 0.9mm in steel plate, 1mm in epoxy layer and 2mm in concrete block. Totally 1.405e7 elements are included. For the two interfaces among steel plate, epoxy layer and concrete block, a fully tied condition is applied, on which the nodes in pair on the same interface is restricted to have the same performance. The explicit method is applied in time analysis, which requires a small time increment but a relatively small computational cost in per increment. Hence, for time discretization, time step of 1e-8s is adopted in whole analysis time of 3.05e-4s. To create a virtual experiment as close as the real experiment, concentrated force loads are applied on several nodes as an area force as the simulation of the transmitting transducer and its contacted area, as marked by "T" in Fig. 4.18. One period of sine wave (200kHz, same as the real pulser) is adopted as the input pulse. The calculated vertical displacement of two nodes distanced the transmitter with 60mm and 120mm, as marked by "R_1" and "R_2" in Fig. 4.18, will be approximately used as signals received by R_1 and R_2. The material constants setting in this model is the same as Specimen 2 in Table 4.1, which is the estimated material property of the layered specimen.

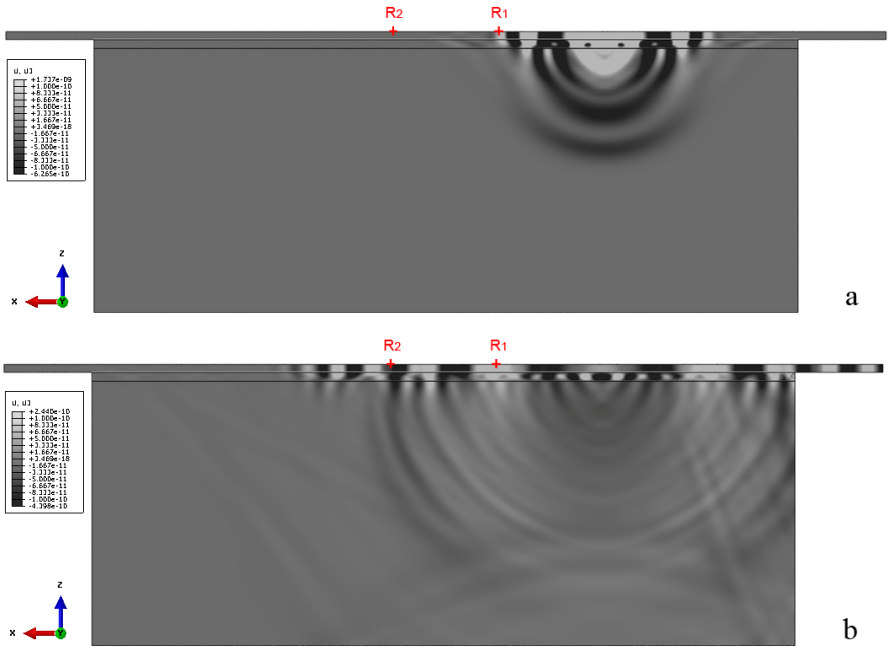

Fig. 4.19 Simulation of wave propagation (u3) on the center section: a, at 20μs; b, at 60μs.

Through 3-D EFEM simulation, the wave propagation inside the 3-layer media can be visualized. Fig. 4.19 shows the waveform on the center section when the 3-D model has been cut by half vertically along the *x*-axis. In Fig. 4.19 a, the surface wave front has just passed through the spot of R_1, but not yet reached R_2. Also, the bulk wave front is clear shown at the 1/2 depth of the concrete, which has already passed through two interfaces but not yet reached the bottom or the edge of the specimen, therefore no reflection wave from there. In Fig. 4.19 b, $40\mu s$ after the time in a, the surface wave has traveled through both R_1 and R_2, meanwhile, the bulk wave has reached the bottom and edge and been reflected by those boundaries. However, from the color map, we can see that the amplitudes of the reflected bulk waves are far smaller than the amplitudes of surface waves and guided waves propagating in steel and epoxy layer. It is revealed that the amplitude's attenuation in the concrete is much more distinct than that in steel and epoxy.

4.6.2 Numerical Dispersion Curves

Fig. 4.20 shows the waveforms on R_1 and R_2. Compared to Fig. 4.11, they are quite familiar both on shape and relative amplitude. In both numerical and experimental signals, the maximum amplitude of waveform of R_2 is almost half of that of R_1, which means the attenuations of the surface wave in both cases are about the same. From Fig. 4.21 a and b, we can see that the amplitude along frequency is gradually decreasing from low frequency to high frequency, especially after 200kHz, the distribution becomes quite low. Because it is impossible to calculate coherence function from the numerical simulation, the only approach to judge the reliability of the phase information is the distribution of frequency's amplitude. If the amplitude is too low, the phase information is no longer useable. Also, in very low frequency part around 0kHz, the numerical signal also meets the limitation, as almost no energy existing in that range.

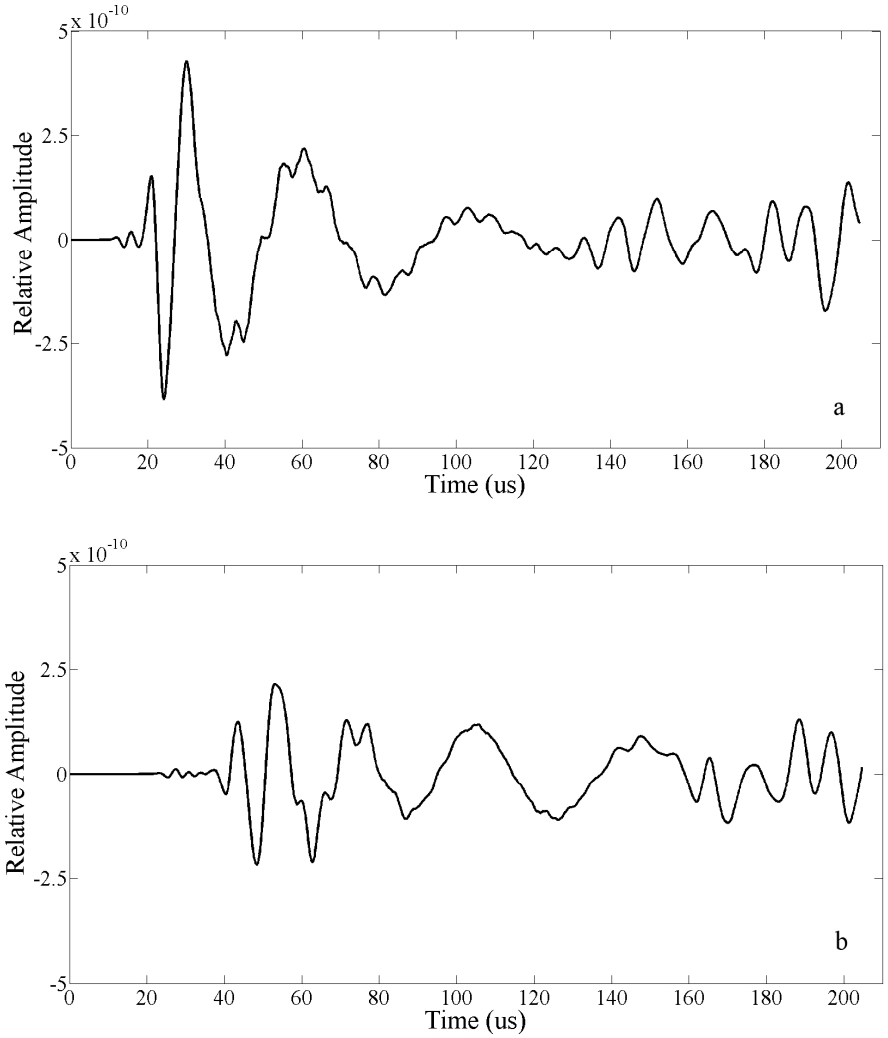

Fig. 4.20 Vertical displacement of: a, node representing R_1; b, node representing R_2.

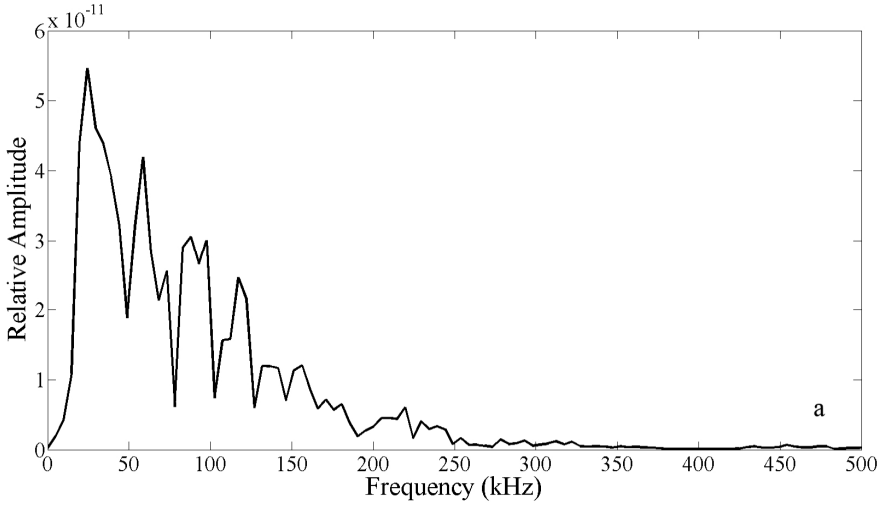

Fig. 4.21 Fourier Spectra of Waveforms Shown in Fig. 4.18: a, node representing R_1;

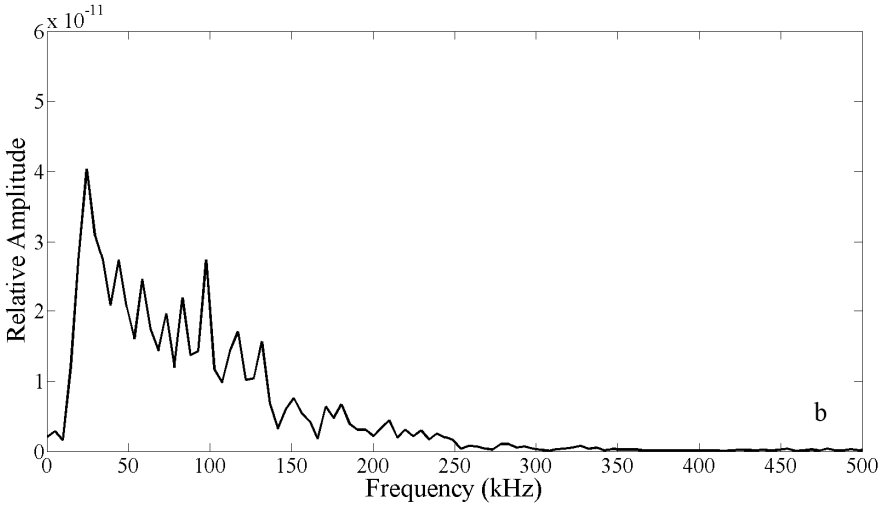

Fig. 4.21 Fourier Spectra of Waveforms Shown in Fig. 4.18: b, node representing R_2.

Through the same procedures as section 4.4, the numerical dispersion curves are obtained, as the points marked by circles in Fig. 4.22. From 20kHz to nearly 160kHz, they are quite agree with the experimental phase velocities and the analytical dispersion curves (the 1st Mode). In low frequency part ($0 < f <$ 20kHz), the matching is not so good, similar as the experimental data performs. In relative high frequency part (160kHz $< f$), the difference between numerical and experimental data shows: the numerical curve is more close to the 2nd Mode of analytical curve; the experimental curve is still rising, where the Rayleigh wave of 1st layer in high frequency starts to contribute the dispersion. From the comparison of the dispersion curves of these 3 types, a clear knowledge has been achieved that the most reliable frequency range for inversion process is (20kHz $< f <$ 160kHz) in this case, almost same as the "hook" part of the 1st Mode, the most distinguishable part of the analytical curves. The FEM simulation validates the experimental data in accuracy and also gives a support to the approach of material property estimation based on SASW method.

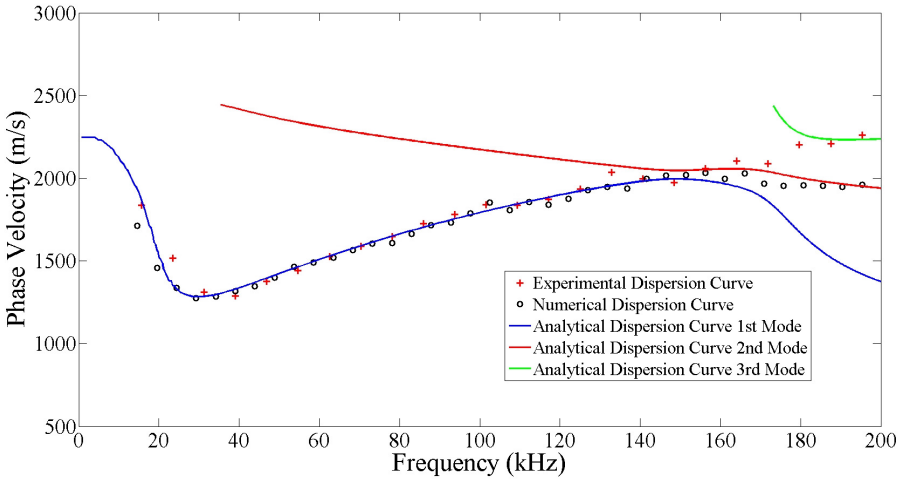

Fig. 4.22 Comparison of analytical, experimental and numerical dispersion curves.

4.7 Summary

Through dispersion curve analysis, we have found that the frequency range of 20kHz~160kHz, around the "hook" shape part of the 1st mode, is the most distinguishable and sensitive part of dispersion curves for variation of elastic constants. Meanwhile, the ultrasonic NDE test and spectral analysis have been applied in constructing of experimental dispersion curves. During this test, cases with different spacings between R_1 and R_2 have been conducted, and a relatively large spacing (60mm) between receivers is recommended, for a low frequency range of 20kHz~160kHz is most interested. Through an inversion process based on a variance function for multi-modes, the matched analytical dispersion curves have been found for two different specimens with a good accuracy. However, the inversion process is highly related with the quality of experimental dispersion curves we obtained. A manual check is needed to exclude those obviously deviated phase velocity points with low coherence values. Based on the estimated material property, the numerical study by a 3-D Explicit FEM model is completed. From the comparison of analytical, experimental, and numerical dispersion curves, it can be revealed that the measured experimental dispersion curves contain multi-dispersion modes, but the most distinguishable and sensitive mode in inversion process is the 1st mode.

CHAPTER 5

WAVE REFLECTION AND TRANSMISSION IN LAYERED MEDIA

5.1 Introduction

Besides dispersion, another important property of the multi-layered media is the reflection and refraction on interfaces. Especially for the way of oblique incidence that we will employed in the following experiments, the comprehensive knowledge of reflection and refraction (transmission) is necessary to be acquired. In this chapter, some basic theories, e.g. Snell's law, critical angle, slowness profile et al., will be firstly introduced. Then, the boundary conditions of different types of interfaces, including solid-solid, solid-liquid, and liquid-solid will be depicted. The reflection factor equations will be deduced, by solving which, the reflection and transmission coefficients of each type of interface will theoretically be calculated. For practical application, the cases of steel-water-steel, steel-water-concrete, and steel-water-epoxy will be emphasized, and they will be utilized to guide and explain the nondestructive detection in Chapter 6.

5.2 Basic Theories of Reflection and Refraction

5.2.1 Oblique Incidence and Snell's Law

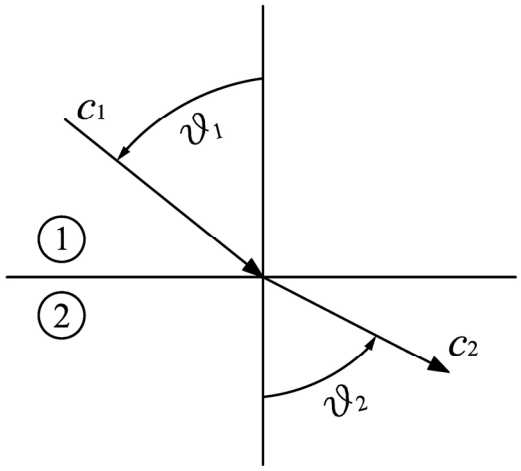

Fig. 5.1 Oblique incidence and the refraction on the interface of two materials.

Several things happen when an ultrasonic wave encounters an interface between two materials at some oblique angle. First of all, refraction occurs in much the same way as it occurs for optical light waves. Consider the diagram in Fig. 5.1, The refracted angle can be computed from Snell's law [Rose, 1999]:

$$c_1 \sin\theta_2 = c_2 \sin\theta_1 \tag{5.1}$$

The second thing that occurs at the interface is mode conversion. Energy is distributed into longitudinal and transverse waves in the second material. Some energy is also reflected, where the angle of reflection is equal to the angle of incidence.

Snell's law can also be used to calculate refracted shear angles in material 2.The following two equations can be deduced from Snell's law (see Fig. 5.2):

$$c_{1L} \sin\theta_{2L} = c_{2L} \sin\theta_{1L} \tag{5.2}$$

$$c_{1L} \sin\theta_{2T} = c_{2T} \sin\theta_{1L} \tag{5.3}$$

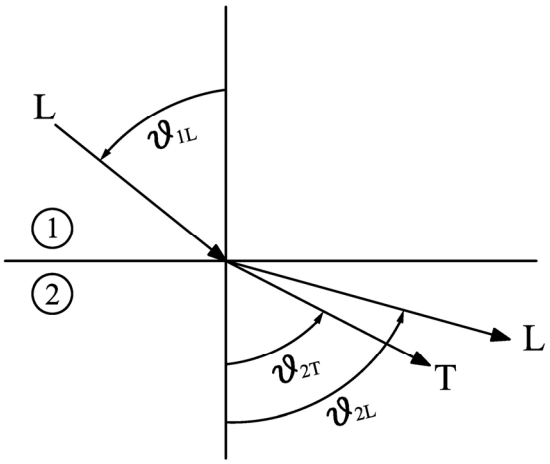

Fig. 5.2 Oblique incidence, refraction, and mode conversion.

5.2.2 Critical Angles

Consideration of Snell's law indicates that two critical angles exist with respect to the refraction process [Rose, 1999].

(1) The first critical angle can be defined as

$$\theta_{cr1} = \sin^{-1}\frac{c_1}{c_{2L}} \qquad when\ \theta_{2L} = 90° \tag{5.4}$$

In this case, all of the longitudinal energy is either reflected or converted to an interface wave. Only transverse waves remain in the second material.

(2) Similarly, the second critical angle can be defined as

$$\theta_{cr2} = sin^{-1}\frac{c_1}{c_{2T}} \qquad when\ \theta_{2T} = 90° \tag{5.5}$$

It occurs when the transverse refracted angle is $90°$. In other words, no significant energy is propagated through the second material; all of the energy is either reflected or transformed into interface wave propagation.

However, those two critical angles would not always exist. For example, if one were to compute the critical angle between steel and Plexiglas, one would find that such an angle does not exist ($\sin\theta > 1$). In other words, refracted angles are less than incident angles if the wave

velocity in the second material is slower than in the first material. On the other hand, refracted angles are greater than incident angles when wave velocities in the second material are greater than in the first material.

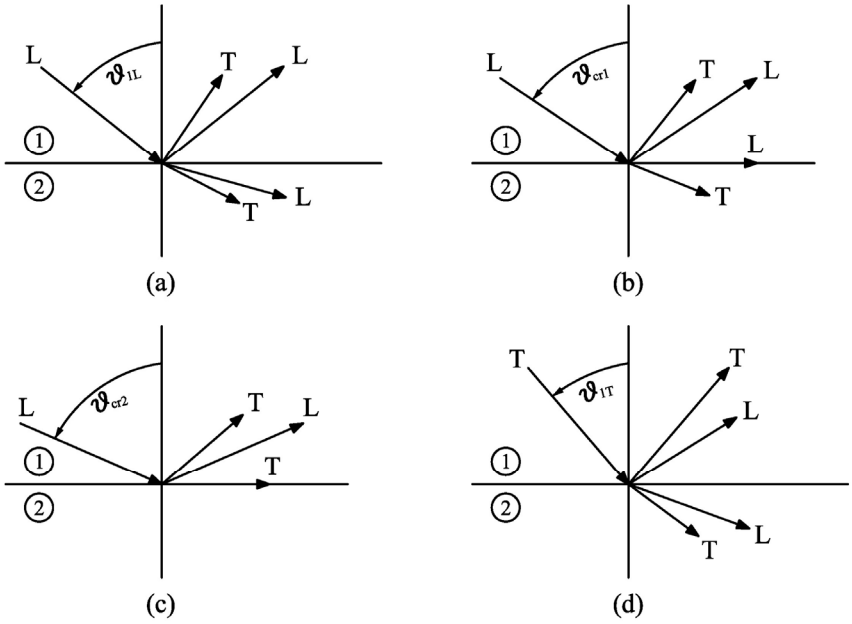

Fig. 5.3 Mode conversion concepts:
(a) general L input; (b) at θ_{cr1}; (c) at θ_{cr2}; (d) general T input.

We may now summarize some important topics on mode conversion associated with the subject of oblique incidence analysis. Fig. depicts four possibilities of mode conversion. Fig.5.3 (a) shows the possible waveforms produced from a longitudinal incident wave at an angle θ_L. Refracted waves in a second material may be longitudinal or transverse; reflected waves also may be longitudinal or transverse. The two refracted and two reflected angles can be calculated from Snell's law. For longitudinal incident waves, the angle of incidence is obviously equal to the angle of reflection.

Fig.5.3 (b) illustrates the situation for an incident angle wave at the first critical angle. Only transverse waves are propagated into the second material, with longitudinal waves going off at an angle of $90°$ and so producing an interface wave. In this case, of course, both

longitudinal and shear waves are reflected. Fig.5.3 (c) illustrates an incident longitudinal wave at the second critical angle. In this case, it is not possible to produce ultrasonic energy in the second material, because both transverse and longitudinal waves are reflected. In Fig.5.3 (d), the transverse wave reflection angle is equal to the transverse wave incident angle.

5.2.3 Slowness Profiles for Refraction

We will now illustrate how slowness profiles can assist us in oblique incidence studies. If a wave encounters an interface between two anisotropic media then wave reflection and refraction will occur. Let's consider symmetric but different elliptic-type slowness profiles, as illustrated in Fig. 5.4 [Rose, 1999]. If a wave is incident to material 1 at a specific angle θ, then the wave vector component k_x along the interface must be preserved. This is simply a restatement of Snell's law:

$$\frac{1}{c_{p1}}\sin\theta_1 = \frac{1}{c_{p2}}\sin\theta_2 \tag{5.6}$$

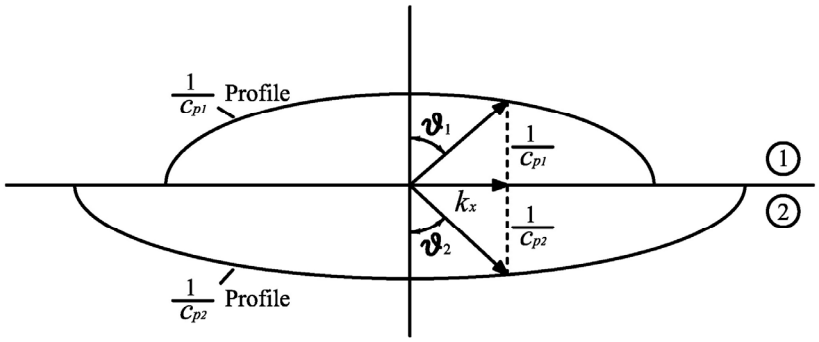

Fig. 5.4 Slowness profiles for calculating refraction angle.

Fig. 5.5 shows how slowness curves can be used to evaluate reflection angles as well as refraction and critical angles. For an incident transverse wave at θ_T, the reflected transverse angle will, of course, still be θ_T. Mode conversion does take place, and some longitudinal waves are reflected also. The reflected longitudinal wave angle will be θ_L, as illustrated in Fig.

5.5, with k_x being preserved. Hence, the longitudinal and transverse reflection angles have the following relationship:

$$\frac{1}{c_L} sin\,\theta_L = \frac{1}{c_T} sin\,\theta_T \tag{5.7}$$

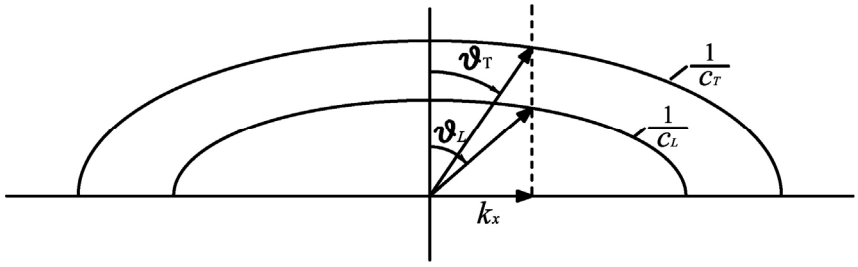

Fig. 5.5 Slowness curves for calculating reflection angles.

5.3 Boundary Conditions

5.3.1 Solid-Solid Boundary Conditions

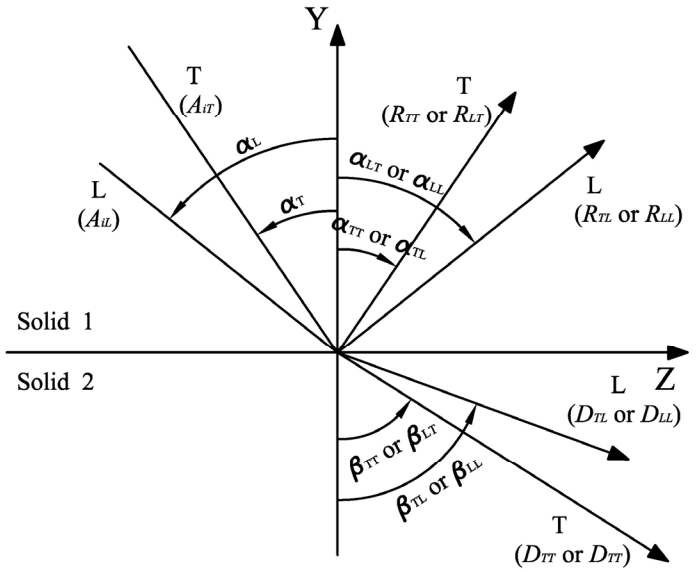

Fig. 5.6 Reflection and refraction at a solid-solid media interface.

The reflection and refraction factors for a perfectly bonded solid-solid interface are derived as follows. Assume that isotropic solid media 1 and 2 are two infinite half-spaces in the

coordinate system XYZ. That is, solid 1 is in the space $y > 0$; solid 2, in $y < 0$ (Fig. 5.6). For transverse wave incidence, we can write expressions for particle velocities; the key to obtaining solutions is satisfying the boundary conditions. For particle velocity V and stress σ_{ij}, the boundary conditions calling for the continuity of particle velocity and stress on $y = 0$ can be written as follows for shear input [Rose, 1999]:

$$\begin{aligned}
V_y\text{:} \quad & (V_T^I)_y + (V_T^R)_y + (V_L^R)_y = (V_T^T)_y + (V_L^T)_y \\
V_z\text{:} \quad & (V_T^I)_z + (V_T^R)_z + (V_L^R)_z = (V_T^T)_z + (V_L^T)_z \\
\sigma_{yy}\text{:} \quad & (\sigma_T^I)_{yy} + (\sigma_T^R)_{yy} + (\sigma_L^R)_{yy} = (\sigma_T^T)_{yy} + (\sigma_L^T)_{yy} \\
\sigma_{yz}\text{:} \quad & (\sigma_T^I)_{yz} + (\sigma_T^R)_{yz} + (\sigma_L^R)_{yz} = (\sigma_T^T)_{yz} + (\sigma_L^T)_{yz}
\end{aligned} \tag{5.8}$$

Here, with V_n^m we have m as R for a reflected wave, T for a transmitted wave, or I for an incident wave; n is either L for a longitudinal wave or T for a transverse wave. For longitudinal input, we would consider V_L^I.

Consider now the following elastic constant-velocity relationships:

$$\rho c_L^2 = \lambda + 2\mu \quad , \qquad \rho c_T^2 = \mu \tag{5.9}$$

$$\lambda_1 + 2\mu_1 \cos^2 \alpha_L = (\lambda_1 + 2\mu_1) \cos(2\alpha_T) \tag{5.10}$$

Given the particle velocity-displacement relationship, the strain-displacement relationship from Eq. (3.2), and the stress-strain relationship (from Hooke's law) for two-dimensional plane strain in isotropic media, we can obtain the stress-particle velocity relationship as follows:

$$\bar{V} = \frac{\partial \bar{u}}{\partial t} = i\omega\bar{u} \qquad (from\ harmonic\ motion\ principles) \tag{5.11}$$

$$\varepsilon_{yy} = \frac{\partial u_y}{\partial y} \qquad \varepsilon_{zz} = \frac{\partial u_z}{\partial z} \qquad \varepsilon_{yz} = \frac{1}{2}\left(\frac{\partial u_y}{\partial z} + \frac{\partial u_z}{\partial y}\right) \tag{5.12}$$

$$\sigma_{yy} = \lambda(\varepsilon_{yy} + \varepsilon_{zz}) + 2\mu\varepsilon_{yy} \quad , \qquad \sigma_{yz} = 2\mu\varepsilon_{yz} \tag{5.13}$$

$$\sigma_{yy} = \frac{1}{i\omega}\lambda\left(\frac{\partial V_y}{\partial y} + \frac{\partial V_z}{\partial z} + 2\mu\frac{\partial V_y}{\partial y}\right) \quad , \quad \sigma_{yz} = \frac{1}{i\omega}\mu\left(\frac{\partial V_y}{\partial z} + \frac{\partial V_z}{\partial y}\right) \tag{5.14}$$

Substituting the particle velocities and stresses into the boundary condition equations, we can find the reflection factor equations,

$$\mathrm{M}\begin{bmatrix} R_{TL} \\ R_{TT} \\ D_{TL} \\ D_{TT} \end{bmatrix} = a_T\,, \qquad and \qquad \mathrm{M}\begin{bmatrix} R_{LL} \\ R_{LT} \\ D_{LL} \\ D_{LT} \end{bmatrix} = a_L\,, \quad respectively, \tag{5.15}$$

where M is a 4×4 matrix:

$$\mathrm{M} = \begin{bmatrix} -\cos\alpha_{LT} & \sin\alpha_{TT} & -\cos\beta_{TL} & \sin\beta_{TT} \\ -\sin\alpha_{LT} & -\cos\alpha_{TT} & \sin\beta_{TL} & \cos\beta_{TT} \\ -k_{L1}(\lambda_1 + 2\mu_1)\cos 2\alpha_{TT} & k_{T1}\mu_1 \sin 2\alpha_{TT} & k_{L2}(\lambda_2 + 2\mu_2)\cos 2\beta_{TT} & -k_{T2}\mu_2 \sin 2\beta_{TT} \\ -k_{L1}\mu_1 \sin 2\alpha_{LT} & -k_{T1}\mu_1 \cos 2\alpha_{TT} & -k_{L2}\mu_2 \sin 2\beta_{TL} & -k_{T2}\mu_2 \cos 2\beta_{TT} \end{bmatrix} \tag{5.16}$$

and, a_T and a_L are 4×1 matrices:

$$a_T = \begin{pmatrix} \sin\alpha_T \\ \cos\alpha_T \\ -k_{T1}\mu_1 \sin 2\alpha_T \\ -k_{T1}\mu_1 \cos 2\alpha_T \end{pmatrix} A_{iT}, \quad and \quad a_L = \begin{pmatrix} -\cos\alpha_L \\ \sin\alpha_L \\ k_{L1}(\lambda_1 + 2\mu_1)\cos 2\alpha_T \\ -k_{L1}\mu_1 \sin 2\alpha_L \end{pmatrix} A_{iL}\,. \tag{5.17}$$

where A_{iT} and A_{iL} are the amplitudes of transverse and longitudinal incident waves respectively.

R_{mn} and D_{mn} are the amplitudes of the reflected or transmitted wave respectively. The subscript m indicates the types of incident waves, and n indicates the types of reflected or transmitted waves.

We call the quotients of R_{mn}/A_{iT} or R_{mn}/A_{iL} as reflection coefficients, and the quotients of D_{mn}/A_{iT} or D_{mn}/A_{iL} as transmission coefficients.

As a sample result, Fig. 5.7 shows the reflection and transmission coefficients for oblique incident angles from 0° to 90° onto an aluminum-Plexiglas interface. We can find that in the case of longitudinal incidence (Fig. 5.7 (a)), the curves are continuous, since there are no critical angles. However in Fig. 5.7 (b), a discontinuity is present because of the critical angle for transverse incidence.

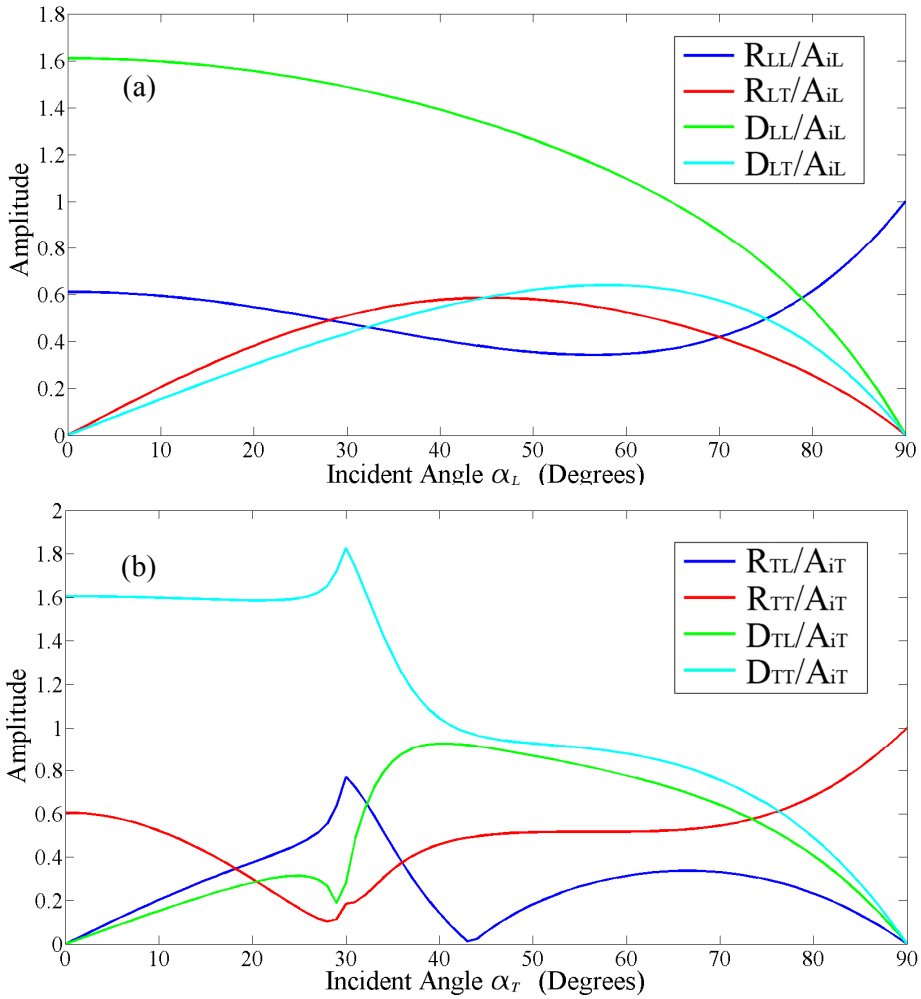

Fig. 5.7 Reflection and transmission coefficients for oblique incidence onto an aluminum-Plexiglas interface: (a), longitudinal incidence; (b), transverse incidence.

5.3.2 Solid-Liquid Boundary Conditions

The reflection and refraction factor equations for a solid-liquid interface (see Fig. 5.8) can be derived in the same way as those for solid-solid boundary conditions. The only difference

is the absence of shear waves in the liquid, which leads to a zero shear stress and to continuity of normal stress and normal particle velocity at the interface [Rose, 1999].

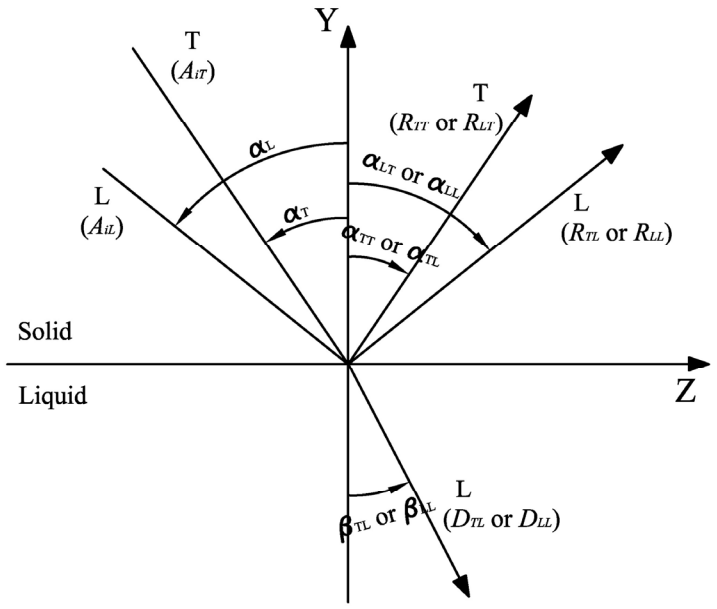

Fig. 5.8 Reflection and refraction at a solid-liquid media interface.

The reflection and refraction equations under these conditions become:

$$\mathrm{M}\begin{bmatrix} R_{LL} \\ R_{LT} \\ D_{LL} \end{bmatrix} = a_L \quad , \quad \mathrm{M}\begin{bmatrix} R_{TL} \\ R_{TT} \\ D_{TL} \end{bmatrix} = a_T \tag{5.18}$$

for longitudinal and transverse incident waves respectively, and this time the matrix M is a 3×3 matrix:

$$\mathrm{M} = \begin{bmatrix} -\cos\alpha_{LT} & \sin\alpha_{TT} & -\cos\beta_{TL} \\ -k_{L1}(\lambda_1 + 2\mu_1)\cos 2\alpha_{TT} & k_{T1}\mu_1 \sin 2\alpha_{TT} & k_{L2}\lambda_2 \\ -k_{L1}\mu_1 \sin 2\alpha_{LT} & -k_{T1}\mu_1 \cos 2\alpha_{TT} & 0 \end{bmatrix} \tag{5.19}$$

There is only longitudinal wave (as incident wave) in the liquid, but both longitudinal and transverse waves exist in the solid layer above. So the vector on RHS of the equation is:

$$a_L = \begin{pmatrix} -\cos\alpha_L \\ k_{L1}(\lambda_1 + 2\mu_1)\cos 2\alpha_T \\ -k_{L1}\mu_1 \sin 2\alpha_L \end{pmatrix} A_{iL} \tag{5.20}$$

$$a_T = \begin{pmatrix} \sin\alpha_T \\ -k_{T1}\mu_1 \sin 2\alpha_T \\ -k_{T1}\mu_1 \cos 2\alpha_T \end{pmatrix} A_{iT} \tag{5.21}$$

for longitudinal and transverse incident waves respectively.

Again we show a sample result of oblique incidence onto an aluminum-water interface in Fig. 5.9. We can see no critical angles in the longitudinal incidence case (Fig. 5.9 (a)), but in the transverse incidence case (Fig. 5.9 (b)), the critical angle occurs beyond 29°.

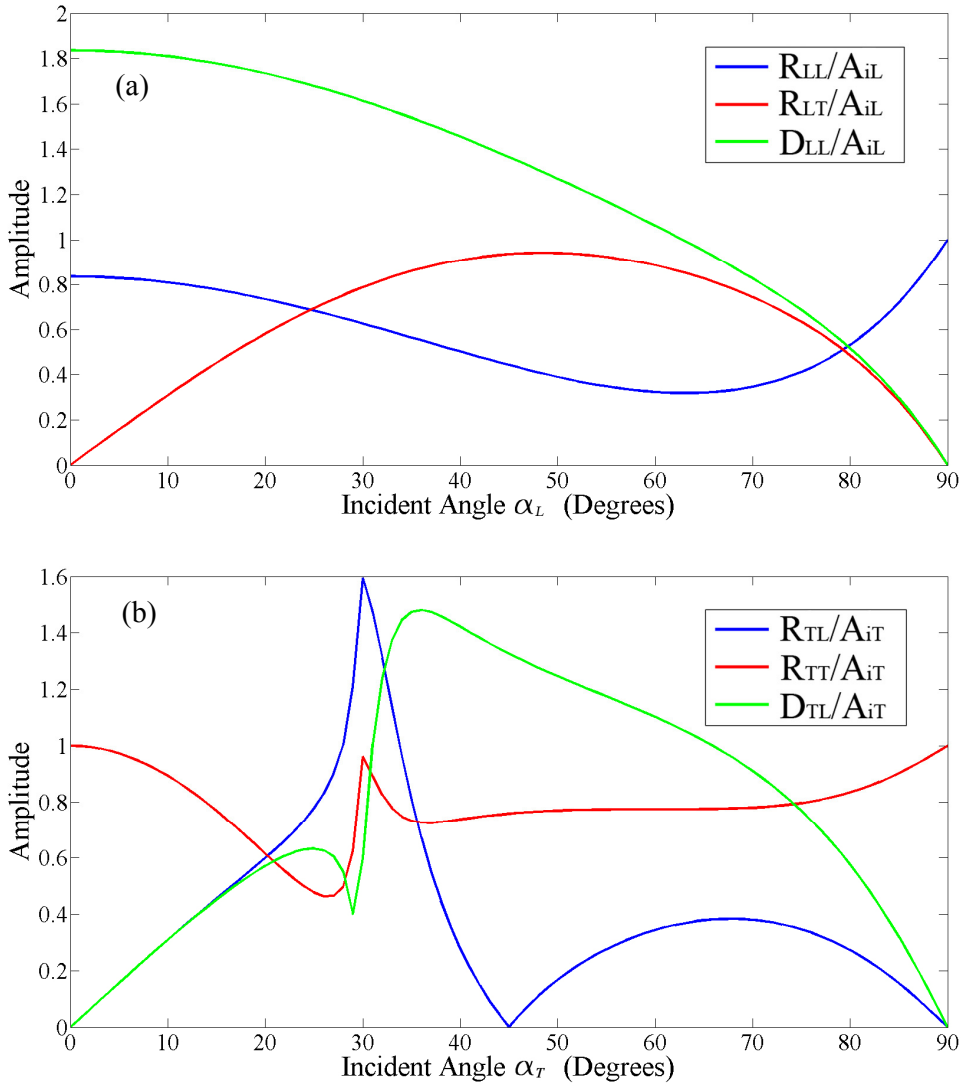

Fig. 5.9 Reflection and transmission coefficients for oblique incidence onto an aluminum-water interface: (a), longitudinal incidence; (b), transverse incidence.

5.3.3 Liquid-Solid Boundary Conditions

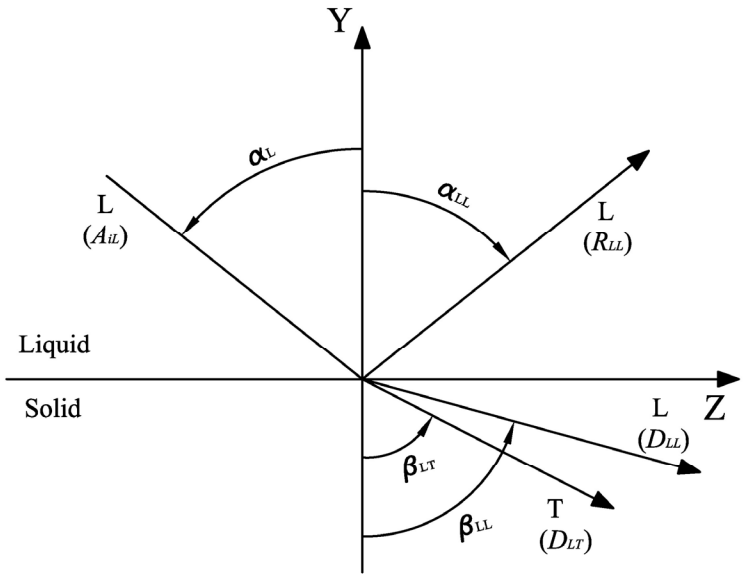

Fig. 5.10 Reflection and refraction at a liquid-solid media interface.

The reflection and refraction factor equations for liquid-solid boundary conditions (see Fig. 5.10) can be obtained as before. With liquids, there is only a longitudinal wave. The reflection and refraction equations become [Rose, 1999]:

$$\mathrm{N}\begin{bmatrix} R_{LL} \\ D_{LL} \\ D_{LT} \end{bmatrix} = b \tag{5.22}$$

where

$$\mathrm{N} = \begin{bmatrix} -\cos\alpha_{LL} & -\cos\beta_{LL} & \sin\beta_{LT} \\ -k_{L1}\lambda_1 & k_{L2}(\lambda_2 + 2\mu_2)\cos 2\beta_{LT} & -k_{T2}\mu_2 \sin 2\beta_{LT} \\ 0 & -k_{L2}\mu_2 \sin 2\beta_{LL} & -k_{T2}\mu_2 \cos 2\beta_{LT} \end{bmatrix} \tag{5.23}$$

and

$$b = \begin{bmatrix} -\cos\alpha_L \\ k_{L1}\lambda_1 \cos 2\alpha_L \\ 0 \end{bmatrix} \tag{5.24}$$

Consider now a sample result of oblique incidence reflection and transmission coefficients onto a water-aluminum interface in Fig. 5.11. The effect of the two critical angles is clear until the total reflection is achieved beyond 29°.

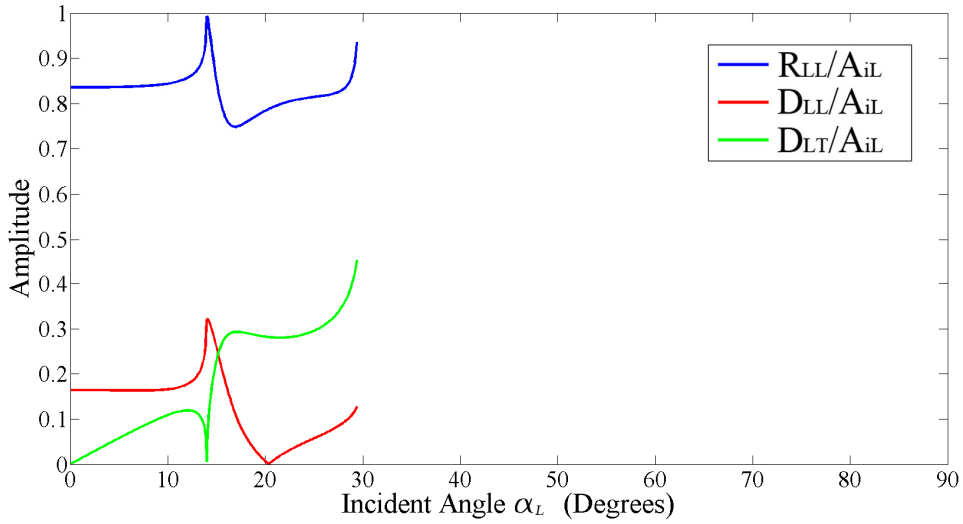

Fig. 5.11 Reflection and transmission coefficients for oblique incidence onto a water-aluminum interface.

5.4 Reflection and Transmission in Multi-layered Media

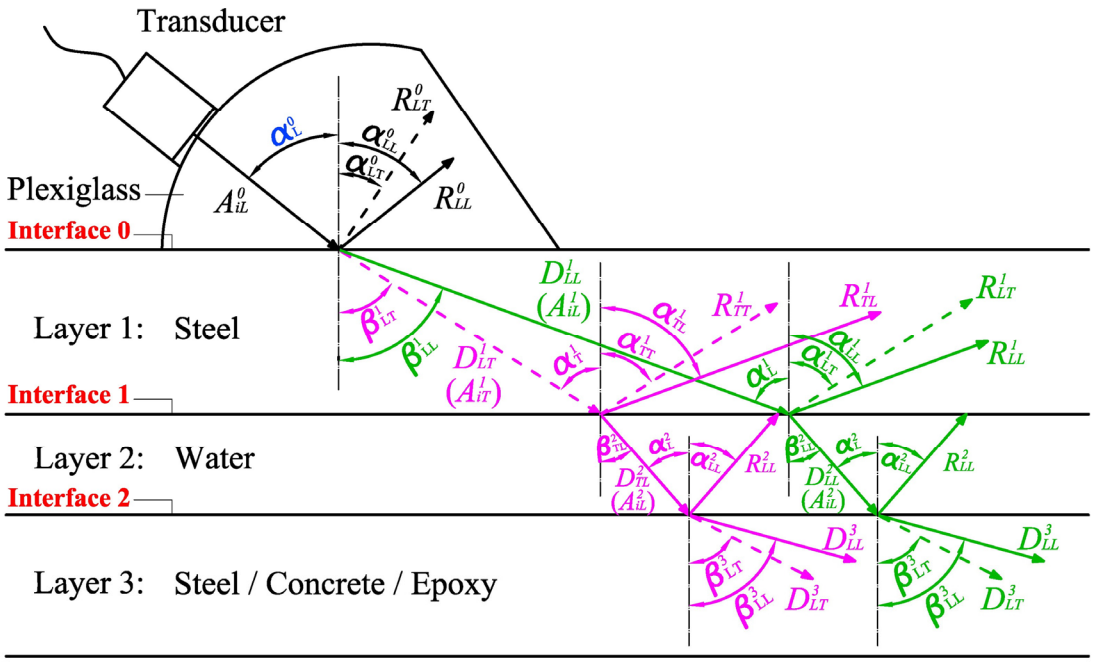

Fig. 5.12 Generation of Ultrasonic wave on a steel-water-bottom layered media, and its reflection and transmission on the interfaces.

Fig. 5.12 presents the reflection and transmission of an obliquely incident longitudinal wave in a three layered media, where the superscripts 0, 1, 2, or 3 denote the layer's number respectively. The purple arrows denote the transverse wave in the top steel plate, followed by the reflected and refracted waves on the interfaces 1 and 2, whereas the green arrows denote the longitudinal wave and its reflected and refracted waves. The reflection and transmission angles at each interface in the multi-layered media including a water layer can be calculated according to Snell's law. In the following graphs, the incident angle α_L^0 of the longitudinal wave in the angle-adjustable wedge made of plexiglass is taken as a variable of all the coefficient curves, for it is the only controllable angle in the experiment.

5.4.1 Interface of Steel-Water

Table 5.1 Material constants of the multi-layered media.

Material	C_L (m/s)	C_T (m/s)	ρ (kg/m^3)
Plexiglas	2680	1280	1200
Steel	5870	3140	7800
Water	1500	-	1000
Concrete	4000	2450	2400
Epoxy	2000	1000	1120

Figs. 5.13 (a) and (b) show the reflection and transmission coefficients on the steel-water interface (Interface 1 in Fig. 5.12), subjected to longitudinal and transverse waves in a steel plate, respectively, as a function of the incident angle α_L^0. The material constants of each layer are listed in Table 5.1. Now, we focus on the transmission coefficients of D_{LL}^2/A_{iL}^1 and D_{TL}^2/A_{iT}^1, since we are interested in how much energy can be transmitted through the steel-water interface into the water layer, which is directly related to the effect of the multi-reflection in water. In Fig. 5.13, we can find two critical angles of $\alpha_{c1} = 27.2°$ and $\alpha_{c2} = 58.6°$. When the incident angle $\alpha_L^0 > \alpha_{c1}$, then no propagating longitudinal wave exists in the steel plate

due to the total refraction of a longitudinal wave at Interface 0. It is also noted that the reflected longitudinal wave of R_{TL}^{1} becomes an inhomogeneous wave with amplitude decay vertically from the Interface 1 when $\alpha_L^0 > \alpha_{c1}$, and is not possible to be received by the transducer on the top surface. Similarly, for $\alpha_L^0 > \alpha_{c2}$, there is no propagating transverse wave in the steel layer. Thus no acoustic waves with the amplitude D_{LL}^{2} and D_{TL}^{2} exist in the water layer if $\alpha_L^0 > \alpha_{c1}$ and $\alpha_L^0 > \alpha_{c2}$, respectively, as shown in Fig. 5.13 (a) and (b). It is noticed that the amplitude of the transmitted wave from the transverse wave in steel is remarkable for $30^\circ < \alpha_L^0 < 50^\circ$, but the amplitude decreases quickly to zero for $\alpha_L^0 > 50°$. Also, for $0^\circ < \alpha_L^0 < 20^\circ$, the amplitude of the transmitted wave from the longitudinal wave is quite large. But in this range, both propagating longitudinal and transverse waves exist, which may bring a complicated received waveform.

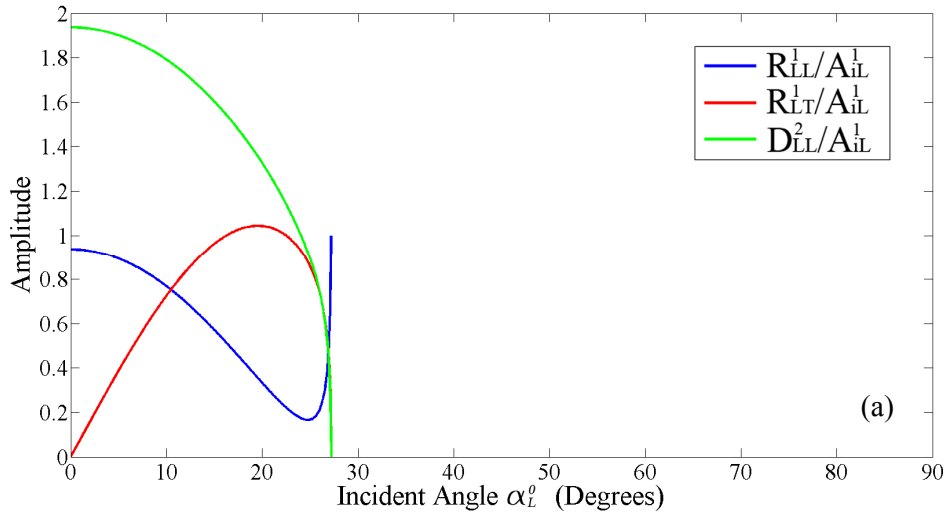

Fig. 5.13 Reflection and transmission coefficients on the steel-water interface (Interface 1 in Fig. 5.12) with incident angles 0° ~ 90°: (a) longitudinal incident wave in steel layer;

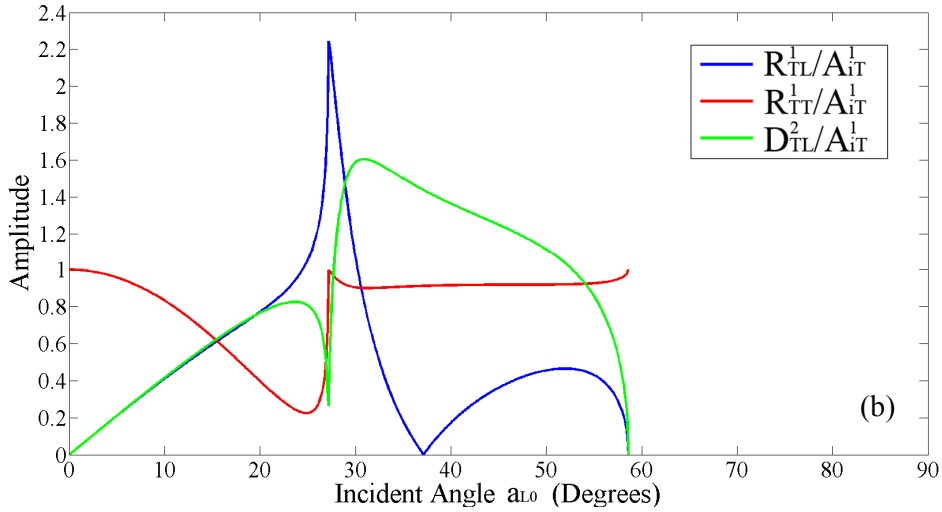

Fig. 5.13 Reflection and transmission coefficients on the steel-water interface (Interface 1 in Fig. 5.12) with incident angles 0° ~ 90°: (b) transverse incident wave in steel layer.

5.4.2 Interface of Water-Solid

Fig. 5.14 shows the reflection and transmission coefficients on the water-solid interface (Interface 2 in Fig. 5.12). The material of the bottom layer solid has three options: (a) steel, (b) concrete, and (c) epoxy. As to the steel plate strengthen method for RC structure, the water (rain water or moisture) can penetrate into the gap between steel and concrete, if epoxy is not used as an adhesive; or it can penetrate into the debonding interface between steel and epoxy when epoxy is used as an adhesive. Therefore, we need to consider the coefficients for reflection and transmission in these two cases. The configuration of steel-water-steel is just set here for the comparison with the previous two cases.

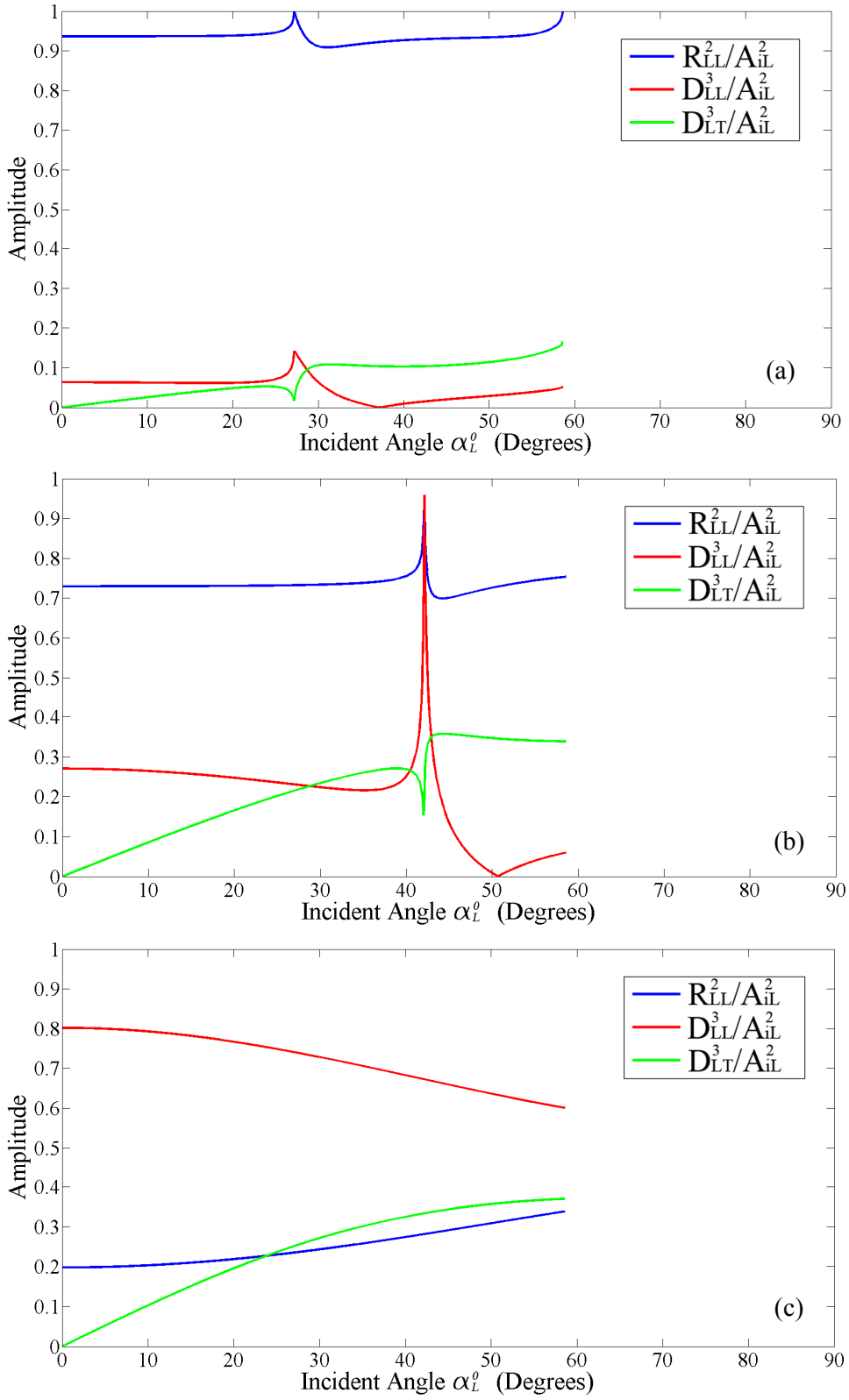

Fig. 5.14 Reflection and transmission coefficients on the water-solid interface (Interface 2 in Fig. 5.12) with incident angles 0°~90°: (a) steel, (b) concrete, (c) epoxy as the bottom solid.

In Fig. 5.14 (a), we can see that for a water-steel interface, the reflection coefficient R_{LL}^2/A_{iL}^2 is very close to 1 for $\alpha_L^0 < \alpha_{c2}$. Oppositely, the transmission coefficients D_{LL}^3/A_{iL}^2 and D_{LT}^3/A_{iL}^2 are very small. This means that once an ultrasonic wave is transmitted into a thin water layer between double steel plates, almost all energy of the wave is reflected back by steel plates and trapped as longitudinal waves in water, with few energy penetrating into the bottom steel plate. In the case of a water-concrete interface, the reflection coefficient is still much larger than transmission coefficients as seen in Fig. 5.14 (b), but compared to the water-steel case, more energy is transmitted into the bottom concrete. In the case of the water-epoxy interface, as seen in Fig. 5.14 (c), on the other hand, the amplitude of reflection coefficient R_{LL}^2/A_{iL}^2 is smaller than transmission coefficient D_{LL}^3/A_{iL}^2, which means more energy is absorbed by epoxy layer instead of being reflected.

The calculated reflection and transmission coefficients for various material combinations can be used to estimate the effect of multi-reflection approach which will be introduced in the following section, and many phenomena occurred in the experiment can also be explained by those coefficients.

5.5 Summary

The reflection and transmission in the multi-layered media has been discussed in this chapter through the figures of reflection coefficients versus incident angle changing. In the liquid-solid model, three different materials (steel, concrete, and epoxy) have been considered as the bottom solid layer, and extraordinarily good and relatively good reflection properties have been found in the cases of steel and concrete respectively. However, setting epoxy as the bottom layer will not largely reflect the energy back into the water layer, instead, absorbing it on quite a level. This theoretical result will influence the effect of the multi-reflection based detection in Chapter 7 somehow. The factor of critical angles will also give us the theoretical principle of the incident angle selection in the oblique incident ultrasonic wave testing in the following chapters.

CHAPTER 6

DETECTION OF WATER LAYER IN LAYERED MEDIA BASED ON MULTI-REFLECTION OF OBLIQUE INCIDENT ULTRASONIC WAVE

6.1 Introduction

In this chapter, a novel detection method based on multi-reflections of oblique incident ultrasonic waves in high frequency range (around 5MHz) is developed, which is operationally effective and visually resolvable for the existence of a thin water layer in multi-layered media [Shen and Hirose, 2016]. Experiments are conducted for multi-layered configurations with different water layer thicknesses (from 1mm to 10mm). From experimental results, not only the water layer's existence can be clearly distinguished, but also the water layer thickness can be estimated by comparing the measured time interval of reflected wave groups from received signals with the theoretical wave travelling time in the water layer. In the experiments, we also substitute different materials of steel, concrete, and epoxy as the bottom layer. It will be shown that different materials used as the bottom layer can affect the multi-reflection effect notably

and the corresponding received waveforms can be well explained by the calculated reflection coefficients in Chapter 5.

6.2 Multi-reflection Approach

When an incident wave is obliquely generated, and reflected and transmitted on a solid-liquid interface, some energy will penetrate as a longitudinal wave into the liquid layer. When the thickness of the liquid layer is thin, the longitudinal wave can be reflected and refracted several times in the liquid layer between two solid layers, as shown in Fig. 6.1. For simplicity, we consider the case of $\alpha_{c1} < \alpha_L^0 < \alpha_{c2}$, for which only transverse waves can propagate in Solid 1 layer as discussed in the previous section. In Fig. 6.1, different colors are employed to stand for reflected waves with different reflection cycles in the liquid layer. Black dashed line denotes the wave reflected only in the Solid 1 without any propagation in the liquid. To the receiver, this wave group propagating along the black route will be firstly received, so called "first arrival wave group". The blue, red and green lines represent the wave propagation routes with single, twice and triple reflections in the liquid layer, respectively. The total reflection times from the bottom interface depend on the reflection and transmission coefficients of different interfaces, and the distance between the transmitter and the receiver. Theoretically a longer distance can cause more reflected wave groups captured by the receiver, but the decay of signal will also become notable after a long way of propagation. Generally from the second reflection, the amplitudes of those reflected waves decrease distinctly, which will be shown in the later experiment part. It is noted that any down-going wave on Solid1-Liquid interface inside the plate will generate a new transmitted wave into the liquid, but for simplicity, those transmitted waves are not shown in Fig. 6.1 except the first one.

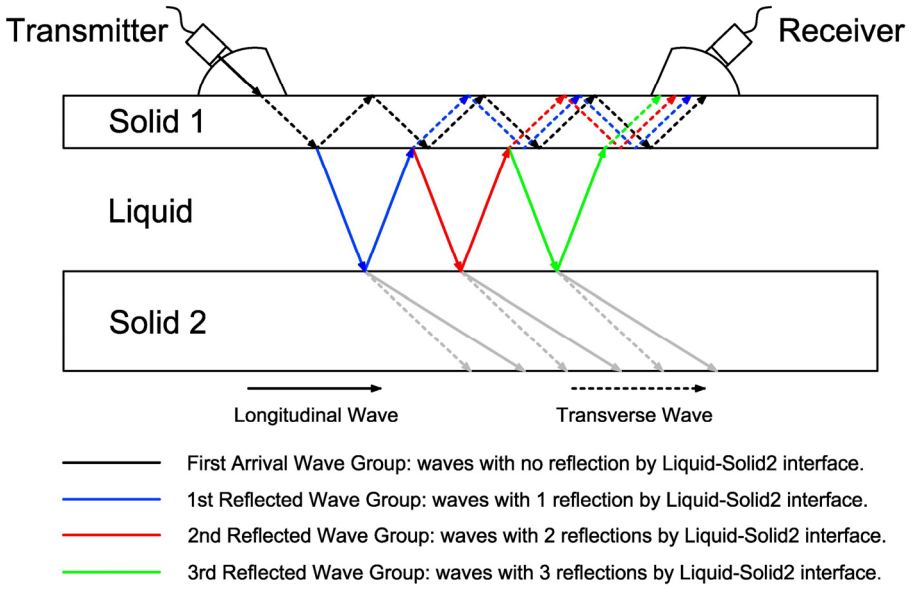

Fig. 6.1 Oblique incident ultrasonic multi-reflection approach to detect the thin liquid layer between solid layers.

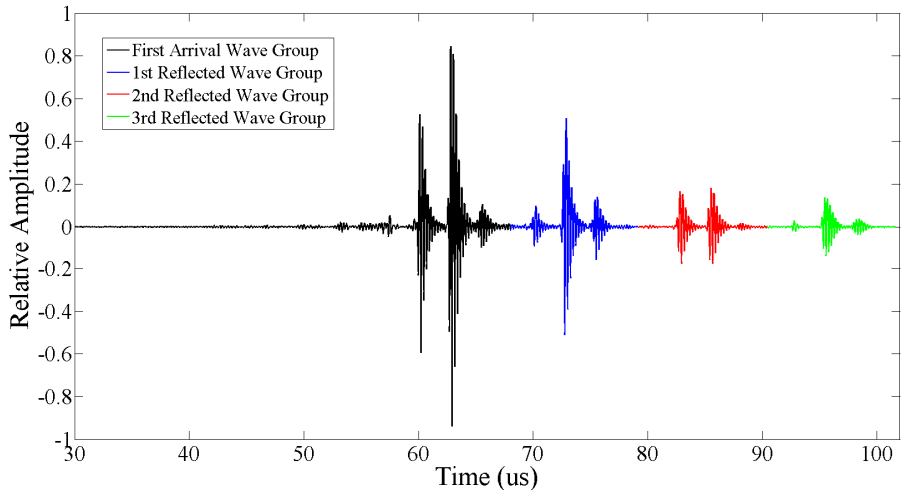

Fig. 6.2 Different wave groups are captured by receiver. The colors are corresponding to those in Fig. 6.1.

Since the velocity of longitudinal wave in liquid is normally much smaller than the transverse wave velocity in solid, the wave groups transmitted back into the solid plate after multiple reflections in the liquid layer (blue, red, and green routes in Fig. 6.1) will be received sequentially behind the first arrival wave group (black route in Fig. 6.1) with a certain time

interval. This time interval is related with the travel time of the longitudinal wave in the liquid layer, namely, the propagation length in liquid, which depends on the thickness of the liquid layer. Hence, if there is a liquid layer under the solid plate, the receiver can capture those wave groups as shown in Fig. 6.2. In Fig. 6.2, those wave groups are apart from each other with an almost constant time interval, representing each group's travel time in the liquid layer. Therefore, this phenomenon of multi-reflection can be used to detect the existence of water layer beneath a solid layer, judging by the received wave forms.

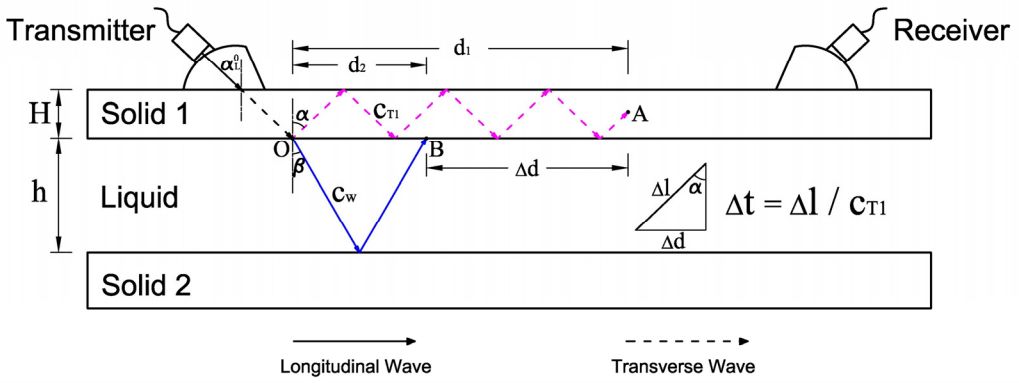

Fig. 6.3 Calculation of theoretical time interval of two adjacent wave groups.

In Fig. 6.3, the calculation method of the theoretical time interval between two adjacent wave groups is presented. Assuming the incident angle of $\alpha_{c1} < \alpha_L^0 < \alpha_{c2}$, where no propagating longitudinal wave exists in the steel plate as mentioned in the previous section, we only consider a transverse wave in the solid plate. We assume that at point O, a transverse wave reaches the Solid 1-Liquid interface, and is separated into the reflected wave in Solid 1 with velocity c_{T1} and the transmitted wave in the liquid with velocity c_w. After the one-cycle travel time of the longitudinal wave in the liquid layer, the wave in the liquid reaches the Liquid-Solid 1 interface again at point B, and the transverse wave in Solid 1 reaches point A far ahead due to the faster velocity in Solid 1. Their horizontal distance is marked as Δd in

Fig. 6.3, which is:

$$\Delta d = d_1 - d_2 = \frac{2h}{cos\,\beta}\left(\frac{c_{T1} \cdot sin\,\alpha}{c_w} - sin\,\beta\right) \tag{6.1}$$

where h is the liquid layer thickness, and α and β are the reflection angle in Solid 1 and refraction angle in Liquid respectively, which can be both determined by incident angle α_L^0 through Snell's law.

The longitudinal wave in the liquid can transmit into Solid 1 again after point B as transverse wave with velocity of c_{T1}, hence, the theoretical time interval of these two wave groups (purple and blue) is:

$$\Delta t = \Delta l / c_{T1} \tag{6.2}$$

where Δl is the distance between A and B on the direction of transverse wave propagation in Solid 1, namely,

$$\Delta l = \Delta d / sin\,\alpha \tag{6.3}$$

If we can measure the time interval of wave groups from the experiment, Δt_{exp}, and substitute the theoretical time interval Δt in Eq. (6.2), then we can estimate the liquid layer thickness from Eqs. (6.1)~(6.3) by:

$$h_{est} = \frac{\Delta t_{exp} \cdot cos\,\beta}{2\left(\frac{1}{c_w} - \frac{sin\,\beta}{c_{T1} \cdot sin\,\alpha}\right)} \tag{6.4}$$

From Eq. (6.4), we can see that for a certain incident angle, the estimated liquid layer thickness is only proportional to the experimental time interval, Δt_{exp}. Hence, the measurement of Δt_{exp} is significant for the liquid layer thickness estimation.

6.3 Ultrasonic Test

In order to experimentally apply the multi-reflection approach to detect the existence of

the water layer and estimate its thickness, a specimen of steel-water-solid (steel, concrete, and epoxy) configuration with variable water thickness is prepared as shown in Fig. 6.4, where a bottom solid is concrete, steel or epoxy. Two identical transducers with variable angle are positioned with distance of 10cm, one as a transmitter and another one as a receiver. In each test, the same angle is set for both transducers. Glycerine is pasted as a couplant between the wedge and steel plate. Meanwhile, for comparison, the same tests are also conducted for the steel-concrete and steel-epoxy-concrete perfectly bonded specimens.

In practical, the water layer thickness may not be constant due to several factors. In real structures, however, a debonding area is much larger than that we made in the specimen. We can treat the distance of 10cm between the transducer pair as a local spot on the relative large debonding area. In this paper, therefore, a constant water layer thickness is set in both theory and experiment. Also, assuming that the surfaces and interfaces are relative smooth, the effect of surface roughness due to corrosion is not considered here.

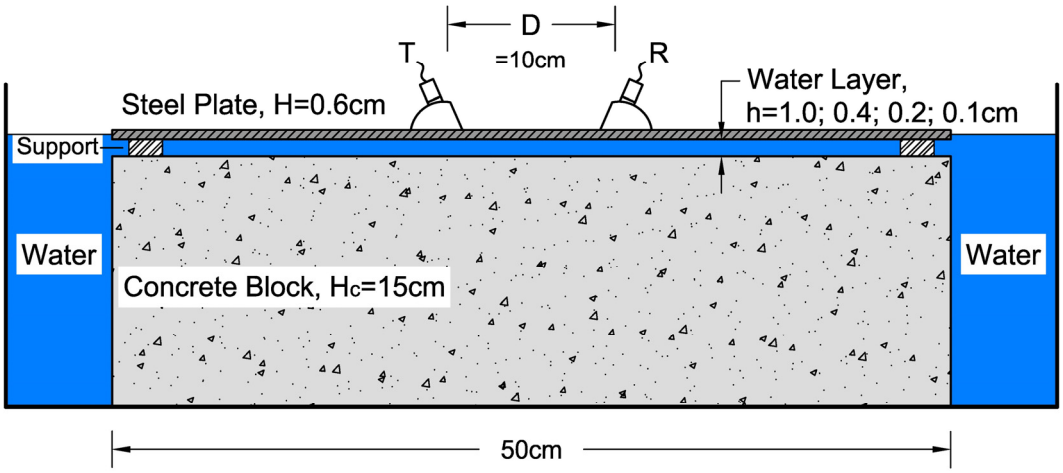

Fig. 6.4 Experimental setup for steel-water-concrete specimen.

Although reflection and transmission coefficients are not a function of frequency or wavenumber as seen in Eqs. (5.15)~(5.17), the frequency of the incident wave has significant effect on the practical usage of the multi-reflection approach. In a relatively low frequency

range (<1MHz), the width of a wave signal becomes wide, and several wave groups with different propagation routes are overlapped in the received waves, which makes it difficult to measure the arrival time of those wave groups. Hence, a relatively high frequency is recommended for the measurement. In this experiment, a pair of angle beam transducers with the central frequency of 5MHz and a one-wave square impulse wave of 5MHz are used in this study. Fig. 6.5 shows some details of the experiment setup.

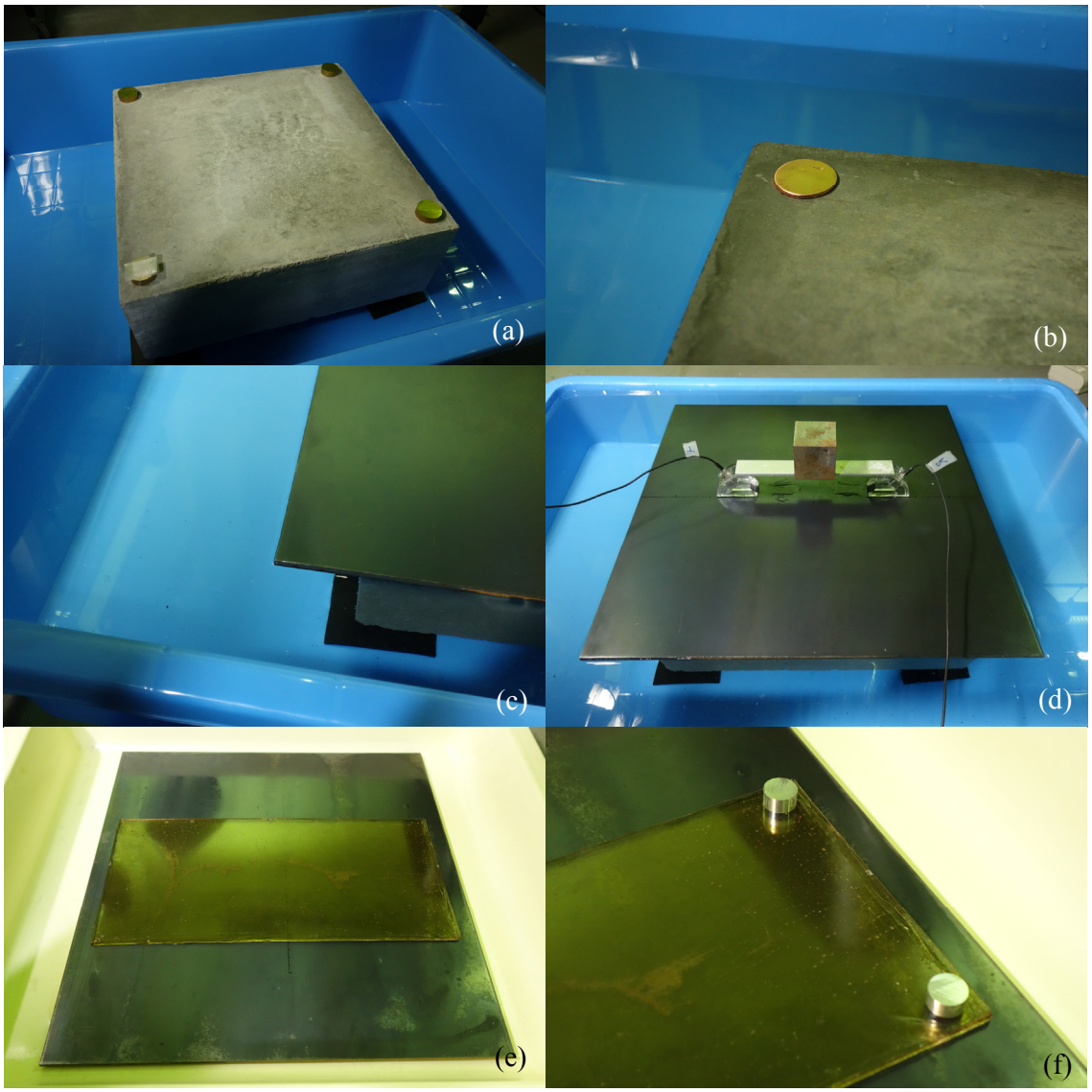

Fig. 6.5 Details of the experiment setup: (a), concrete block in a tank with 4 copper supports; (b), a 1mm thick copper support; (c), water been injected till half immerse the steel plate; (d), transducers on the steel plate; (e), epoxy plate as bottom layer; (f), aluminum supports.

6.4 Experimental Results and Discussion

6.4.1 Water Layer Detection

Fig. 6.6 clearly shows the difference between received waveforms for cases with and without a water layer. The blue lines are the waveforms obtained for the steel-concrete (Fig. 6.6 (a)) and steel-epoxy-concrete (Fig. 6.6 (b)) perfectly bonded specimens; while the red lines are the waveforms obtained for the corresponding configurations with a water layer. The thickness of the water layer is 10mm, the distance between two transducers is 10cm and the incident angle is $35°$.

In Fig. 6.6 and subsequent figures, it is seen that the waves are received as the form of wave group, among which the cases of "with water layer" contain multiple wave groups, as explained in Fig. 6.2. At the meantime, each group consists of several wavelets. The reason of the generation of wavelets in a group is as follows. When wave propagates in the steel plate, it can be reflected many times on the top and bottom surfaces of the plate. Within the finite contact area of the receiver's wedge with the steel plate, there are several reflection points, from which refracted waves are transmitted into the wedge [Lorenz and Lewandowski, 2012]. So several wavelets are observed in a wave group. A smaller incident angle can bring more reflection points within the finite contact area, and thus more wavelets can be seen in each group, as shown in Fig. 6.7.

From Fig. 6.6 we can see that the waveforms without a water layer perfectly overlap with the 1st wave group of waveforms with a water layer, which reveals that the propagation of the 1st wave group is not influenced by the water layer beneath. On the other hand, the subsequent reflected wave groups from the water layer differ entirely from the waveforms without a water layer, which can be used to distinguish the existence of a water layer effectively. Also we can find that the waveforms of steel-water-epoxy (Fig. 6.6 (b)) and steel-water-concrete (Fig. 6.6

(a)) show different behaviors on the number of reflected wave groups and the rate of signal decay. In the case of steel-water-epoxy, the amplitudes of reflected wave groups after the first one decrease fast, which is related with the relatively low reflection coefficient we obtained in Fig. 5.14 (c).

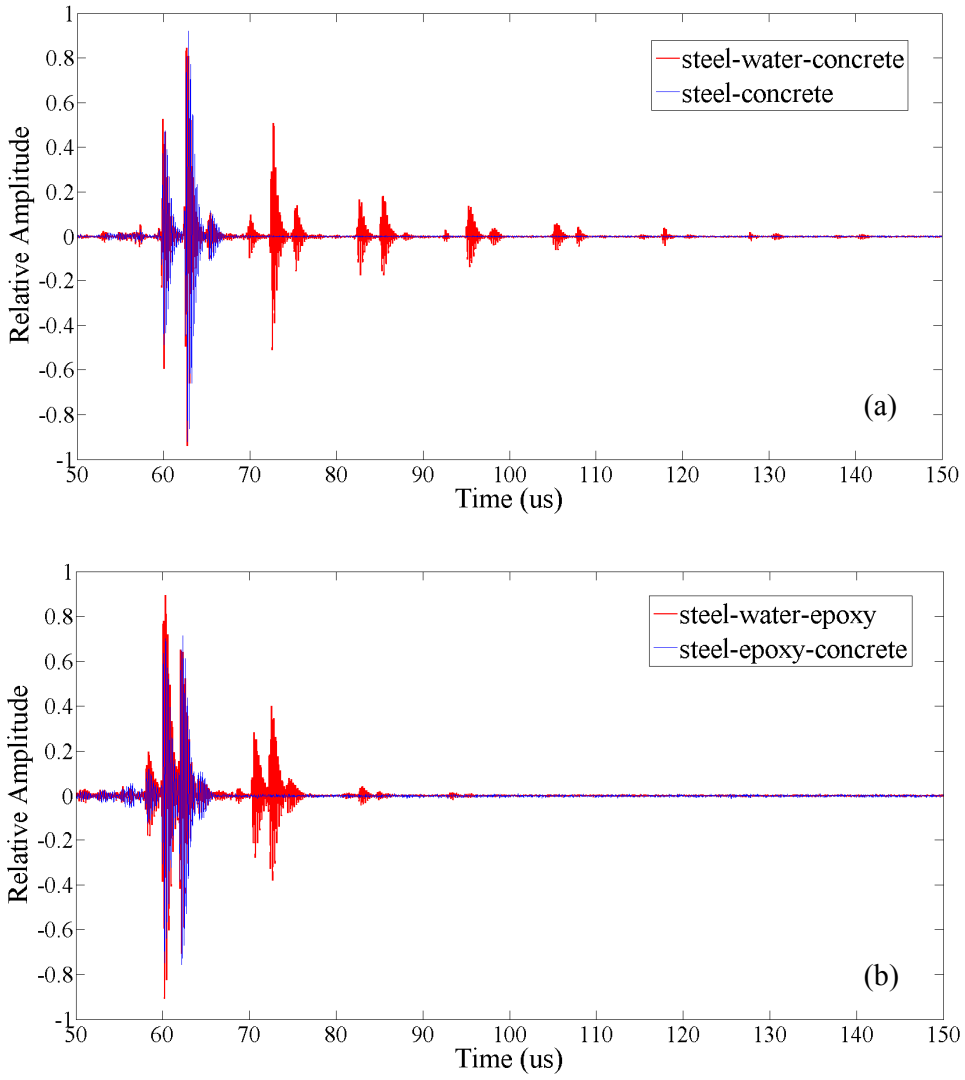

Fig. 6.6 Waveform comparison between configurations with water layer (10mm) and without water layer: (a) comparison of signals for steel-concrete bonded specimen and steel-water-concrete configuration; (b) comparison of signals for steel-epoxy-concrete bonded specimen and steel-water-epoxy configuration.

6.4.2 Incident Angles Selection

Then, we discuss the characteristics of waveforms with different incident angles. To distinctly demonstrate the effect of the incident angle, here, we use a layered model of steel-water-steel, for which multi-reflection effect can be seen clearly as a reference to the layered media of steel-water-concrete and steel-water-epoxy. Fig. 6.7 shows the received signals with different incident angles $\alpha_L^0 = 10°$ to $60°$ for the steel-water-steel configuration. The water layer thickness is 10mm and the distance between two transducers is 10 cm. For the cases of $\alpha_L^0 = 10°$ and $20°$, where the incident angle is smaller than the critical angle α_{c1}, both longitudinal and transverse components exist as body waves in the top steel plate, as seen in Fig. 5.13. Multi-reflected waves from the water layer can also be refracted into the top steel plate as longitudinal and transverse waves. Therefore, the waveforms are very complicated as shown in Fig. 6.7 (a) and (b). Thus for the case of $\alpha_L^0 < \alpha_{c1}$, reflected wave groups are not clearly demarcated and the time intervals between two adjacent wave groups are hard to be measured. For $\alpha_{c1} < \alpha_L^0 < \alpha_{c2}$, on the other hand, only transverse waves can propagate in the steel plate. As seen in Fig. 6.7 (c)~(e), therefore, the received waveforms are much simpler, and the first arrival wave group and the following reflected wave groups are clearly separated, especially for the cases of $\alpha_L^0 = 40°$, and $50°$. Thus, it is not difficult to measure the time intervals between wave groups. When the incident angle is close to the critical angle α_{c2}, say, $\alpha_L^0 = 50°$, the reflected wave groups show fast decay in amplitude, because of sudden drop of the value of D_{TL}^2 near α_{c2} as shown in Fig. 5.13 (b). For the case of $\alpha_{c2} < \alpha_L^0$, both longitudinal and transverse waves cannot propagate in the steel plate. The received wave is only a surface wave propagating along the surface, therefore in the case of $\alpha_L^0 = 60°$, received waves show small amplitudes. From the above discussion on the results shown in Fig. 6.7, it is concluded that the best incident angle range for the multi-reflection approach is $30°\sim50°$.

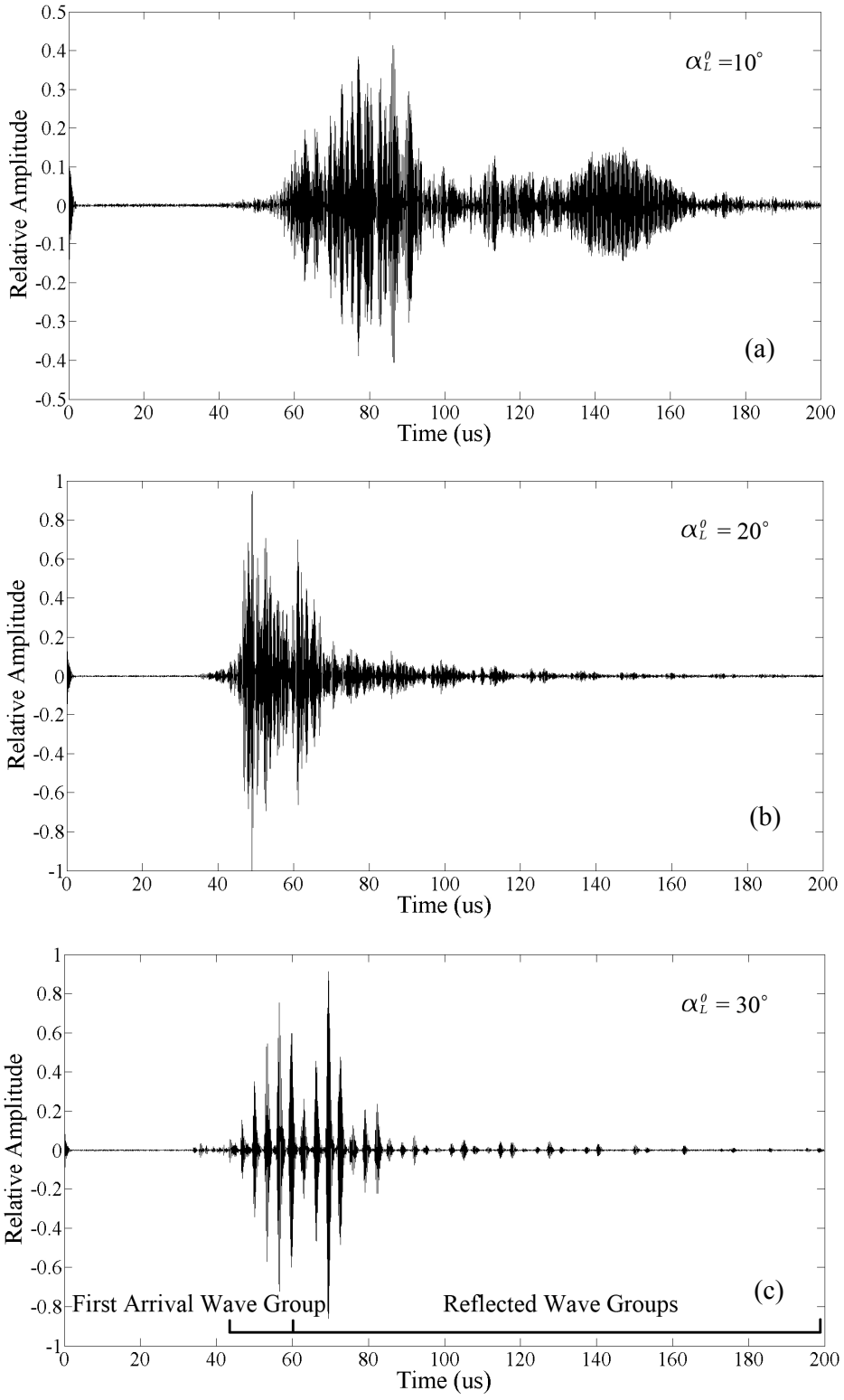

Fig. 6.7 Received waveforms for the steel-water-steel configuration with different incident angle α_L^0, h=10mm: (a), $\alpha_L^0 = 10°$; (b), $\alpha_L^0 = 20°$; (c), $\alpha_L^0 = 30°$.

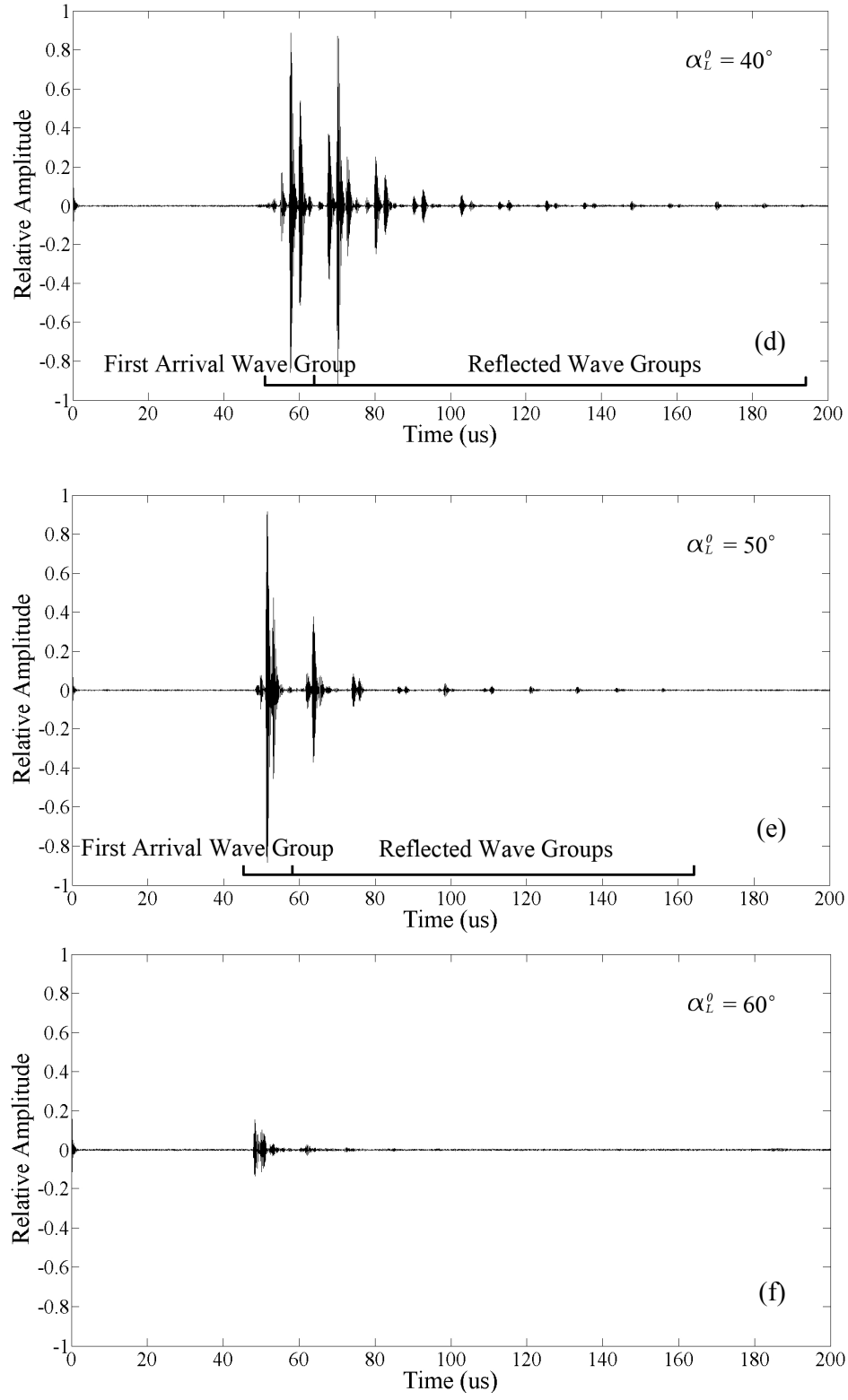

Fig. 6.7 Received waveforms for the steel-water-steel configuration with different incident angle α_L^0, h=10mm: (d), $\alpha_L^0 = 40°$; (e), $\alpha_L^0 = 50°$; (f), $\alpha_L^0 = 60°$.

6.4.3 Effect of Water Layer Thickness

Next we investigate how the water layer thickness affect the received waveform, also the effect of bottom materials on received waves is discussed. Three different materials of steel, concrete and epoxy are used as a bottom layer. The thickness of the water layer is adjusted by changing the height of the support. Fig. 6.8 shows waveforms for steel-water-steel configuration when the water layer thickness is (a) 10mm, (b) 4mm, (c) 2mm, and (d) 1mm. The distance between two transducers is 10cm and the incident angle is $35°$. In all cases, compared with no water cases (blue line), the reflected wave groups of water cases (red line) are clearly seen and distinguishable. For relatively large water layer thickness of 10mm (Fig. 6.8 (a)), the reflected wave groups are apart each other with the large time interval (Δt), which can be measured easily by finding the corresponding peaks between two adjacent wave groups. In the reflected wave groups, we can always find the corresponding peaks with those in the wave group for no water configuration. For relatively small water layer thickness of 4mm (Fig. 6.8 (b)), the reflected wave groups are compressed with shorter time intervals. For even smaller thicknesses of 2mm (Fig. 6.8 (c)) and 1mm (Fig. 6.8 (d)), the first arrival wave group and the first reflected wave group are so close, mixing with each other. This is because the water layer is so thin that the travel time of waves in water is too short to separate the first arrival and reflected wave groups apart. Thus, in principle, the multi-reflection approach utilizes the waveforms obtained only for the configuration with water, in which the reflected wave groups are separately seen from the first arrival wave group. For a case with thin water layer thickness (e.g. 2mm and 1mm), however, it may be difficult to separate the reflected wave groups from the first arrival wave group. In such a case, we recommend that the waveform for the case with no water layer is used as a reference to identify which wave packet belongs to which wave group.

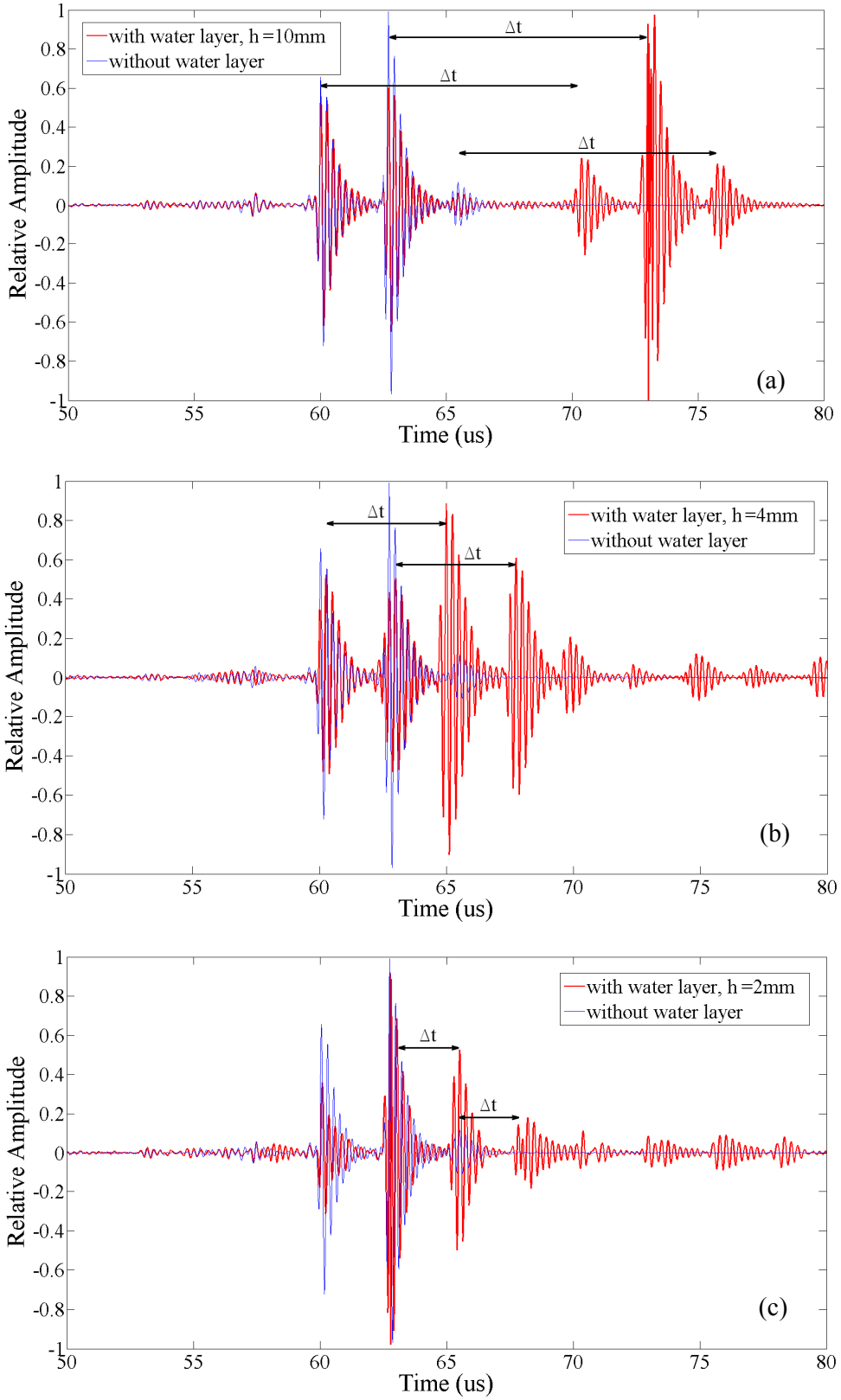

Fig. 6.8 Received waveforms on steel-water-steel configuration with water layer thickness of: (a) 10mm, (b) 4mm, and (c) 2mm. The time intervals of adjacent wave groups are marked.

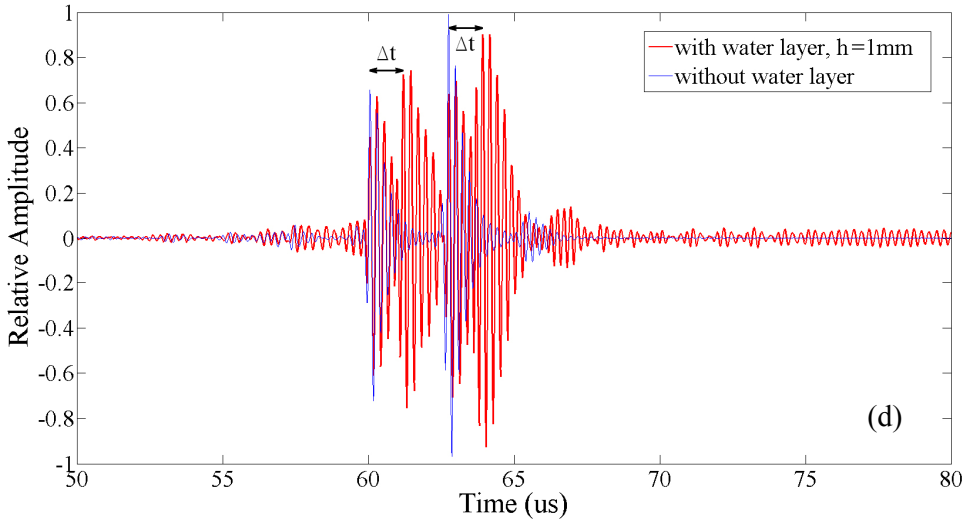

Fig. 6.8 Received waveforms on steel-water-steel configuration with water layer thickness of: (d) 1mm. The time intervals (Δt) of adjacent wave groups are marked.

Fig. 6.9 shows waveforms on steel-water-concrete configuration when the water layer thickness is 10mm (a), 4mm (b), 2mm (c), and 1mm (d). The distance between two transducers is 10cm and the incident angle is 35°. In all these cases, the differences between waveforms with and without water cases are significant. The multi-reflection effect is clear for the time interval measurement between wave groups. The only difference between steel-water-steel case and steel-water-concrete case is the decay rate of the amplitude of reflected wave groups, especially when the water layer thickness is relatively small as 2mm (Fig. 6.9 (c)) and 1mm (Fig. 6.9 (d)). In Fig. 6.9 (c), only one reflected wave group can be distinguished when the bottom layer is concrete, while in Fig. 6.8 (c), several reflected wave groups can be received. In another word, when the water layer thickness is very thin, the reflection effect in steel-water-concrete configuration is weaker than in steel-water-steel one. This phenomena can be explained by taking account of the reflection coefficients for different bottom materials shown in Fig. 5.14.

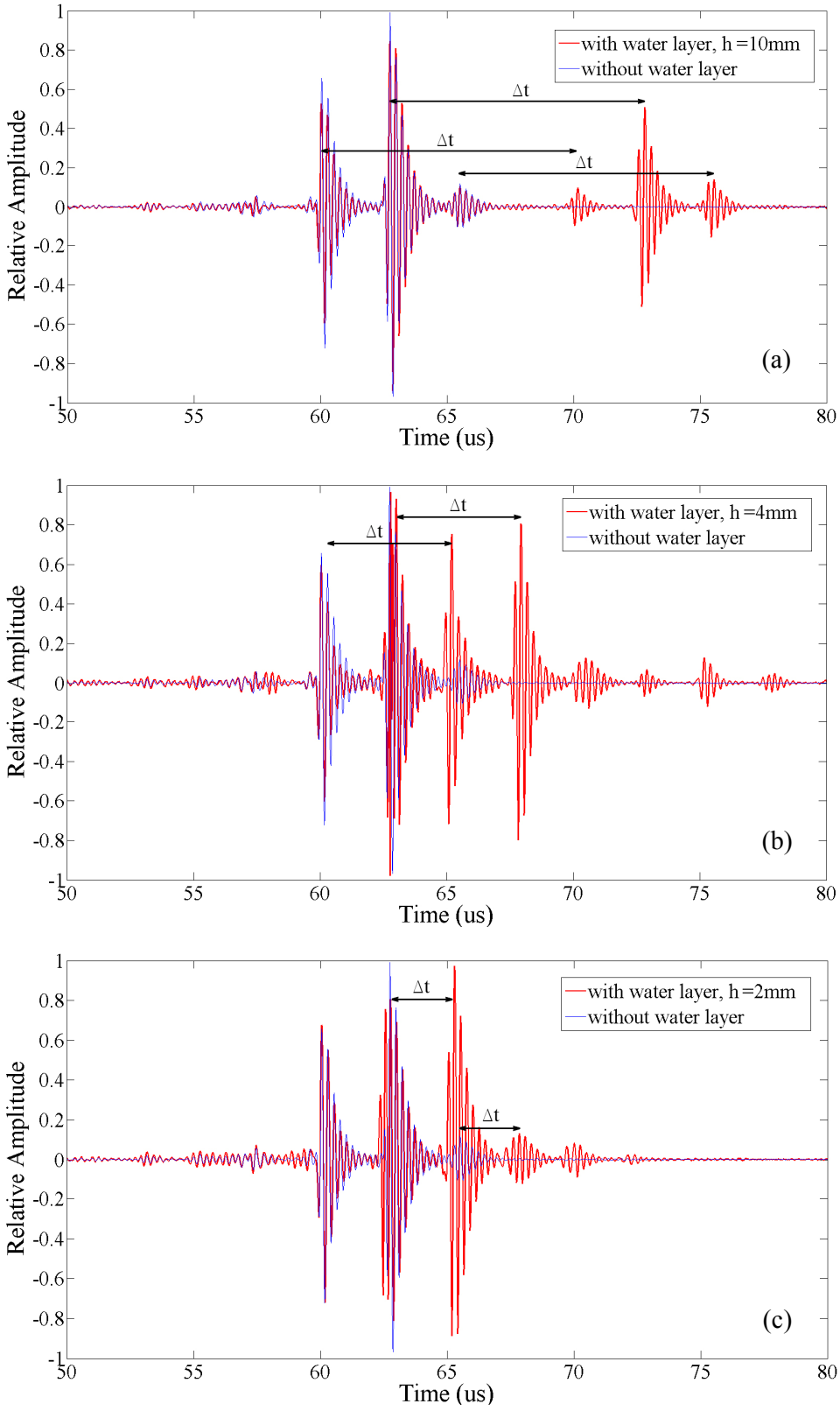

Fig. 6.9 Received waveforms on steel-water-concrete configuration with water layer thickness of: (a) 10mm, (b) 4mm, and (c) 2mm.

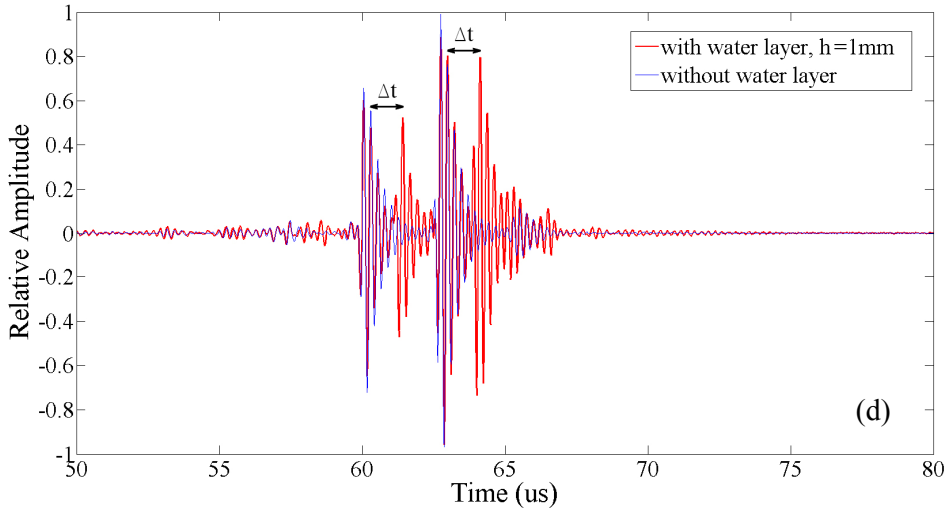

Fig. 6.9 Received waveforms on steel-water-concrete configuration with water layer thickness of: (d) 1mm.

Fig. 6.10 presents waveforms obtained for the steel-water-epoxy configuration. When the thickness is relatively large such as 10mm (Fig. 6.10 (a)) and 4mm (Fig. 6.10 (b)), the reflected wave groups are remarkably separated. When the thickness becomes small as 2mm (Fig. 6.10 (c)), however, the amplitudes of the reflected wave groups decrease. In Fig. 5.14 (c), it is found that the reflection coefficient on water-epoxy interface is relatively small compared with the other two cases. Therefore it can be said that the experiment validates the theoretical results well. For very thin water layer, e.g. $h = 1mm$ and $D = 10cm$ in Fig. 6.10 (d), to measure the time interval is difficult. In that case, employing a larger distance between transducers can help to obtain clearer reflected wave groups, as shown in Fig. 6.10 (e), where $D = 20cm$.

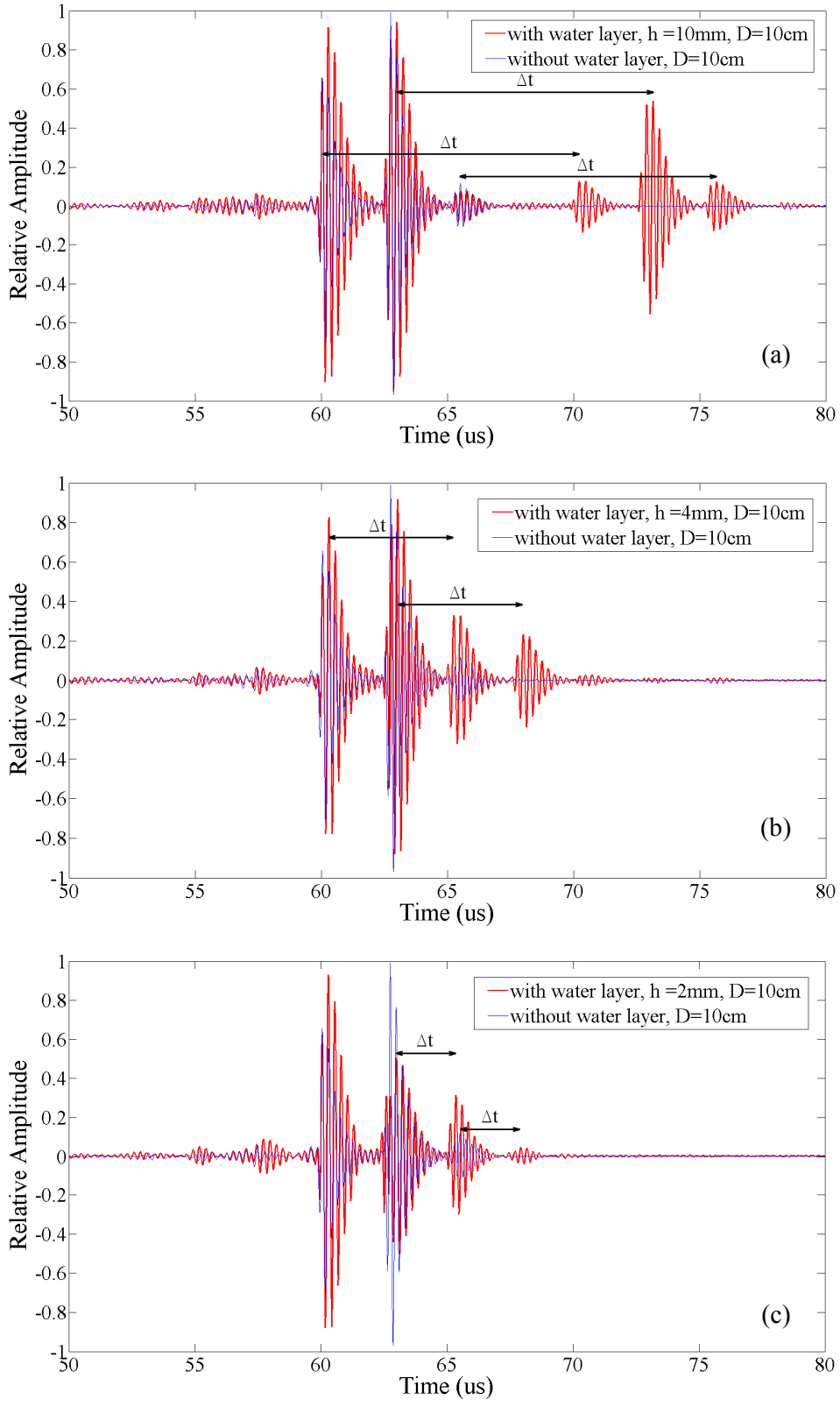

Fig. 6.10 Received waveforms on steel-water-epoxy configuration: (a) h=10mm, D=10cm, (b) h=4mm, D=10cm, and (c) h=2mm, D=10cm.

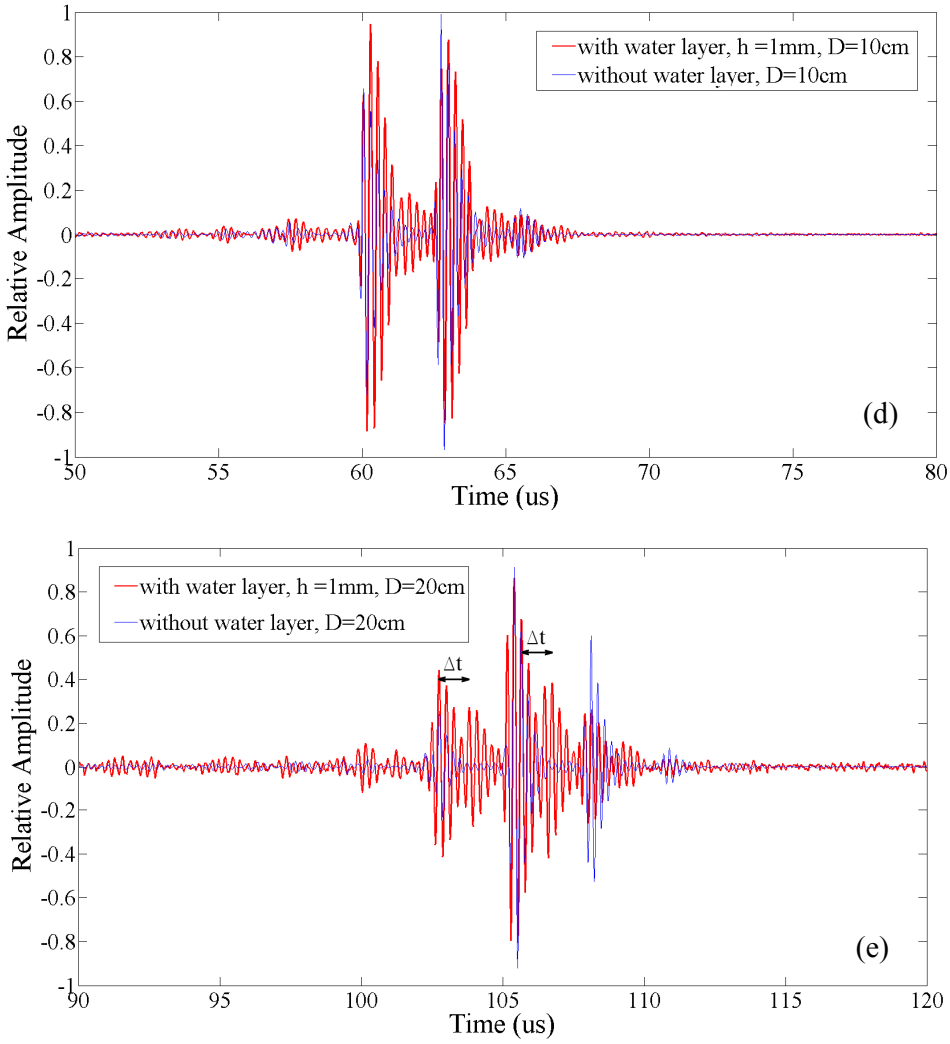

Fig. 6.10 Received waveforms on steel-water-epoxy configuration:
(d) h=1mm, D=10cm, and (e) h=1mm, D=20cm.

From the waveforms of these three configurations, we found that no matter how thick the water layer is, the 1st reflected wave group often shows relatively large amplitudes, corresponding to the distinct peaks with the first arrival wave group, which are very useful for time interval measurement. The following estimation of water layer thickness generally relies on the measurement of the 1st reflected wave groups.

6.5 Water Layer Thickness Estimation

From received waveforms of multi-layered media with a water layer, the time intervals of reflected wave groups can be measured. Table 6.1 lists the calculated and measured time

intervals of different configurations and water layer thicknesses. Incident angles from $30°$ to $50°$ are employed. The column of error is the difference ratio between each calculated Δt and measured Δt pairs. Then according to Eq. (6.4), the thickness of water layer in the multi-layered media can be estimated applying different incident angles.

Fig. 6.11 shows the estimated water layer thicknesses and the corresponding errors of different configurations (steel-water-steel; steel-water-concrete; steel-water-epoxy). In all the cases of water layer thickness of 10mm (Fig. 6.11 (a)), 4mm (Fig. 6.11 (b)), 2mm (Fig. 6.11 (c)), and 1mm (Fig. 6.11 (d)), estimation errors ($(h_{est} - h_{real})/h_{real}$) are generally less than 10%, which are acceptable in engineering concern. When the water layer thickness is relatively large, e.g. 10mm for any layer configurations and incident angles, the errors are stable. For relatively small thicknesses (4mm, 2mm, and 1mm), errors are much influenced by incident angles, with generally small values between $40°$ and $50°$. One reason of the error is the contact area of the receiver, which is not a single point as in theoretical consideration. Because of the noticeable bottom size of the transducers compared to the wave propagation distance between them, those wave groups are not received by a transducer at the same point, which may cause error in measured time interval. The measurement error can also be from the complicated waveform of the wave groups, each containing several wavelets, caused by the multiple reflections and transmissions on receiver's wedge-plate contact area. The other factor for the error is the positioning of the receiver. When the top steel plate is thick (6mm in this study), the horizontal distance of one reflection cycle in the steel plate (see Fig. 6.3) becomes large. It is, therefore, important to set the receiver correctly to catch the obliquely propagated wave properly.

From Fig. 6.11, it is concluded that it is practical to use calculated and measured time intervals of reflected wave groups in estimation of water layer thickness between two solid

layers.

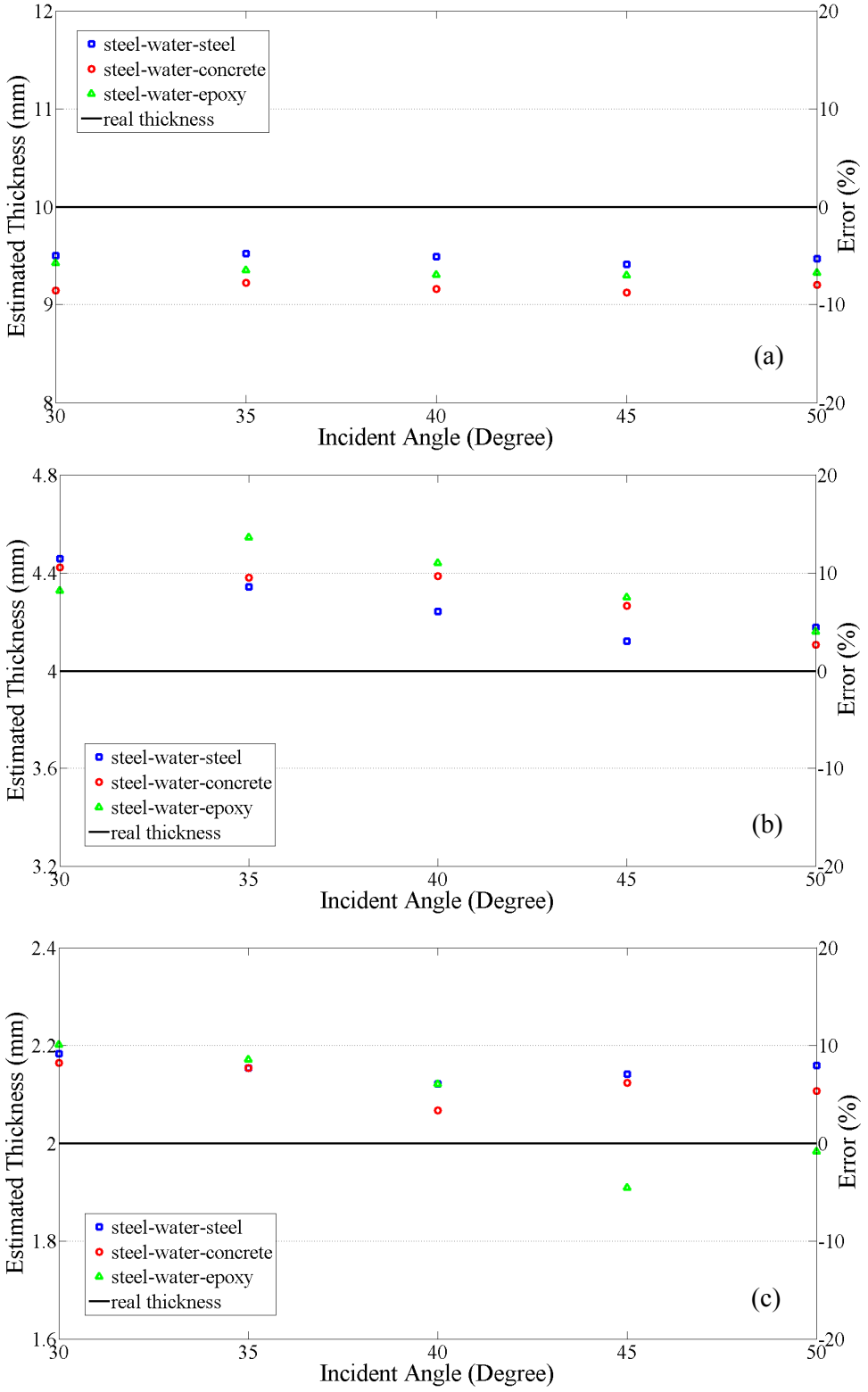

Fig. 6.11 Results of water layer thickness estimation of different configurations and different incident angles with water layer thickness of: (a) 10mm, (b) 4mm, and (c) 2mm.

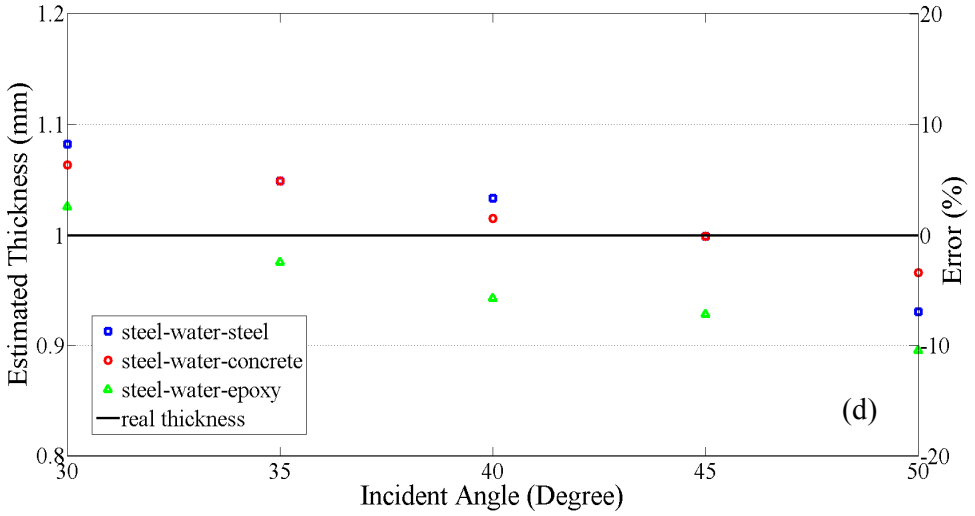

Fig. 6.11 Results of water layer thickness estimation of different configurations and different incident angles with water layer thickness of: (d) 1mm.

Table 6.1 Calculated and measured time intervals of reflected wave groups.

Steel-Water-Steel, h=10mm			
Incident Angle (deg.)	Calculated Δt (sec.)	Measured Δt (sec.)	Error
30	1.07E-05	1.02E-05	5.03%
35	1.09E-05	1.03E-05	4.84%
40	1.10E-05	1.05E-05	5.16%
45	1.12E-05	1.05E-05	5.94%
50	1.14E-05	1.08E-05	5.36%

Steel-Water-Steel, h=4mm			
Incident Angle (deg.)	Calculated Δt (sec.)	Measured Δt (sec.)	Error
30	4.29E-06	4.78E-06	11.49%
35	4.35E-06	4.72E-06	8.60%
40	4.41E-06	4.68E-06	6.08%
45	4.48E-06	4.62E-06	3.07%
50	4.56E-06	4.76E-06	4.47%

Steel-Water-Steel, h=2mm			
Incident Angle (deg.)	Calculated Δt (sec.)	Measured Δt (sec.)	Error
30	2.14E-06	2.34E-06	9.15%
35	2.17E-06	2.34E-06	7.68%
40	2.21E-06	2.34E-06	6.08%
45	2.24E-06	2.40E-06	7.09%
50	2.28E-06	2.46E-06	7.98%

Steel-Water-Steel, h=1mm			
Incident Angle (deg.)	Calculated Δt (sec.)	Measured Δt (sec.)	Error
30	1.07E-06	1.16E-06	8.22%
35	1.09E-06	1.14E-06	4.92%
40	1.10E-06	1.14E-06	3.36%
45	1.12E-06	1.12E-06	0.05%
50	1.14E-06	1.06E-06	6.94%

Steel-Water-Concrete, h=10mm			
Incident Angle (deg.)	Calculated Δt (sec.)	Measured Δt (sec.)	Error
30	1.07E-05	9.80E-06	8.57%
35	1.09E-05	1.00E-05	7.78%
40	1.10E-05	1.01E-05	8.42%
45	1.12E-05	1.02E-05	8.80%
50	1.14E-05	1.05E-05	8.00%

Steel-Water-Concrete, h=4mm			
Incident Angle (deg.)	Calculated Δt (sec.)	Measured Δt (sec.)	Error
30	4.29E-06	4.74E-06	10.55%
35	4.35E-06	4.76E-06	9.52%
40	4.41E-06	4.84E-06	9.71%
45	4.48E-06	4.78E-06	6.64%
50	4.56E-06	4.68E-06	2.72%

Steel-Water-Concrete, h=2mm			
Incident Angle (deg.)	Calculated Δt (sec.)	Measured Δt (sec.)	Error
30	2.14E-06	2.32E-06	8.22%
35	2.17E-06	2.34E-06	7.68%
40	2.21E-06	2.28E-06	3.36%
45	2.24E-06	2.38E-06	6.20%
50	2.28E-06	2.40E-06	5.35%

Steel-Water-Concrete, h=1mm			
Incident Angle (deg.)	Calculated Δt (sec.)	Measured Δt (sec.)	Error
30	1.07E-06	1.14E-06	6.35%
35	1.09E-06	1.14E-06	4.92%
40	1.10E-06	1.12E-06	1.55%
45	1.12E-06	1.12E-06	0.05%
50	1.14E-06	1.10E-06	3.43%

6.6 Summary

The multi-reflection method is very sensitive and effective to detect the existence of water layer in multi-layered media. The theory of reflection and transmission of oblique incidence in multi-layered media (liquid layer contained) and the coefficients can help to explain many phenomenon in the experiment, including effect of incident angle, effect of different bottom layer material, and time interval of reflected waves. The thickness of the water layer can be estimated through comparison of the measured time interval of reflected waves and the calculated wave travel time in water layer of different thicknesses. The estimation's accuracy is acceptable for engineering concern, and the error may come from the choice of receiver's position, the contacted area of the transducers, and the multiple reflections and transmission in wedge-plate contact area. This detection approach based on multi-reflection can be easily applied into the practical examination of water penetration in steel plate strengthened RC structures.

CHAPTER 7

IDENTIFICATION OF REGION OF WATER LAYER IN MULTI-LAYERED MEDIA

7.1 Introduction

In Chapter 6, we have conducted the oblique incident ultrasonic testing on various multi-layered media with relative ideal configuration setting, in order to prove the existence of water layer under the steel plate and to estimate its thickness. However, in the practical work, not only the water layer's existence and thickness need to be confirmed, but also the region of the invaded water beneath the steel plate needs to be discovered. The identification of the region of water layer can give a guidance about the exact location and the scale of the retrofitting or replacement work. In this chapter, steel-epoxy-concrete and steel-concrete multi-layered specimens with reserved damages (debonding, delamination, and gap) are casted. Then water can be injected through small holes on the steel plate to generate a liquid layer inside. The same technique of oblique incident ultrasonic testing based on multi-reflection will be applied to detect the water layer beneath and to identify the boundary of this water layer. Although in

reality, this invaded liquid layer could be quite large and more randomly distributed, we believe that the same detection method that we used on the specimen can be applied in the real case too, for the principle is not restricted to the size of the objects.

7.2 Procedures for Identification of Region of Water Layer

For a relative large debonding area where water could invade into, to detect its boundary using the method we proposed in Chapter 6 is what we concerning in this chapter. In reality, the boundary of this area could be pure randomly distributed and broadly extended. However, we can divide the detection area by relative smaller zones as shown in Fig. 7.1. After the detection on all these zones are completed, we can obtain an entire identification of the water invasion area. For the detection of each zone, we can have several steps to estimate the boundary of the debonding and water invaded area.

Step 1: Sparse detection to have a rough boundary. As presented in Fig. 7.1, set transducer pair (transmitter and receiver) on positions sparsely with relative large distances. If the waveforms received have the property of healthily bonded layered media, in another word, no reflected signal from the liquid layer, then, those positions can be marked with green color, as healthily bonded area. Oppositely, if the waveforms received contain the reflected components due to the liquid layer beneath, then those positions can be marked with red color, as water invasion area. After obtaining the markings, we can draw the middle points of each pair and connect them with dashed line, as the roughly estimated boundary as shown in Fig.7.1. In this step, the selection of detection positions can be relatively sparse, since the target of this step is to globally distinguish the areas of healthily bonded and water layer contained.

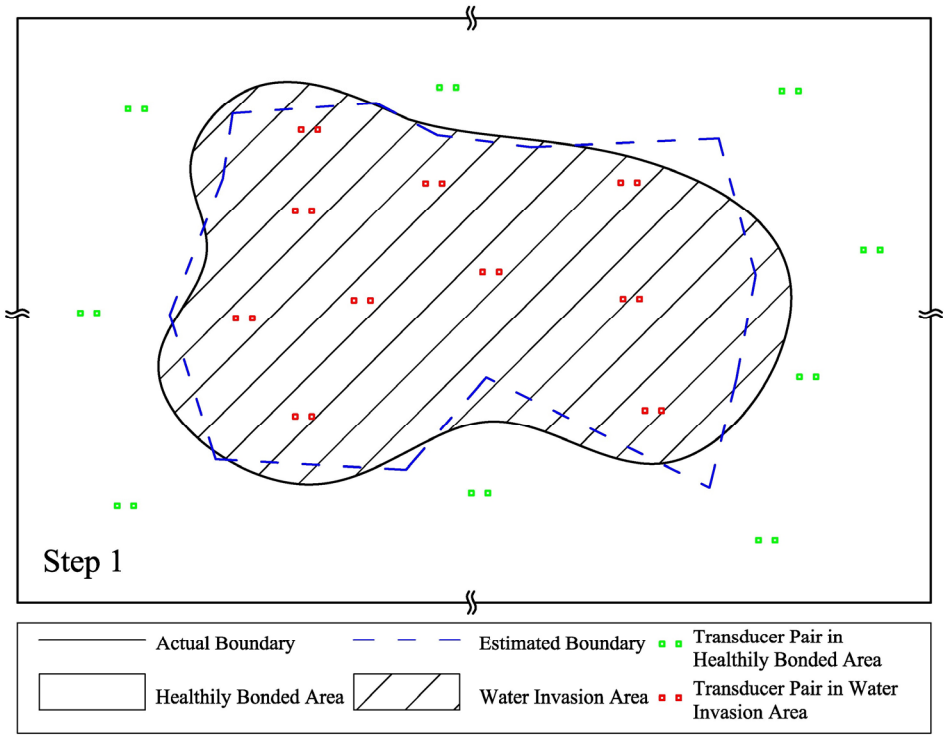

Fig. 7.1 Identification of region of water layer: step 1, sparse detection, rough boundary.

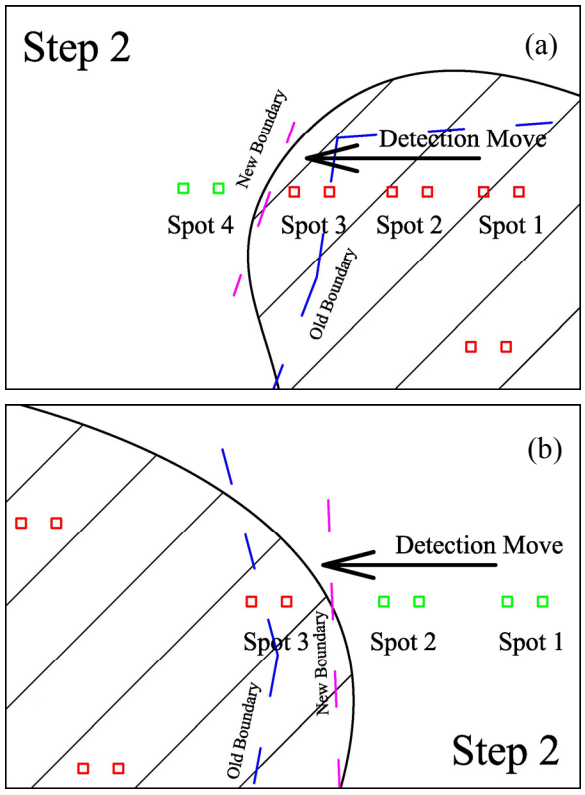

Fig. 7.2 Identification of region of water layer: step 2, detection move, renew boundary.
(a), from the water invasion area to the healthily bonded area;
(b), from the healthily bonded area to the water invasion area.

Step 2: Detection move; renew the boundary. After we obtain the rough boundary, we need to refine the boundary with more detection positions near that boundary. The refine or renew work can be progressed along two paths: from the water invasion area to the healthily bonded area (Fig. 7.2 (a)) or oppositely (Fig. 7.2 (b)). The principle of this progress is to move the transducer pair gradually with short space interval with signal receiving and comparing in real time. As long as the received waveform changes its property (reflected components appear or disappear), then the new boundary can be redrawn on the middle point of the current detection position and the previous one. Through this much finer detection around the rough boundary, we can correct the boundary precisely, to meet the engineering requirement.

Step 3: Obtain the final estimated boundary. When all the finer detections have been completed with renewed boundary sections, we can connect all the sections to have the final estimated boundary, as shown in Fig. 7.3. The accuracy of this estimated boundary depends on the number of the fine detection positions around the boundary and the complexity of the water invasion area itself. In some practical work, only the general region of the water invasion area is needed to know, for the following retrofitting work will not be applied so locally. In that case, the fine detection points can be less. However, benefiting from the easy comparison through waveforms directly, a much finer identification will not be so time consuming either.

This identification is based on the fact that the detection method proposed in Chapter 6 can distinguish the areas inside the boundary from outside the boundary, especially in the area close to the actual boundary. The following sections will discuss about this precondition.

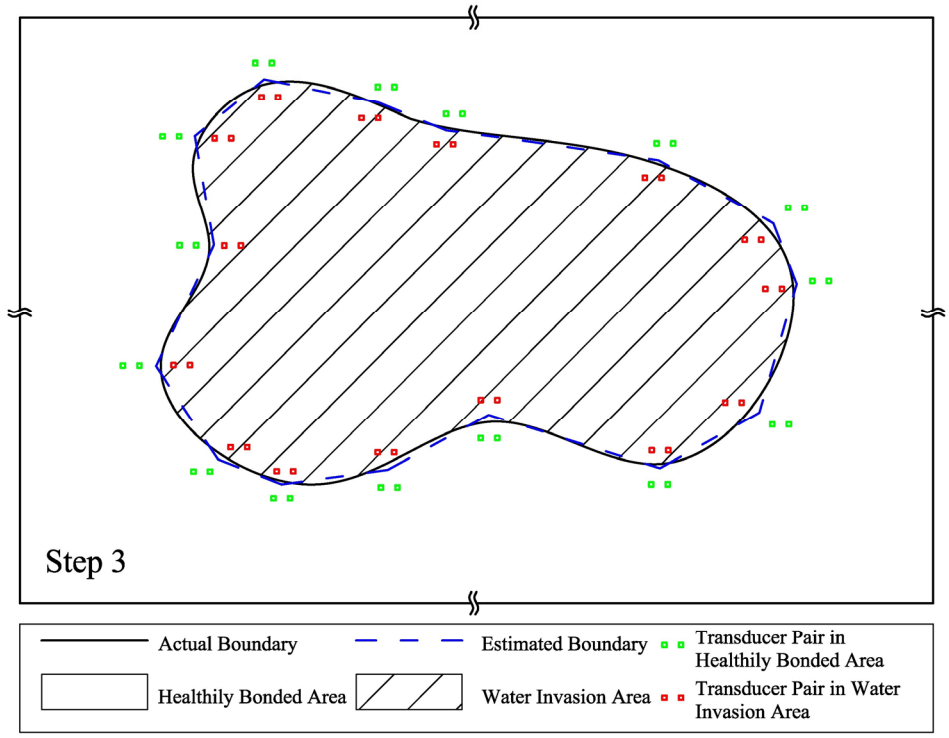

Fig. 7.3 Identification of region of water layer: step 3, obtain final estimated boundary.

7.3 Detection of Water Layer in Casted Multi-layered Specimens

Before the water layer's boundary detection, we will firstly test the capability of water layer's existence detection on casted multi-layered specimens using oblique incident ultrasonic wave. Unlike the ideal multi-layered configuration in Chapter 6, the injected water layer in the casted specimen has smaller region and thickness, and it has an artificial boundary beneath the steel plate. Two types of specimens are casted for testing: steel-mortar-concrete type and steel-epoxy-concrete type. For the 1st type, about 1mm thickness of water layer will be injected into the delamination area between steel and mortar. The using of mortar block (140mm×140mm×30mm) is for the manufacture convenience of the artificial delamination inside. Hence, the size of the water layer will be 140mm×140mm. The cross section of this type of specimen is shown in Fig. 7.4. For the 2nd type, about 5mm thickness of water layer can be injected in the gap between steel and concrete, surrounded by the 5mm thickness of epoxy

layer, as shown in Fig. 7.6. The size of the water layer beneath the steel plate will be 300mm×300mm.

In order to detect the existence of water layer inside the casted specimen, water will be firstly injected in through the holes reserved on the steel plate. Till confirming the water has penetrated into every corners of the delamination area, two transducers are then set up on the center part above the water layer. The distances adopted between the transmitter and the receiver are 8mm and 10mm in the case of the 1st type specimen. In the 2nd type specimen, the steel plate was painted with anticorrosive paint, which caused more decay on signal amplitude. Therefore, a relative small distance, 6mm between T and R is adopted.

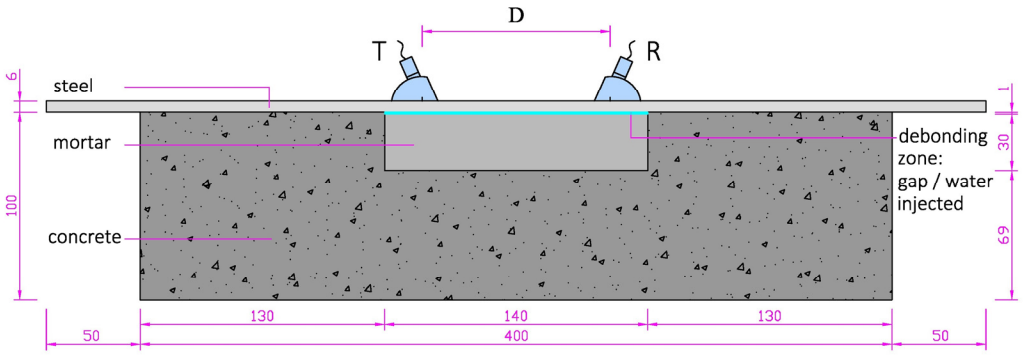

Fig. 7.4 The 1st type casted specimen: steel-mortar-concrete layered media. (Dimension: mm)

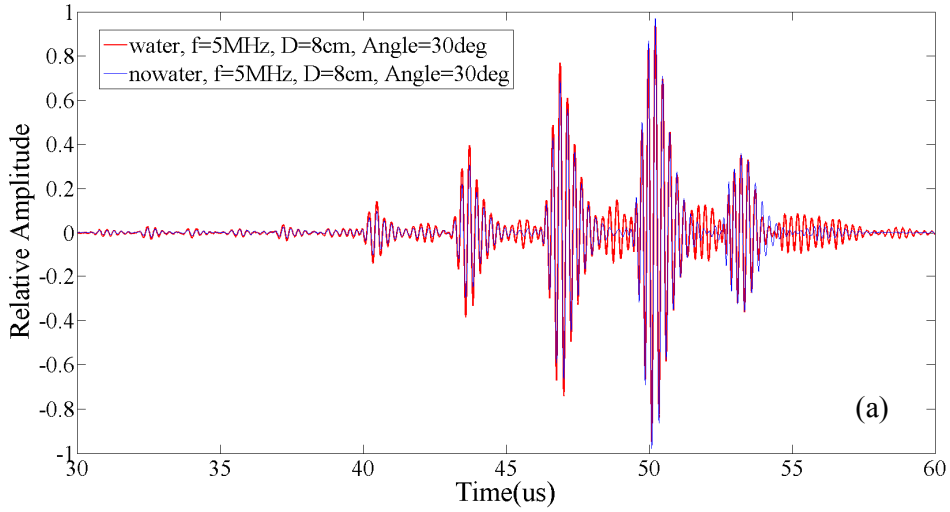

Fig. 7.5 Waveforms before water injection (blue) vs. after water injection (red) on the 1st specimen: (a), distance between T and R is 8cm;

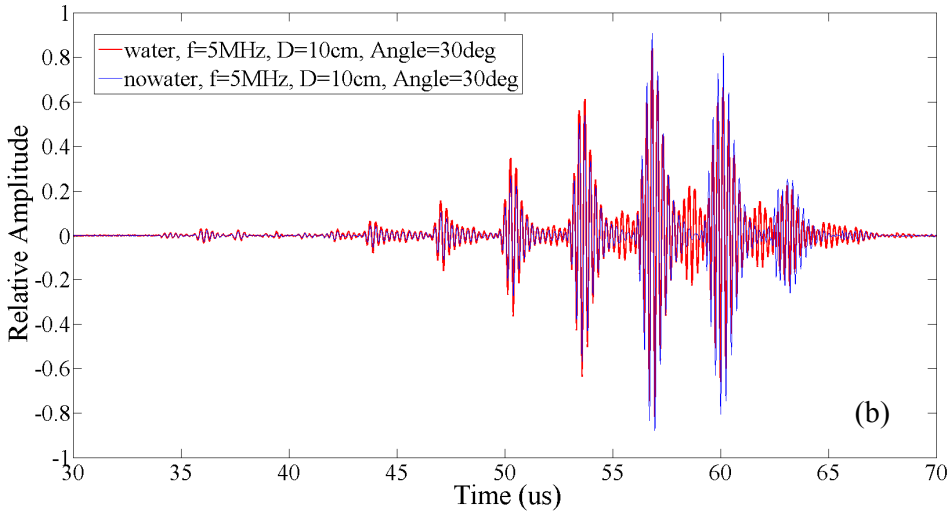

Fig. 7.5 Waveforms before water injection (blue) vs. after water injection (red) on the 1st specimen: (b), distance between T and R is 10cm.

Fig. 7.5 shows the received waveforms on the 1st specimen. The incident angle of 30 degrees is applied in this case, and the distances between transmitter and receiver are 8cm (a) and 10cm (b) respectively. From both figures we can see that the overlapped part of the signals is quite clear, which are almost identical in water case (red) and no water case (blue). However, in the waveform of water case, there is additional small amplitude wave group showing among the overlapped part, which is actually the reflected wave from the liquid layer beneath. Since in the 1st specimen, the injected water layer is very thin (about 1mm), the reflected wave is mixed with the original wave group (the overlapped part). Due to the relative low reflection ability of the bottom layer, mortar, the amplitude of the reflected wave group is not so significant. However, the difference is already distinct to detect the existence of water layer.

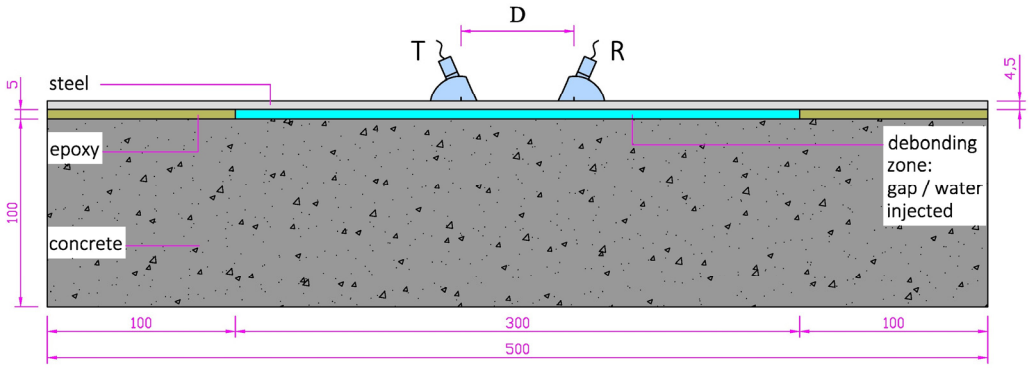

Fig. 7.6 The 2nd type casted specimen: steel-epoxy-concrete layered media. (Dimension: mm)

Fig. 7.7 shows the waveforms received on the 2nd type specimen drawn in Fig. 7.6. In this case, the receiver could be located on three different positions: on the healthily bonded area, on the debonding area without water layer, or on the debonding area with water layer beneath. Hence, both comparisons are shown in Fig. 7.7. In Fig. 7.7 (a), the blue waveform stands for the signal received on the debonding area without water layer beneath; the red waveform stands for the signal received on the same position after water been injected, as shown in Fig. 7.6. From Fig. 7.7 (a), we can easily find the reflected wave group following the original one, with clear time interval between them. From these waveforms, we can not only discover the existence of water layer, but also estimate the thickness of it. In Fig. 7.7 (b), we can still find the overlapped original wave group and the reflected wave group. In this case, the blue waveform stands for the signal received on the healthily bonded area, namely, the steel-epoxy-concrete layered media. Hence, the blue waveform has some additional components from the epoxy layer also, which is a bit complicated than the blue one in Fig. 7.7 (a). However, the difference in this comparison case is still very clear.

From those waveform comparisons, we can see that on the casted multi-layered specimens, this detection method can successfully identify the existence of the water layer inside.

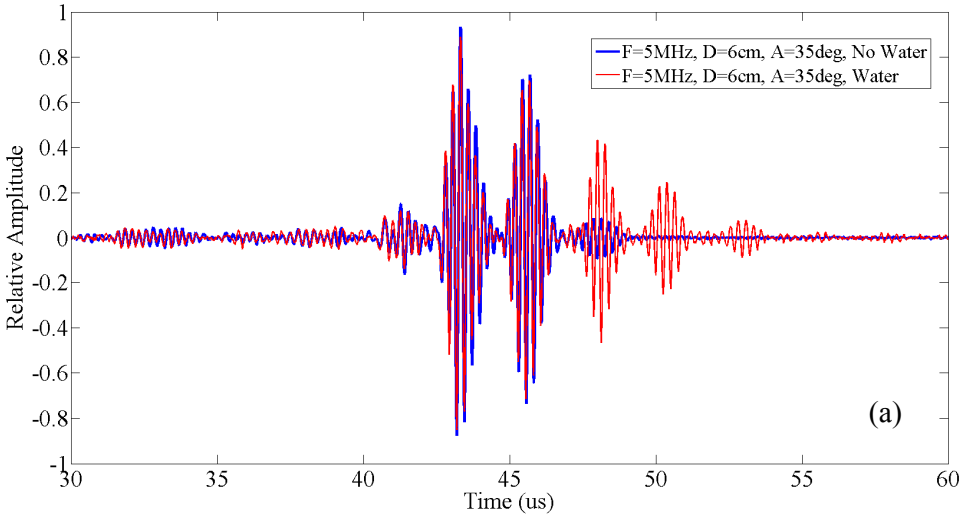

Fig. 7.7 Waveform comparison on the 2nd specimen when incident angle is 35 degrees: (a), received waveforms before water injection (blue) vs. after water injection (red);

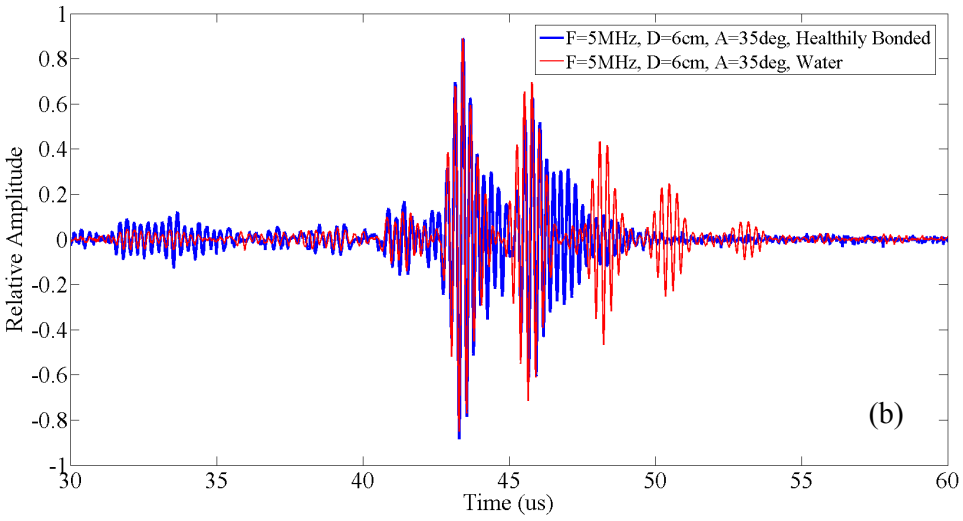

Fig. 7.7 Waveform comparison on the 2nd specimen when incident angle is 35 degrees: (b), received waveforms on healthily bonded area (blue) vs. on water injected area (red).

7.4 Boundary Identification of The Water Layer

The tests in Section 7.3 are all based on the received signal on the center of the water invaded area. The tests results can ensure that the Step 1 of the procedures of identification mentioned in Section 7.2 can be achieved. However, in Step 2, the detection will move forward to the boundary gradually, which require the detectability close to the boundary of the water layer beneath. Here, we will prove it to be practical.

Two approaching orientations will be tested: parallel approaching, in which the line of transmitter and receiver is parallel to the boundary; vertical approaching, in which the same line is vertical to the boundary.

7.4.1 Parallel Approaching

Fig. 7.8 depicts the transducers' setting for the parallel approaching. The transducers set inside the region of water layer are marked with red squares; and those set on the healthily bonded area are marked with green squares. Two distances between T and R are adopted: 4mm and 6mm. The positions of the transducers are set 2cm away from the boundary of the region

of water layer, which is quite close to the boundary. The detection move is vertical to the hidden boundary. The reason of the parallel approaching test is to check when the transducer pair's move orientation is vertical with its setting, whether or not the hidden boundary that is almost parallel to the transducer pair can be identified successfully.

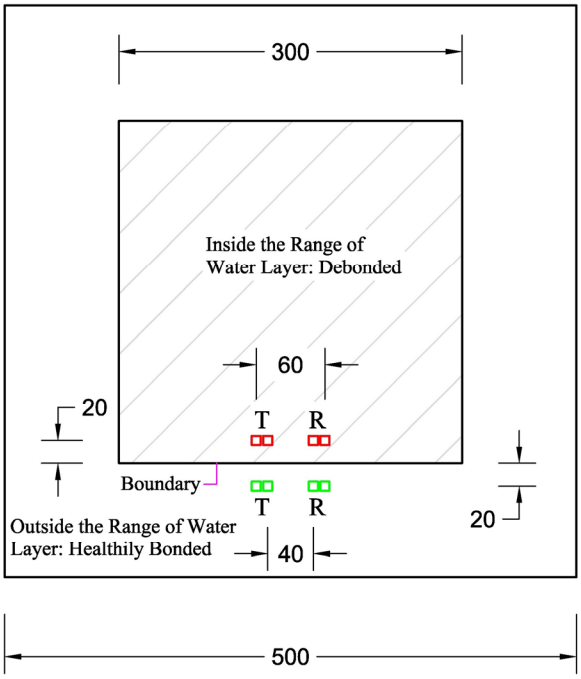

Fig. 7.8 Transducers setting for parallel approaching. (Dimension: mm.)

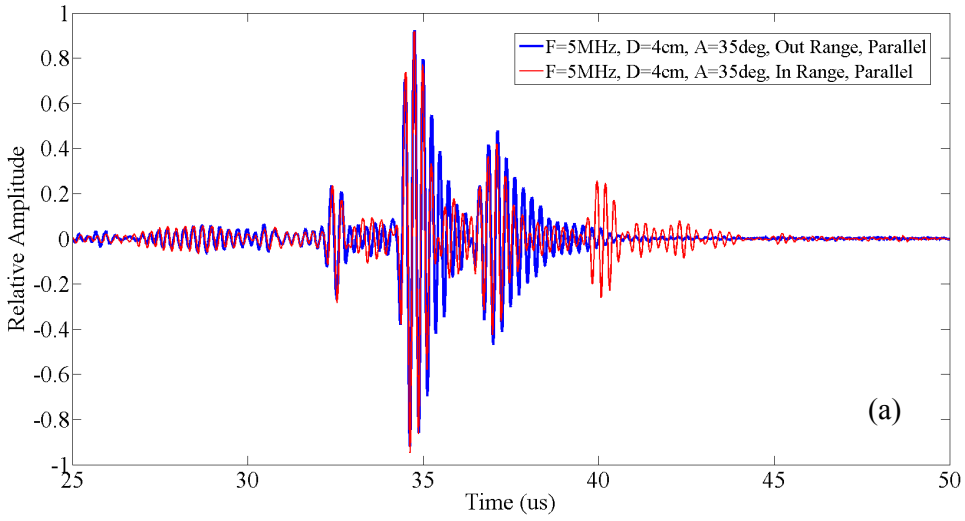

Fig. 7.9 Waveform comparison around boundary, parallel approaching: out of water range vs. in water range: (a), distance between T & R is 4cm;

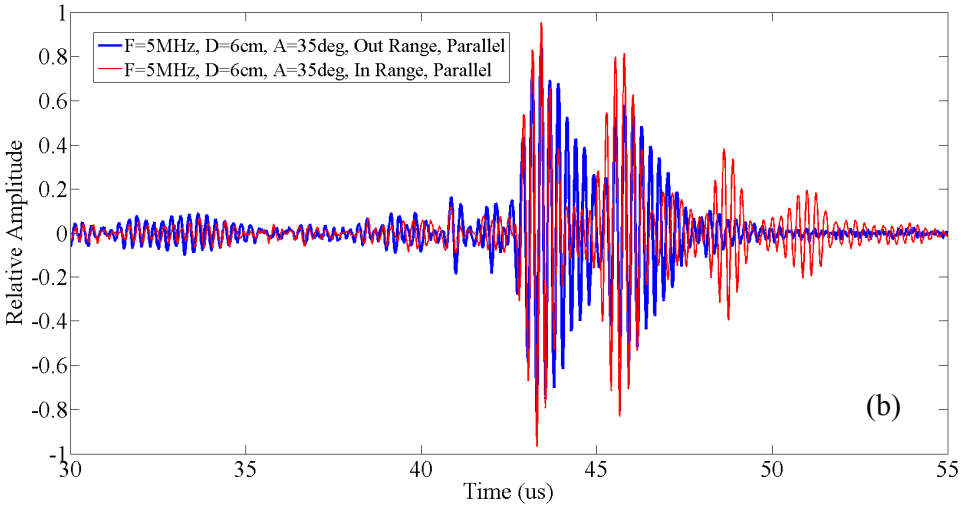

Fig. 7.9 Waveform comparison around boundary, parallel approaching: out of water range vs. in water range: (b), distance between T & R is 6cm.

Fig. 7.9 has clearly told us the feasibility of this way of approaching and transducer setting. When the transducer pair is set on the side of water range, reflected wave group can be received following the original wave group. Both the distances of 4mm and 6mm can obtain the same reflected components, which are notable enough to identify the hidden boundary. Closer the distance between T and R applies, more accurate the boundary estimation will be.

7.4.2 Vertical Approaching

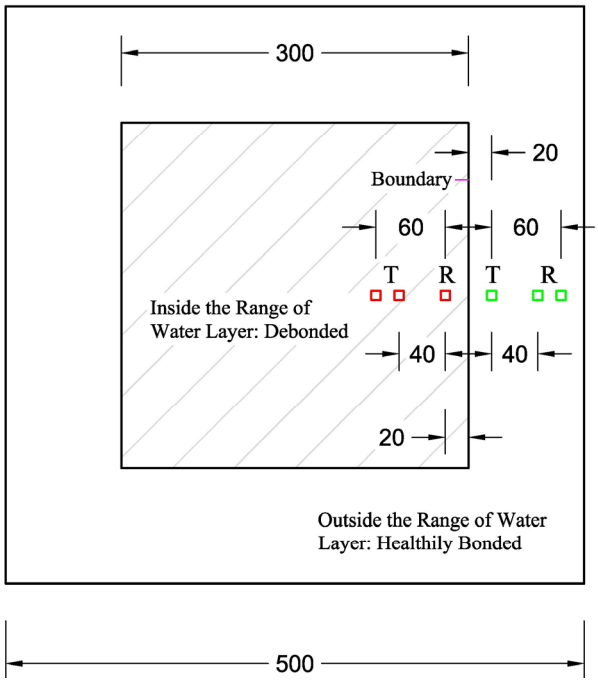

Fig. 7.10 Transducers setting for vertical approaching. (Dimension: mm.)

Similarly, in Fig. 7.10, the transducer setting of vertical approaching is depicted. In this case, the line of the transducer pair and the move orientation are both vertical to the hidden boundary. The closest transducer is 2cm away from the boundary. The test of this setting is also aimed to check the influence of transducers' position to the effect of the detection, because in the real testing, we are not able to know the relation between the hidden boundary and the transducer pair's setting orientation.

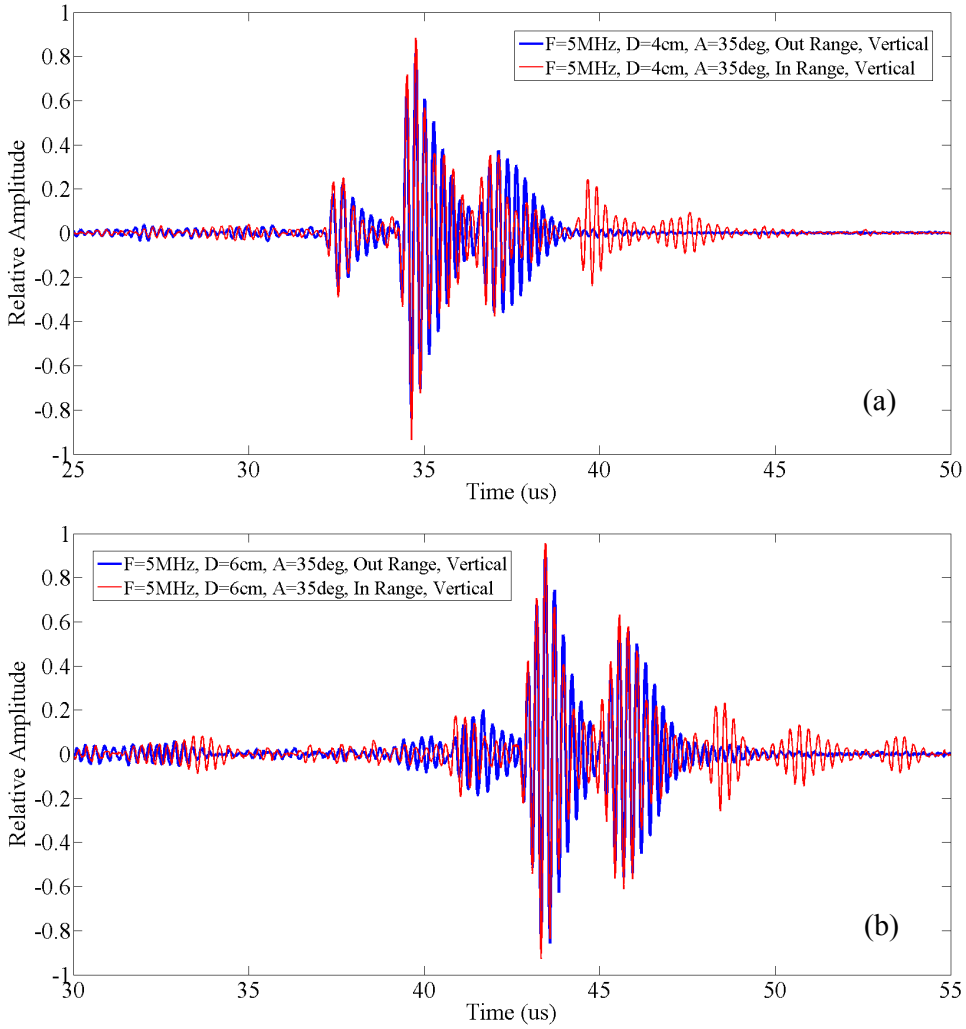

Fig. 7.11 Waveform comparison around boundary, vertical approaching: out of water range vs. in water range. (a), distance between T & R is 4cm; (b), distance between T & R is 6cm.

Again, we've got a positive answer from the waveforms we obtained in Fig. 7.11. The significant difference between in range (red line) and out range (blue line) cases are telling us

the location of the hidden boundary is just about the middle of their setting positions.

Through the tests conducted closely to the hidden boundary, we have the confidence that the procedures of the water layer's region identification is achievable. In the on-site detection of the real structure, the detection efficiency, or the detection time cost is necessary to be considered. However, the efficiency will sometimes influence the accuracy of boundary detection. How many detection points need to be set in one certain detection area, to keep a good balance between the detection accuracy and efficiency, require a mature optimization. One plan is to develop two parallel observe windows in the oscilloscope which can show the present waveform and the previous waveform at the same time, so that a quick comparison of received waveform change can be achieved. In this way, the detection move will be fast and also the accuracy can be assured.

7.5 Summary

In this chapter, an identification approach for the region of water layer beneath the steel plate has been proposed, and its procedures has also been presented. The feasibility of the 3 steps of detection has been proven through the tests on the casted multi-layered specimen with reserved delamination or gap area between layers. In the tests, two ways of detection moving, the parallel and the vertical, have been employed with good detectability. Hence, the multi-reflection method proposed in Chapter 6 has been extended here. However, the tests in this chapter are only based on the casted specimen, the detection on the real damaged structures is not yet to be done, which would become the future work to be conducted.

CHAPTER 8

CONCLUSIONS AND RECOMMENDATIONS

8.1 Conclusions

This research investigates the nondestructive evaluation of multi-layered media, and two main objectives are included: to estimate the material property of epoxy layer in steel-epoxy-concrete layered media, and to detect water layer beneath the solid plate. Both the objectives have been achieved successfully through the theoretical research and the experimental work that have been done. The contributions of this research can be briefly summarized as follows:

(1) Dispersion equation solving and analytical dispersion curves obtaining.

Different types of multi-layered media have been considered according to the real configurations of different statuses of epoxy bonded steel plate strengthened RC slabs, especially the water layer contained multi-layered media. The dispersion equations of each type have been deduced and solved employing the upgraded bisection method. The analytical dispersion curves have been plotted, and the cases of with water layer and without water layer have been compared through the dispersion curves. Wave structures of different modes have

been analyzed and can be used to distinguish modes development when they are very close to each other or have crossing point at certain frequencies.

(2) Experimental dispersion curves obtaining through spectral analysis of surface waves.

A nondestructive testing of surface wave generation and receiving on a steel-epoxy-concrete layered specimen has been conducted. The received waveforms with certain distance were processed using spectral analysis, and their phase difference was calculated on certain frequency range, based on which the experimental dispersion curves were able to be plotted. The position settings of transmitter and receiver were finely controlled to receive stable signals with high coherence values and good spectral properties. The experimental dispersion curves of multi-layered media with inhomogeneous material, concrete, were rarely obtained in former researches.

(3) Material property estimation through inversion process of analytical and experimental dispersion curves.

An inversion process based on variation function and simplex method has been developed for the optimization of analytical dispersion curves and experimental one. Material propertie of the epoxy layer was then estimated with a good accuracy. However, the inversion process is highly related with the quality of experimental dispersion curves we obtained. Especially, due to the inhomogeneity of the concrete material and the functional restrict of the transducers, there are deviated phase velocity points with low coherence values that need to be excluded manually before the inversion process.

(4) Water layer detection and thickness estimation based on multi-reflection of oblique incident waves.

A novel detection method of water layer in multi-layered media based on multi-reflection

of oblique incident waves have been developed. The effects of incident angles, water layer thicknesses, and the material properties of bottom layer have been tested and presented with numbers of waveforms from the experiments on different multi-layered configurations. The explanation of those experimental phenomenon is given according to the reflection and transmission coefficients. A method of water layer thickness estimation is proposed and tested with acceptable errors, whose possible causes are given, according to which the estimation could be improved.

(5) Identification of the region of water layer.

An identification approach of region of water layer beneath the steel plate based on the multi-reflection effect is developed with three steps of procedure. The feasibility of this region identification has also been proven through the tests on casted multi-layered specimens. Two possible approaches of the detection move, the parallel and the vertical ways, have been tested also. This identification approach of the region of water layer can be effectively applied in the practical detection as well.

8.2 Recommendations

This research shall be continued in the following aspects:

a. The roots searching algorithm can be improved by adding automatically modes distinguishing module based on wave structures, so that the dispersion curve plotting program can automatically select the roots in the same wave mode. It could strongly increase the efficiency of the plotting.

b. The liquid detection can also be tried from the difference of the mode shape of the 1st mode and 2nd mode, especially from the difference of group velocities. Then a direct but precise group velocity measurement can tell whether or not there is water layer beneath. However, that group velocity measurement on multi-layered media may meet certain challenges.

c. The amplitudes of the reflected wave groups shall be estimated and related with the calculated reflection coefficients, e.g. the multiplication of the reflection and refraction coefficients along wave's propagating path.

d. The complicated multiple reflections and transmissions in the wedge-plate contact area which generate the wavelets in a wave group shall be analyzed and simulated, to control the error level in the water layer thickness estimation.

e. The liquid detection method and the liquid layer region identification shall be tested and applied in the practical NDE work in the detection of real structures.

REFERENCES

Achenbach, J. D. (1980), Wave Propagation in Elastic Solids. *Amsterdam: North-Holland*, pp. 66 & pp. 221.

Adhikary, B. B. and Mutsuyoshi, H. (2002), Numerical simulation of steel-plate strengthened concrete beam by a nonlinear finite element method model. *Construction and Building Materials*, Vol. 16, pp. 291-301.

Ahyi, A. C., Pernod, P., Gatti, O., Latard, V., Merlen, A. and Überall, H. (1998), Experimental demonstration of the pseudo-Rayleigh (A0) wave. *J. Acoust. Soc. Am.*, Vol. 104, pp. 2727-2732.

Antonio, O. V. M. and Hirose, S. (2012), Ultrasonic imaging of concrete by synthetic aperture focusing technique based on Hilbert-Huang transform of time domain data. *Materials Transactions*, Vol. 53(4), pp. 621-626.

Auld, B. A. (1973), Acoustic fields and waves in solids, Vols. 1 and 2. *New York, Wiley*.

Bao, X. L., Franklin, H., Raju, P. K. and Überall, H. (1997), The splitting of dispersion curves for plates fluid-loaded on both sides. *J. Acoust. Soc. Am.*, Vol. 102, pp. 1246-1248.

Barnes, R. A., Baglin, P. S., Mays, G. C. and Subedi, N. K. (2001), External steel plate systems for the shear strengthening of reinforced concrete beams. *Engineering Structures*, Vol. 23, pp. 1162-1176.

Billy, M. and Quentin, G. (1983), Experimental study of the Scholte wave propagation on a plane surface partially immersed in a liquid. *Journal of Applied Physics*, Vol. 54, pp. 4314-4322.

Burch, S. F., Collett, N. J., Terpstra, S. and Hoekstra, M. V. (2007), M-skip: A quantitative technique for the measurement of wall loss in inaccessible components. *Insight- Non-Destructive Testing and Condition Monitoring*, Vol. 49(4), pp. 190-194.

Buyukozturk, O., Gunes, O. and Karaca, E. (2004), Progress on understanding debonding problems in reinforced concrete and steel members strengthened using FRP composites. *Construction and Building Materials*, Vol. 18(1), pp. 9-19.

Cegla, F. B., Cawley, P. and Lowe, M. J. S. (2005), Material property measurement using the quasi-Scholte mode-A waveguide sensor. *J. Acoust. Soc. Am.*, Vol. 117(3), pp. 1098-1107.

Chimenti, D. E. and Nayfeh, A. H. (1985), Leaky Lamb waves in fibrous composite laminates. *Journal of Applied Physics*, Vol. 58, pp. 4531-4538.

Chimenti, D. E. and Martin, R. W. (1991), Nondestructive evaluation of composite laminates

by leaky Lamb waves. *Ultrasonics*, Vol. 29(1), pp. 13-21.

Dayal, V. and Kinra, V. K. (1989), Leaky Lamb waves in an anisotropic plate. I: An exact solution and experiments. *J. Acoust. Soc. Am.*, Vol. 85(6), pp. 2268-2276.

Dayal, V. and Kinra, V. K. (1991), Leaky Lamb waves in an anisotropic plate. II: Nondestructive evaluation of matrix cracks in fiber-reinforced composites. *J. Acoust. Soc. Am.*, Vol. 89, pp. 1590-1598.

Dorman, J. (1962), Period equation for waves of Rayleigh type on a layered, liquid-solid half space. *Bulletin of the Seismological Society of America*, Vol. 52(2) pp. 389-397.

Ewing, W. M., Jardetzky, W. S. and Press, F. (1957), Elastic Waves in Layered Media. *New York: McGraw-Hill*.

Favretto, A. N. and Rabau, G. (1997), Excitation of the stoneley-scholte wave at the boundary between an ideal fluid and a viscoelastic solid. *Journal of Sound and Vibration*, Vol. 203(2), pp. 193-208.

Ferguson T. P. and Qu, J. M. (2006), Elastic modulus variation due to moisture absorption and permanent changes upon redrying in an epoxy based underfill. *IEEE transactions on components and packaging technologies*, Vol. 29(1), pp. 105-111.

Folds, D. L. and Loggins, C. D. (1977), Transmission and reflection of ultrasonic waves in layered media. *J. Acoust. Soc. Am.*, Vol. 62, pp. 1102-1109.

Ganji, V., Gucunski, N. and Nazarian, S. (1998), Automated inversion procedure for spectral analysis of surface waves. *J. Geotech. Geoenviron. Eng.*, Vol. 124(8), pp. 757-770.

Gélébart, Y., Duflo, H. and Duclos, J. (2007), Air coupled Lamb waves evaluation of the long-term thermo-oxidative ageing of carbon-epoxy plates. *NDT&E International*, Vol. 40, pp. 29-34.

Goueygou, M., Piwakowski, B., Fnine, A., Kaczmarek, M. and Buyle-Bodin, F. (2004), NDE of two-layered mortar samples using high-frequency Rayleigh waves. *Ultrasonics*, Vol. 42(1-9), pp. 889-895.

Hayashi, T., Tamayama, C. and Murase, M. (2006), Wave structure analysis of guided waves in a bar with an arbitrary cross-section. *Ultrasonics*, Vol. 44(1), pp. 17-24.

Henneke, E. G. (1972), Reflection-refraction of a stress wave at a plane boundary between anisotropic media. *J. Acoust. Soc. Am.*, Vol. 51, pp. 210-217.

Hosten, B., Castaings, M., Tretout, H. and Voillaume, H. (2001), Identification of composite

materials elastic moduli from Lamb wave velocities measured with single sided, contactless ultrasonic method. *Review of Progress in Quantitative Nondestructive Evaluation*, Vol. 20, pp. 1023-1030.

Hu, H. W. and Sun C. T. (2000), The characterization of physical aging in polymeric composites. *Composites Science and Technology*, Vol. 60(14), pp. 2693-2698.

Jardetzky, W. S. and Press, F. (1953), Crustal structure and surface-wave dispersion: Part III, Theoretical dispersion curves for suboceanic Rayleigh waves. *Bulletin of the Seismological Society of America*, Vol. 43(2), pp. 137-144.

Jones, R., Swamy, R. N. and Ang, T. H. (1982), Under- and over-reinforced concrete beams with glued steel plates. *The International Journal of Cement Composites and Lightweight Concrete*, Vol. 4, pp. 19-32.

Joseph, L. R. (1999), Ultrasonic waves in solid media. *Cambridge University Press*, pp. 416-417.

Kajorncheappunngam, S., Gupta, R., and GangaRao, H. (2002), Effect of Aging Environment on Degradation of Glass-Reinforced Epoxy. *J. Compos. Constr.*, Vol. 6(1), pp. 61-69.

Karim, M. R., Mal, A. K. and Bar-Cohen, Y. (1990), Inversion of leaky Lamb wave data by simplex algorithm. *J. Acoust. Soc. Am.*, Vol. 88(1), pp. 482-491.

Kim, Y. H., Kim, D. H., Han, J. H. and Kim, C. G. (2007), Damage assessment in layered composites using spectral analysis and Lamb wave. *Composites: Part B*, Vol. 38, pp. 800-809.

Kotyaev, O., Shimada, Y., Hirose, S., Tachibana, H., Nakamoto, K., Misaki, N. and Takinami, H. (2014), Actual laser-based methods for remote inspection of shinkansen tunnels and highway bridges. *Proc. The 5th US-Japan NDT Symposium, The American Society for Nondestructive Testing*, pp. 212-218.

Kundu, T., Bereiter-Hahn, J. and Hillmann, K. (1991), Measuring elastic properties of cells by evaluation of scanning acoustic microscopy V(Z) values using simplex algorithm. *Biophysical Journal*, Vol. 59(6), pp. 1194-1207.

Lafarie-Frenot, M. C., Rouquié, S., Ho, N. Q. and Bellenger, V. (2006), Comparison of damage development in C/epoxy laminates during isothermal ageing or thermal cycling. *Composites Part A: Applied Science and Manufacturing*, Vol. 37(4), pp. 662-671.

Lee, Y. C. and Cheng, S. W. (2001), Measuring Lamb wave dispersion curves of a bi-layered plate and its application on material characterization of coating. *Ultrasonics, Ferroelectrics, and Frequency Control, IEEE Transactions*, Vol. 48(3), pp. 830-837.

Lobkis, O. I., Chimenti, D. E. and Zhang, H. (2000), In-plane elastic property characterization in composite plates. *J. Acoust. Soc. Am.*, Vol. 107(4), pp. 1852-1858.

Lorenz, M. and Lewandowski, S. (2012), Ultrasonic Multi-Skip inspection at clamped saddle supports. *18th World Conference on Nondestructive Testing*.

Luppe, F. and Doucet, J. (1988), Experimental study of the Stoneley wave at a plane liquid-solid interface. *J. Acoust. Soc. Am.*, Vol. 83(4), pp. 1276-1279.

Lydon, F. D. and Iacovou, M. (1995), Some factors affecting the dynamic modulus of elasticity of high strength concrete. *Cement and Concrete Research*, Vol. 25(6), pp. 1246-1256.

Lydon, F. D. and Balendran, R. V. (1986), Some observations on elastic properties of plain concrete. *Cement and Concrete Research*, Vol. 16(3), pp. 314-324.

Mailhot, B., Morlat-Thérias, S., Bussière, P. -O. and Gardette, J. -L. (2005), Study of the degradation of an epoxy/amine resin, 2. *Macromol. Chem. Phys.*, Vol. 206, pp. 585–591.

Monney, L., Belali, R., Vebrel, J., Dubois, C. and Chambaudet, A. (1998), Photochemical degradation study of an epoxy material by IR-ATR spectroscopy. *Polymer Degradation and Stability*, Vol. 62(2), pp. 353-359.

Murray, S., Hillman, C. and Pecht, M. (2003), Environmental aging and deadhesion of siloxane-polyimide-epoxy adhesive. *IEEE Transactions on Components and Packaging Technologies*, Vol. 26(3), pp. 524-531.

Naffa, S. O., Goueygou, M., Piwakowski, B. and Buyle-Bodin, F. (2002), Detection of chemical damage in concrete using ultrasound. *Ultrasonics*, Vol. 40(1-8), pp. 247-251.

Nayfeh, A. H. (1995), Wave Propagation in Layered Anisotropic Media: with Applications to Composites. *North-Holland*, pp. 99.

Nayfeh, A. H. and Chimenti, D. E. (1984), Reflection of finite acoustic beams from loaded and stiffened half-spaces. *J. Acoust. Soc. Am.*, Vol. 75(5), pp. 1360-1368.

Nazarian, S. and Desai, M. R. (1993), Automated surface wave method: field testing. *Journal of Geotechnical Engineering*, Vol. 119(7), pp. 1094-1111.

Nelder, J. A. and Mead, R. (1965), A simplex method for function minimization. *Comput J*, Vol. 7, pp. 308.

Neville, A. M. (1997), Properties of concrete, 4th edition. *New York: John Wiley & Sons Inc*.

Ngoc, T. D. K. and Mayer, W. G. (1979), Ultrasonic nonspecular reflectivity near longitudinal critical angle. *Journal of Applied Physics*, Vol. 50, pp. 7948-7951.

Park, J. (1996), Surface waves in layered anisotropic structures. *Geophys. J. Int.*, Vol. 126 (1), pp. 173-183.

Parra, J. O. and Xu, P. C. (1994), Dispersion and attenuation of acoustic guided waves in layered fluid-filled porous media. *The Journal of the Acoustical Society of America*, Vol. 95, pp. 91-98.

Puthillath, P. and Rose, J. L. (2010), Ultrasonic guided wave inspection of a titanium repair patch bonded to an aluminum aircraft skin. *International Journal of Adhesion and Adhesives,* Vol. 30(7), pp. 566-573.

Pilarski, A. and Rose, J. L. (1988), A transverse-wave ultrasonic oblique-incidence technique for interfacial weakness detection in adhesive bonds. *J. Appl. Phys*. Vol. 63(2), pp. 300-307.

Pilarski, A. and Rose, J. L. (1988), Ultrasonic oblique incidence for improved sensitivity in interface weakness determination. *NDT International*, Vol. 21(4), August, pp. 241-246.

Pilarski, A., Rose, J. L. and Balasubramaniam, K. (1990), The angular and frequency characteristics of reflectivity from a solid layer embedded between two solids with imperfect boundary conditions. *J. Acoust. Soc. Am.*, Vol. 87(2), pp. 532-542.

Plonka, R., Mäder, E., Gao, S. L., Bellmann, C., Dutschk, V. and Zhandarov, S. (2004), Adhesion of epoxy/glass fibre composites influenced by aging effects on sizings. *Composites Part A: Applied Science and Manufacturing*, Vol. 35(10), pp. 1207-1216.

Piwakowski, B., Fnine, A., Goueygou, M. and Buyle-Bodin, F. (2004), Generation of Rayleigh waves into mortar and concrete samples. *Ultrasonics*, Vol. 42(1-9), pp. 395-402.

Rogers, W. P. (1995), Elastic property measurement using Rayleigh-Lamb waves. *Research in Nondestructive Evaluation*, Vol. 6(4), pp. 185-208.

Rose, J. L. (1999), Ultrasonic waves in solid media. *Cambridge, UK : Cambridge University Press*.

Ryden, N. and Lowe, M. J. S. (2004), Guided wave propagation in three-layer pavement structures. *J. Acoust. Soc. Am.*, Vol. 116(5), pp. 2902-2913.

Schmitt, M., Olfert, S., Rautenberg, J., Lindner, G., Henning, B. and Reindl, L. M. (2013), Multi reflection of Lamb wave emission in an acoustic waveguide sensor. *Sensors*, Vol. 13(3), pp. 2777-2785.

Schoenberg, M. (1980), Elastic wave behavior across linear slip interfaces. *J. Acoust. Soc. Am.*, Vol. 68, pp. 1516-1521.

Sessarego, J. P., Sagéloli, J., Gazanhes, C. and Überall, H. (1997), Two Scholte–Stoneley waves on doubly fluid-loaded plates and shells. *J. Acoust. Soc. Am.*, Vol. 101, pp. 135-142.

Shao, G. Z., Li, Q. C. and Liang, Z. Q. (2007), A study on dispersion curves of guided wave in layered media with overlying liquid surface. *Chinese J. Geophys.*, Vol. 50, pp. 783-789.

Shen, Y., Hirose, S. and Yamaguchi, Y. (2014), Dispersion of ultrasonic surface waves in a steel-epoxy-concrete bonding layered media based on analytical, experimental, and numerical study. *Case Studies in Nondestructive Testing and Evaluation*, Vol. 2, pp. 49-63.

Shen, Y. and Hirose, S. (2016), Detection and thickness estimation of water layer in layered media based on multi-reflection of oblique incident ultrasonic wave. *Materials Transactions*, (Accepted).

Su, Z. Q., Ye, L. and Lu, Y. (2006), Guided Lamb waves for identification of damage in composite structures: a review. *Journal of Sound and Vibration*, Vol. 295, pp.753-780.

Tachibana, H., Nakamoto, K., Yamaguchi, Y. and Hirose, S. (2014), Quantitative non-destructive evaluation of damages in a steel plate bonding method. *The 7th International Conference on Bridge Maintence, Safety and Management*, pp. 622-627.

Taeljsten, B. (1997), Defining anchor lengths of steel and CFRP plates bonded to concrete. *Int. J. Adhesion and Adhesives*, Vol. 17, pp. 319-327.

Talmant, M., Uberall, H., Miller, R. D., Werby, M. F. and Dickey, J. W. (1989), Lamb waves and fluid-borne waves on water-loaded, air-filled thin spherical shells. *J. Acoust. Soc. Am.*, Vol. 86(1), pp. 278-297.

Tolstoy, I. (1954), Dispersive properties of a fluid layer overlying a semi-infinite elastic solid. *Bulletin of the Seismological Society of America*, Vol. 44(3), pp. 493-512.

Tsai, C. D., Wu, T. T. and Liu, Y. H. (2001), Application of neural networks to laser ultrasonic NDE of bonded structures. *NDT&E International*, Vol. 34, pp. 537-546.

Uberall, H., Hosten, B., Deschamps, M. and Gerard, A. (1994), Repulsion of phase-velocity dispersion curves and the nature of plate vibrations. *J. Acoust. Soc. Am.*, Vol. 96(2), pp. 908-917.

Vallo, C. I., Frontini, P. M. and Williams, R. J. J. (1993), Elastic modulus and yield stress of epoxy networks in the glassy state. *Polymer Gels and Networks*, Vol. 1(4), pp. 257-266.

Vilnay, O. (1988), The analysis of reinforced concrete beams strengthened by epoxy bonded steel plates. *International Journal of Cement Composites and Lightweight Concrete*, Vol. 10(2), pp. 73-78.

Volker, A. and Zon, T. V. (2013), Ultrasonic multi-skip tomography for pipe inspection. *AIP Conf. Proc*, Vol. 1511, pp. 722-728.

Wu, T. T. and Chen, Y. C. (1996), Dispersion of laser generated surface waves in an epoxy-bonded layered media. *Ultrasonics*, Vol. 34, pp. 793-799.

Wu, T. T. and Liu, Y. H. (1999), Inverse determinations of thickness and elastic properties of a bonding layer using laser-generated surface waves. *Ultrasonics*, Vol. 37, pp. 23-30.

Xiao, G. Z. and Shanahan, M. E. R. (1997), Water absorption and desorption in an epoxy resin with degradation. *J. Polym. Sci. B Polym. Phys.*, Vol. 35, pp. 2659-2670.

Xu, P. C., Mal, A. K. and Bar-Cohen, Y. (1990), Inversion of leaky Lamb wave data to determine cohesive properties of bonds. *International Journal of Engineering Science*, Vol. 28(4), pp. 331-346.

Yanagihara, A., Hatanaka, H., Toda, K. and Nakamura, Y. (2015), Development of ultrasonic testing for steel-concrete composite structures. *Proceedings of the 22th Symposium on Ultrasonic Testing*, pp. 139-142.

Yuan, D. and Nazarian, S. (1993), Automated surface wave method: inversion technique. *Journal of Geotechnical Engineering*, Vol. 119(7), pp. 1112-1126.

Yuan, L., Shi, Y. F., Shen, Z. H. and Ni, X. W. (2008), Laser-induced ultrasonic waves in steels with gradient changes of elastic property. *Optics & Laser Technology*; Vol. 40, pp. 325-329.

Zhang, B. and Lu, L. (2003), Rayleigh wave and detection of low-velocity layers in a stratified half-space. *Acoustical Physics*, Vol. 49(5), pp. 516-528.

Zhang, B., Xiong, W., Yu, M., Lan, C. Q. and Li, L. (1998), Study of energy distribution of guided waves in multilayered media. *J. Acoust. Soc. Am.*, Vol. 103, pp. 125-135.

Ziraba, Y. N. and Baluch, M. H. (1995), Computational model for reinforced concrete beams strengthened by epoxy bonded steel plates. *Finite Elements in Analysis and Design*, Vol. 20(4), pp. 253-271.